Theses and Dissertations | 1. Thesis and Dissertation Collection, all items

2008-03

Statistics of acoustic pulse signals through nonlinear internal waves on the continental shelf of the northeastern South China Sea

Reeves, Justin M.

Monterey, California. Naval Postgraduate School

http://hdl.handle.net/10945/4185

NAVAL POSTGRADUATE SCHOOL

MONTEREY, CALIFORNIA

DISSERTATION

STATISTICS OF ACOUSTIC PULSE SIGNALS THROUGH NONLINEAR INTERNAL WAVES ON THE CONTINENTAL SHELF OF THE NORTHEASTERN SOUTH CHINA SEA

by

Justin M. Reeves

March 2008

Dissertation Supervisor: C. – S. Chiu

Approved for public release; distribution is unlimited.

THIS PAGE INTENTIONALLY LEFT BLANK

REPORT DOCUMENTATION PAGE		*Form Approved OMB No. 0704-0188*

Public reporting burden for this collection of information is estimated to average 1 hour per response, including the time for reviewing instruction, searching existing data sources, gathering and maintaining the data needed, and completing and reviewing the collection of information. Send comments regarding this burden estimate or any other aspect of this collection of information, including suggestions for reducing this burden, to Washington headquarters Services, Directorate for Information Operations and Reports, 1215 Jefferson Davis Highway, Suite 1204, Arlington, VA 22202-4302, and to the Office of Management and Budget, Paperwork Reduction Project (0704-0188) Washington DC 20503.

1. AGENCY USE ONLY *(Leave blank)*	2. REPORT DATE March 2008	3. REPORT TYPE AND DATES COVERED Dissertation	
4. TITLE AND SUBTITLE: Statistics of Acoustic Pulse Signals Through Nonlinear Internal Waves on the Continental Shelf of the Northeastern South China Sea		**5. FUNDING NUMBERS**	
6. AUTHOR(S) Justin Martin Reeves			
7. PERFORMING ORGANIZATION NAME(S) AND ADDRESS(ES) Naval Postgraduate School Monterey, CA 93943-5000		**8. PERFORMING ORGANIZATION REPORT NUMBER**	
9. SPONSORING / MONITORING AGENCY NAME(S) AND ADDRESS(ES) N/A		**10. SPONSORING / MONITORING AGENCY REPORT NUMBER**	

11. SUPPLEMENTARY NOTES The views expressed in this thesis are those of the author and do not reflect the official policy or position of the Department of Defense or the U.S. Government.

12a. DISTRIBUTION / AVAILABILITY STATEMENT Approved for public release; distribution is unlimited.	12b. DISTRIBUTION CODE

13. ABSTRACT (maximum 200 words)
A component of the Office of Naval Research (ONR) funded Windy Islands Soliton Experiment (WISE) was conducted from 13 – 15 April 2005 on the continental shelf in the northeast portion of the South China Sea to study the effects of nonlinear internal waves on the transmission of a 400-Hz signal. To capture the ocean variability along the acoustic path, a series of environmental moorings were deployed that sampled the water column. Significant variability in the sound-speed field was observed to be induced by nonlinear internal tides with a broad (~ 10 km) horizontal scale (referred to as the "long-wave pattern") and narrow (< 1 km), high-frequency, nonlinear internal depression and elevation waves superimposed on the internal tides. Through the use of an empirical sound-speed field and a coupled, normal-mode acoustic propagation model, the phenomenology of the nonlinear internal wave field upon the observed intensity pattern was examined. Analysis of the observed and modeled acoustic intensity time-series indicates that the long-wave pattern dictates, to a large degree, the temporal changes in the vertical structure of the sound intensity level. Furthermore, both measurement and model results show that when the thermocline was rapidly displaced by the nonlinear internal waves, sound intensity fluctuations reached their maximum. Modeling results suggest that these maximums are due to the scattering of acoustic energy into both higher and lower acoustic modes along the edges of the elevation/depression waves where strong horizontal sound-speed gradients were present. An additional goal of this paper is to propose and validate an extended statistical theory that relates the observed statistics of the acoustic intensity to the number of resolvable arrivals. The number of resolvable arrivals depends on signal bandwidth and the criteria of "well separateness" and was found to vary significantly as the nonlinear internal waves evolve along the transmission path. The theory is found to be pertinent when the temporal length of the window for calculating statistics was expanded sufficiently in order to collect a sample population with the following characteristics: 1) the standard deviation of the estimated number of arrivals is small, and 2) sufficient internal wave events are captured to ensure the phase distribution of the arrivals in the sample population is uniform.

14. SUBJECT TERMS Acoustic Intensity fluctuations, nonlinear internal waves, shallow-water acoustics, South China Sea, phase random distributions.			15. NUMBER OF PAGES 124
			16. PRICE CODE
17. SECURITY CLASSIFICATION OF REPORT Unclassified	18. SECURITY CLASSIFICATION OF THIS PAGE Unclassified	19. SECURITY CLASSIFICATION OF ABSTRACT Unclassified	20. LIMITATION OF ABSTRACT UU

NSN 7540-01-280-5500

THIS PAGE INTENTIONALLY LEFT BLANK

STATISTICS OF ACOUSTIC PULSE SIGNALS THROUGH NONLINEAR INTERNAL WAVES ON THE CONTINENTAL SHELF OF THE NORTHEASTERN SOUTH CHINA SEA

Justin M. Reeves
Lieutenant Commander, United States Navy
B.S., United States Naval Academy, 1994
M.S., Naval Postgraduate School, 2005

Submitted in partial fulfillment of the
requirements for the degree of

DOCTOR OF PHILOSOPHY IN PHYSICAL OCEANOGRAPHY

from the

**NAVAL POSTGRADUATE SCHOOL
March 2008**

Author: _____

Justin M. Reeves

Approved by:

_____   _____
Ching-Sang Chiu   John A. Colosi
Professor of Oceanography   Associate Professor of
Dissertation Supervisor /   Oceanography
Committee Chair

_____   _____
Steven R. Ramp   Patrick A. Harr
Visiting Professor of Oceanography   Professor of Meteorology

_____
D. Benjamin Reeder
Visiting Assistant Professor of Oceanography

Approved by: _____

Mary L. Batteen, Chair, Department of Oceanography

Approved by: _____

Douglas Moses, Associate Provost for Academic Affairs

iii

THIS PAGE INTENTIONALLY LEFT BLANK

ABSTRACT

A component of the Office of Naval Research (ONR) funded Windy Islands Soliton Experiment (WISE) was conducted from 13 – 15 April 2005 on the continental shelf in the northeast portion of the South China Sea to study the effects of nonlinear internal waves on the transmission of a 400-Hz signal. To capture the ocean variability along the acoustic path, a series of environmental moorings were deployed that sampled the water column. Significant variability in the sound-speed field was observed to be induced by nonlinear internal tides with a broad (~ 10 km) horizontal scale (referred to as the "long-wave pattern") and narrow (< 1 km), high-frequency, nonlinear internal depression and elevation waves superimposed on the internal tides. Through the use of an empirical sound-speed field and a coupled, normal-mode acoustic propagation model, the phenomenology of the nonlinear internal wave field upon the observed intensity pattern was examined. Analysis of the observed and modeled acoustic intensity time-series indicates that the long-wave pattern dictates, to a large degree, the temporal changes in the vertical structure of the sound intensity level. Furthermore, both measurement and model results show that when the thermocline was rapidly displaced by the nonlinear internal waves, sound intensity fluctuations reached their maximum. Modeling results suggest that these maximums are due to the scattering of acoustic energy into both higher and lower acoustic modes along the edges of the elevation/depression waves where strong horizontal sound-speed gradients were present. An additional goal of this paper is to propose and validate an extended statistical theory that relates the observed statistics of the acoustic intensity to the number of resolvable arrivals. The number of resolvable arrivals depends on signal bandwidth and the criteria of "well separateness" and was found to vary significantly as the nonlinear internal waves evolve along the transmission path. The theory is found to be pertinent when the temporal length of the window for calculating statistics was expanded sufficiently in order to collect a sample population with the following characteristics: 1) the standard deviation of the estimated number of arrivals is small, and 2) sufficient internal wave events are captured to ensure the phase distribution of the arrivals in the sample population is uniform.

THIS PAGE INTENTIONALLY LEFT BLANK

TABLE OF CONTENTS

viii

LIST OF FIGURES

LIST OF TABLES

THIS PAGE INTENTIONALLY LEFT BLANK

ACKNOWLEDGMENTS

First and foremost, I would like to thank Chris Miller for his unending personal and technical support throughout the length of my research. I would also like to thank Dr. Jeff Haferman and Mr. Bob Creasey for their support. Both gentlemen provided the critical computer resources necessary to complete all the modeling results in this dissertation. Without their support, it would not have been possible to finish this research prior to transferring to my next command.

I would also like to thank Dr. Richard Spinrad for encouraging me to pursue this degree. Without his dialog, I never would have considered applying for this program.

I would also like to thank the members of my PhD Committee for their persistent guidance and support. I'd especially like to thank the Committee Chair, Dr. Ching-Sang Chiu for his leadership, mentorship and constant support.

Finally, I must thank my wife, Anne, for her unbelievable patience and understanding. She's had to endure countless nights alone while I worked on this research. Without her continued and unconditional love and support, I would never have been able to attain this personal and professional goal.

THIS PAGE INTENTIONALLY LEFT BLANK

I. INTRODUCTION

A. NAVY REQUIREMENTS AND STOCHASTIC APPROACH

Historically, the U.S. Navy has viewed sound propagation through the ocean as a deterministic problem. This antiquated and unrealistic approach not only hinders the warfighter's complete understanding of the acoustic problem, but it also impacts the future design of the U.S. Navy's sonar systems. The Navy's simplistic treatment of sound propagation through a medium needs replacement to reflect a more conventional view that sound propagation through the ocean should be treated stochastically. Although a stochastic approach to sound propagation is not new, it differs from the deterministic approach in that it theorizes that an ocean-acoustic wave guide is in a continuous state of flux so that a once deterministic acoustic signal is quickly transformed into a fluctuating signal in a relatively short distance from its broadcast point of origin (Makris, 1996).

B. STATISTICS OF ACOUSTIC INTENSITY IN A SHALLOW-WATER ENVIRONMENT

The Office of Naval Research (ONR) has funded several studies to investigate the stochastic behavior of sound intensity in shallow-water regimes. Published physical oceanographic results from a 2001 study (Duda et al. (2004a and b)) conducted along the shelf-break in the northeast portion of the South China Sea (SCS) revealed a highly dynamic environment where internal waves of varying spatial and temporal scales dominated the sound-speed field.

Previous studies have determined that the internal wave field on the continental shelf is comprised of nonlinear internal waves originating from two different sources. The first source is simply the local internal tides forced from the barotropic tides. In addition to the local internal tides, tidal flow over the shelf-break from the local internal tides generates localized high-frequency, nonlinear internal waves upon the continental shelf. The second source comes from transbasin nonlinear internal tides that result from the barotropic tidal flow over the sills near the Bataan Islands in the Luzon Strait.

Additionally, if the flow across the sills is strong enough, as it is during "spring tides", sufficient tidal energy exists within the transbasin nonlinear internal tides for the bore wave to transform as it propagates away from the sill into a series of narrow, large amplitude, nonlinear internal depression waves which Ramp et al. (2004) refer to as 'solitons'. Regardless of its shape, the waves associated with the nonlinear internal tides transit across the entire width of the South China Sea and can be observed in the internal wave field on the continental shelf. The interaction among these wave types produced a complex internal wave field upon the continental shelf that would force rapid changes to the acoustic properties of the ocean (Ramp et al., 2004). Additionally, nonlinear interactions between shoaling solitons and the bottom would force these internal waves to evolve from narrow, large amplitude depression waves into much broader wave forms. As the internal waves continue to shoal, the lower layer thins as the thermocline is driven toward the bottom and numerous elevation waves were observed to form behind the lead depression wave once the waves propagated beyond the "critical point" (i.e., where the thickness of the upper and lower layer is equal) (Duda et al., 2004a and b, and Ramp et al., 2004).

In April 2005, an ONR sponsored follow-on experiment (Windy Island Soliton Experiment (WISE)) collected acoustic and physical oceanographic data from a series of moorings in a shallow-water region of the South China Sea inland of the shelf-break (see Section III.A for more information on the experiment). A primary focus of this field experiment was to measure the sound intensity fluctuations associated with a transmitted signal from an acoustic source and determine how various parameters within the ocean-acoustic wave guide influenced the statistics of measured sound intensity.

C.   DISSERTATION OBJECTIVES

1.   First Objective

The first objective of this dissertation is to compare and contrast the sound intensity fluctuations resulting from a transmitted acoustic pulse through nonlinear, elevation internal waves against a signal transmitted through nonlinear, depression internal waves, in terms of phenomenology and statistics.

2.   Second Objective

The second objective of this dissertation is as follows: Expanding upon previously established theories of the statistics of sound intensity fluctuations (Dyer, 1970 and Makris, 1996), propose and validate a hypothesis that relates the variance of the sound intensity level to the number of well-separated arrivals by incorporating critical key parameters such as bandwidth of the received signal (and its effect on the number of resolvable arrivals/degrees of freedom) as well as the temporal separation of the multipath arrivals.

The outline of the paper is as follows. Section II contains a succinct synopsis of relevant literature, previous experiments/studies, and key concepts critical to understanding the results of this research. Sections III and IV correspond with the methodology and results from each of the two dissertation objectives. Section III begins with a discussion on data collection from the five environmental moorings and an examination of the internal wave field. With the end goal of identifying periods when either elevation or depression waves are present along the acoustic path as well as generating a temporally and spatially continuous representation of the sound-speed field, the mooring data is spectrally separated into a tidal and super-tidal bands followed by linear decomposition of the spectral bands. Using the mean sound-speed and dominant temporal and spatial structure of the decomposed sound-speed perturbation time-series, periods when elevation or depression waves occupied the transmission path were identified. Subsequently, the observed statistics of the acoustic intensity as these waves evolved along the transmission path are presented and examined. Finally, through the use of an empirical sound-speed field and a coupled normal-mode acoustic model, Section III concludes with examining the phenomenology of the observed acoustic fluctuations resulting from elevation or depression waves occupying the space near the source or the receiver. Section IV states the proposed hypothesis and how it relates to Dyer's original statistical theory that related the expected statistical distribution of a noise field to the number of spectrally discrete noise sources. Extending this statistical theory to pulse propagation, the proposed theory attempts to relate the number of "resolvable arrivals" resulting from multipath pulse propagation to the statistics of the observed acoustic

intensity. Factors influencing the resolvability of individual arrivals, namely bandwidth of the received signal and fluctuations in the travel time, are examined and discussed. Four different methods of estimating the number of resolvable arrivals from the measured data are examined and the results are compared against the theoretical curve. The conclusions of this dissertation are presented in Section V.

II. BACKGROUND

A. PREVIOUS STUDIES

In late April and May 2001, an extensive experiment, the Asian Sea International Acoustics Experiment (ASIAEX), was conducted in the northeast portion of the South China Sea. Oceanographic and acoustic instruments were deployed by U.S., Taiwan and Singapore scientists, for the purpose of measuring acoustic fluctuations caused by ocean volume variability. Analysis of the environmental data revealed that the sound-speed fluctuations of the South China Sea shelf-slope region in April-May were dominated by two dynamic sources: 1) local internal tides and nonlinear waves excited from internal tidal flow across the nearby shelf-break, and 2) transbasin nonlinear internal tides and waves.

1. Transbasin and Local Internal Tides

Analysis of the ASIAEX data revealed the presence of internal tides of both diurnal and semidiurnal frequencies along the shelf-break in the northeastern South China Sea (Duda et al., 2004a and b). Occasionally, flows induced by the local internal tides would lead to the formation of bores or high-frequency, nonlinear internal waves upon the continental shelf.

2. Transbasin Nonlinear Internal Gravity Waves (Solitons)

Observations along the shelf-break in the northeast portion of the South China Sea revealed the presence of solitons, which Duda et al. (2004a and b) describes as "large-amplitude, nonlinear internal gravity waves." Although the exact generation mechanism is still being researched, these transbasin internal waves appear to originate from the Luzon Strait (Fig. 1). It has been proposed that these internal waves are excited by the strong tidal-current flow initiated during the spring tides across the shallow ridges of the southern portion of the Luzon Strait (Ramp et al., 2004, Chiu et al., 2004, and Duda et al., 2004a and b). The amplitude of these transbasin waves represent some of the largest

internal waves ever observed. Analysis of the ASIAEX data indicated that the solitons transit across the width of the South China Sea, moving west toward the shelf-break and into shallower water.
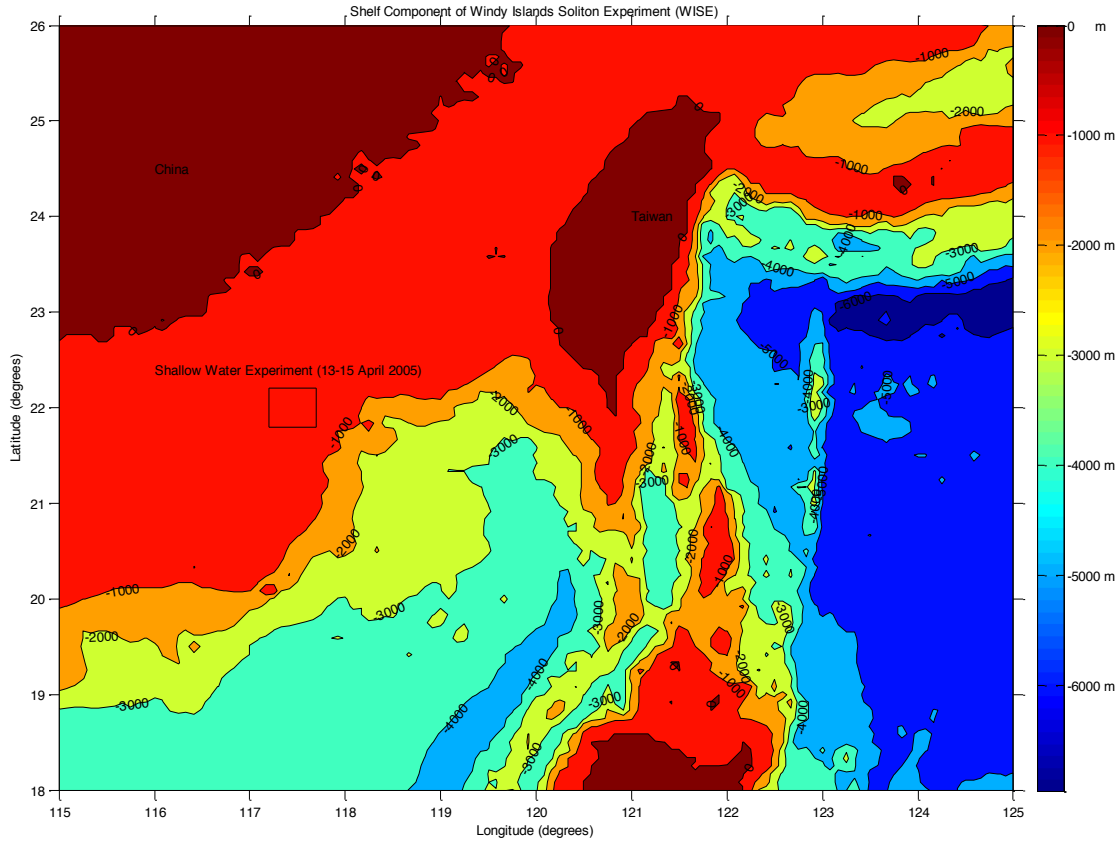
Figure 1.   South China Sea overview. The boxed area near 22°N 117.5°E indicates where the shallow-water component of WISE (13-15 April 2005) was conducted. The contour lines represent isobaths at 1000-m spacing.

As the solitons transition from deep water to shallow water, bottom influences and nonlinear effects begin to change their amplitude, horizontal length scale, and energy as they begin to shoal. Because of the shoaling effects, the amplitude of the depression waves decrease and their width increase as the depression waves move into shallower water and the extent of their amplitude becomes constrained by the bottom. The solitons would continue to decrease in amplitude and broaden until reaching a critical depth, at

which point numerous elevation waves form behind the broad, lead depression wave (Duda et al. 2004a and b, and Ramp et al., 2004). Previous analysis of the ASIAEX data set revealed that the critical depth could be empirically estimated when the thickness of the lower layer and the upper layer were equal. Because internal tides, as well as large amplitude solitons, would continuously force the vertical relocation of the main thermocline, the critical depth, where the transformation would most likely occur, was not a fixed value but rather varied in both space and time.

3. Influences of an Energetic Internal Wave Field on Acoustic Transmissions

The combination of the internal tides and the nonlinear internal waves near the shelf-break produce an extremely dynamic shallow-water environment. The varying temporal and spatial scale processes in a downward refracting medium (forcing numerous bottom interactions), along with the presence of both high-frequency nonlinear elevation and depression waves which dominate the continental shelf region, provided a unique opportunity to study the effects of a rapidly changing ocean-acoustic wave guide (sound-speed field) upon the statistics of the measured acoustic intensity.

While these large amplitude internal waves were propagating through the ASIAEX area, moored and towed acoustic transmitters broadcast both phase-modulated and frequency-modulated acoustic signals, spanning from 50-Hz to 600-Hz, to a hydrophone array positioned near the 120-m isobath. Data analysis revealed how these large amplitude depression waves affected acoustic propagation near the shelf-break. For example, Chiu et al. (2004) demonstrated how depression internal waves bring about a rapid redistribution of acoustic energy through severe mode coupling. Orr et al. (2004) described how rapid fluctuations in horizontal coherence can lead to large fluctuations in array gain. And finally, Duda et al. (2004a and b) correlated scintillation index maxima with large numbers of high amplitude internal gravity waves.

Although the ASIAEX data set and subsequent analysis yielded new insight on the effects of large amplitude internal waves upon acoustic propagation, the data and their relevance to the Navy were limited with respect to shallow-water acoustic propagation.

The ASIAEX acoustic experiment was essentially a slope-propagation experiment as the relevant data were collected orthogonal to the shelf-break and limited to depths between 120-m and 350-m. Unfortunately, insufficient acoustic or physical oceanographic data were collected during ASIAEX that may have provided insight into the evolution of these large amplitude nonlinear internal depression waves into a broad wave packet comprised of both depression and elevation waves as they continued to shoal into shallower water or how they may have affected acoustic transmissions. In April 2005, U.S. and Taiwan scientists attempted to rectify this "data gap" with the advent of the shallow-water component of the Windy Island Soliton Experiment.

B.   ARRIVAL STRUCTURES

In the shallow-water component of WISE, the Naval Postgraduate School (NPS) sound source transmitted a phase-modulated signal at a carrier frequency of 400-Hz with a bandwidth of 100-Hz. The phase modulation employed a 5.11 second, 511 digit pseudo-random sequence corresponding to a compressed pulse of 10-ms resolution after matched-filtering. The received signals, after matched-filter processing, resulted in the multipath and dispersed arrivals of the compressed pulse, i.e., the pulse response (Fig. 2), measured as a function of depth and time (Chiu et al., 2004). The pulse response is also referred to as an arrival structure. Since each arrival structure represents the multipath spread of a single transmitted phase-modulated signal, it follows that a series of "x" transmissions of a phase-modulated signal will result in a sample population of "x" arrival structures, where "x" is simply an integer. It should be noted that an arrival may represents a single ray or mode, or it could be comprised of a group of ray/modes coherently summed.

C.   PULSE-WIDTH OF A COMPRESSED PULSE

An inverse relationship exists between a signal's bandwidth and the temporal resolution (i.e., the pulse-width) of the arrival after matched-filtering. Decreasing (increasing) the bandwidth of the phase-modulated signal would result in arrival with a wider (narrower) pulse-width (i.e., temporal resolution). Therefore, a series of arrivals

that are broader (narrower) due to a decreased (increased) bandwidth will have a greater (lesser) tendency to overlap with adjacent arrivals, reducing (increasing) the number of temporally disjoint arrivals.
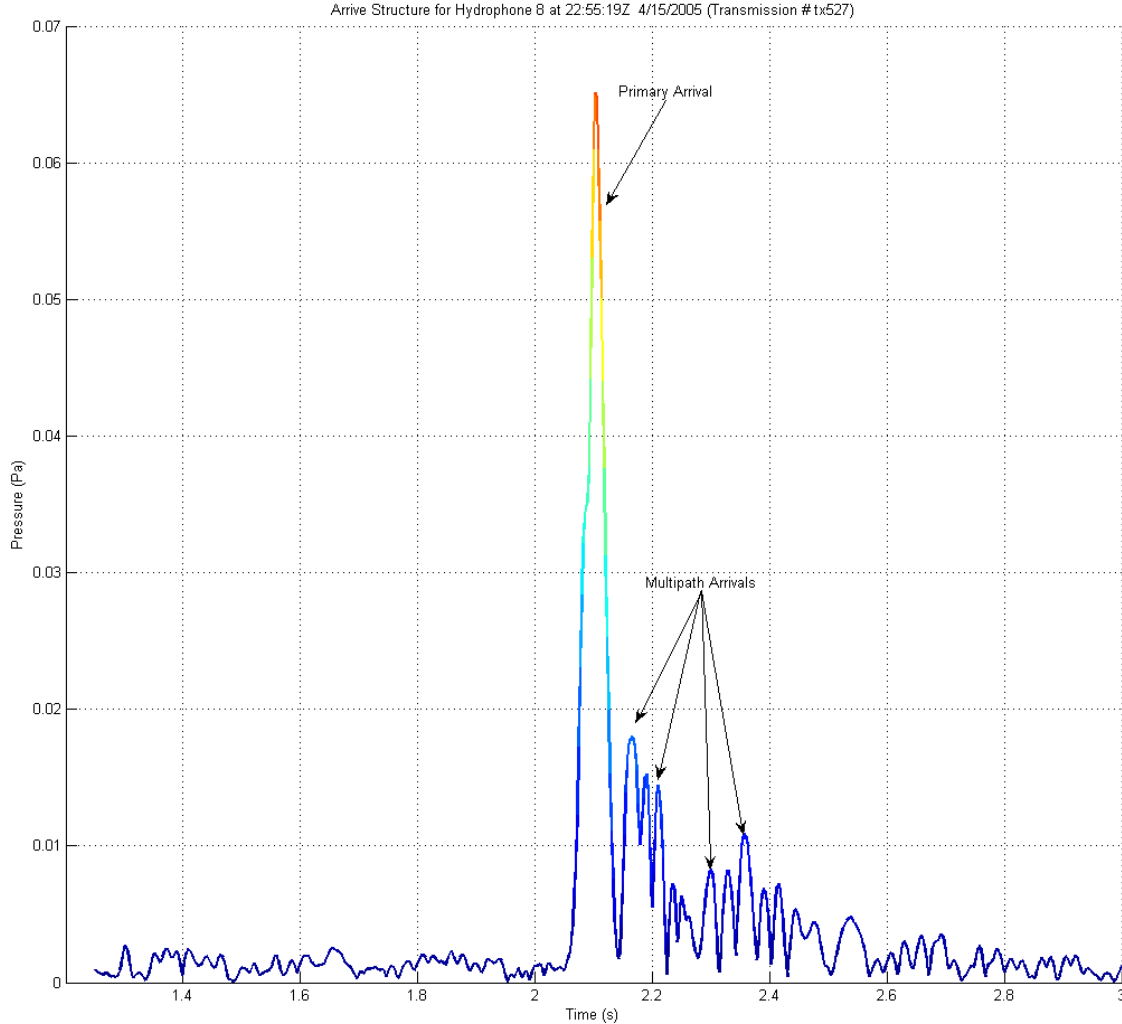
Figure 2.   An example of an arrival structure/pulse response collected during the shallow-water component of WISE. The peaks after 2.1-s represent the various arrivals separated in time due to multipath propagation. The arrivals may represent a single ray or mode, or it could be comprised of a group of ray/modes coherently summed.

D.   SOUND INTENSITY (SI) AND SOUND INTENSITY LEVEL (SIL)

For this study, the sound intensity (SI) is defined as:

$$SI = \frac{1}{T} \int_T p^2(t) \cdot dt$$

and sound intensity level (SIL) is defined as:

$$SIL = 10 \log \left(\frac{\frac{1}{T} \int_T p^2(t) \cdot dt}{(1 \mu Pa)^2} \right)$$

where T is the desired integration time (time difference between the leading edge of the first and the trailing edge of the last arrival of interest), and p is the sound pressure of the signal segment in the matched-filter output. When the output of the matched-filter is properly normalized, the SIL can be directly related to the transmission loss if the equivalent source level (SL_e) is known. The equivalent source level (SL_e) is defined as:

$$SL_e = SL + 10 \log \left(\frac{\tau_0}{T} \right)$$

and source level (SL) is defined as:

$$SL = 10 \log \left(\frac{\frac{1}{\tau_0} \int_{\tau_0} p_{r_0}^2(t) \cdot dt}{(1 \mu Pa)^2} \right)$$

where τ_0 is pulse-width of the compressed pulse (i.e., 10-ms), T is the multipath spread, and p_{r_0} is the sound pressure of the compressed pulse at a range of 1-m from the source. With these defined values, the relationship to transform transmission loss (i.e., the model output) to a modeled sound intensity level is simply, $SIL = SL_e - TL$. Note that T (integration time) is part of the time-bandwidth product (see next paragraph).

E. TIME-BANDWIDTH PRODUCT

The time-bandwidth product (TBWP) of a signal is defined as the product of the duration of that signal and the spectral width (bandwidth) of the medium in which the signal is propagating (ocean waveguide). The spectral width is simply the inverse of the coherence time of the ocean and the duration is the integration time used when calculating sound intensity (level). Coherence times of the ocean vary depending upon the geographic location. Typical values for the coherence time of the deep ocean, where low frequency, mesoscale processes dominate, are of the order of 15-30 minutes. Values of one-to-five minutes are more typical in shallower regions where higher frequency, local processes tend to determine the coherence time.

The coherence time of the ocean along the transmission path for the shallow-water experiment was determined to be around 45 seconds. The integration times used to calculate sound intensity was less than one second. Using an assumed upper limit of one second for the integration time and a coherence time of 45 seconds, the spectral width is 1/45 Hz and the TBWP was much less than unity. Following the results published by Makris (1996), when the measurement time (or in the case of this study, integration time) is much less than the coherence time, the assumption that the TBWP is equal to unity becomes a very good approximation. The TBWP of this study is thus taken to be unity.

F. PRE-EXISTING STATISTICAL THEORIES ON SOUND INTENSITY FLUCTUATIONS

As concluded by Makris (1996), the results of Dyer's statistical treatment are limited to scenarios when the TBWP is equal to unity. The main focus of Makris' work is to expand upon Dyer's theory (1970) by considering longer integration times where the TBWP exceeds unity. Because the TBWP of this study does not exceed unity, the resulting statistical analysis of the acoustic data collected during the shallow-water component of WISE is expected to follow the results published by Dyer.

THIS PAGE INTENTIONALLY LEFT BLANK

III. OBJECTIVE ONE: COMPARE AND CONTRAST THE PHENOMENOLOGY AND STATISTICS RESULTING FROM AN ELEVATION AND DEPRESSION WAVE EVENT

In order to meet the objectives of this study, analysis of both observed sound intensity measurements and modeled sound intensity were required. When portions of this study required the use of an acoustic model, modeled output was compared and checked for consistency against in-situ measurements to ensure the model output was a reasonable estimate of the observed field. The specific acoustic model used in this study and the necessary data fields necessary to initialize the acoustic model are discussed in Section III.D.1.

A. DATA COLLECTION: WINDY ISLAND SOLITON EXPERIMENT (WISE)

The Windy Island Soliton Experiment was designed by Taiwan and U.S. physical oceanographers to observe the generation, evolution and transformation of transbasin, nonlinear waves in the northeastern South China Sea beginning April 2005 (Fig. 1). Until April 2005, no experiment had ever been specifically designed by the scientific community investigate the observed fluctuations resulting from transmitting an acoustic signal through nonlinear, elevation internal waves. WISE was delineated into two separate acoustic experiments, a shallow-water component (mid-April 2005), and a deep basin experiment (April 2005 – October 2006), respectively.

1. Deep Basin Experiment (April 2005 – October 2006)

Because this dissertation focuses on the data collected during the shallow-water component of WISE, the basin experiment will not be referred to again. However, for completeness, the following is provided: the objective of the deep basin experiment (April 2005 – October 2006) was to study and characterize the super-tidal to seasonal scale impacts of the transbasin, nonlinear internal waves on long range transmission loss, and to help monitor the evolution of the transbasin internal waves in the basin's interior.

13

2.   Shallow-water Component of WISE (13-15 April 2005)

The purpose of the shallow-water component of WISE was to study the physics of sound propagation through nonlinear, elevation internal waves in shallow-water, and to quantify the associated fluctuations of the sound intensity. Beginning on April 13, 2005, the data collection was conducted over a three day period, prior to the deep basin experiment. The following is a list of the acoustic and physical oceanographic equipment deployed during the shallow-water component. It should be noted that analysis of the radar images (not shown) collected onboard the Ocean Researcher 1 indicated that the direction of travel for the majority of the waves in the internal wave field was roughly normal to the bathymetric contours (i.e., from the east-southeast toward the west-northwest). Thus the propagation of the acoustic signal was approximately perpendicular to the wave fronts of the majority of the waves in the internal wave field.

a.   NPS 400-Hz SYS13 Sound Source

The sound source deployed for the shelf experiment was a 400-Hz source manufactured by Webb Research Corporation (WRC) belonging to NPS. This source has 100-Hz bandwidth, and transmits a 5.11 second, 511 digit pseudo-random (m-sequence) signal at 180 dB re 1 µPa. In order to assure an adequate collection of acoustic samples, the sound source transmitted 30 continuous m-sequence signals lasting 153.3 seconds (or approximately 2 ½ minutes) every five minutes during the three day deployment.

During ASIAEX, elevation internal waves were observed to form near the 120-m isobath. In an attempt to ensure that the transmission path would be located "inland" of this previously observed critical depth, the sound source was deployed along the 110-m isobath (Figs. 3-4).

b.   NPS Eight Element, Vertical Line Array (VLA)

An eight element, vertical line array (VLA) was deployed in 88-m of water (Fig. 4). Hydrophone spacing was eight meters between each phone resulting in an acoustic aperture of 56-m. With the deepest hydrophone 11.5-m above the bottom and a

surveyed bottom depth of 88-m, the depths of the hydrophones were 20.5-m, 28.5-m, 36.5-m, 44.5-m, 52.5-m, 60.5-m, 68.5-m and 76.5-m respectively. To facilitate analysis later in this paper, the water column was subdivided into three vertical sections, the upper portion (surface to 30-m), the middle portion (30-m to 60-m) and the lower portion (60-m to bottom) of the water column. The eight channel VLA digitizer sampled the acoustic field at 2000-Hz.

Originally, the 400-Hz sound source and the vertical line array were to be separated by a distance of 20-km; however, depth restrictions of the hydrophone array forced the VLA to be deployed on a deeper portion of the shelf. The final distance between the surveyed positions of the sound source and the VLA was approximately 17.1-km.
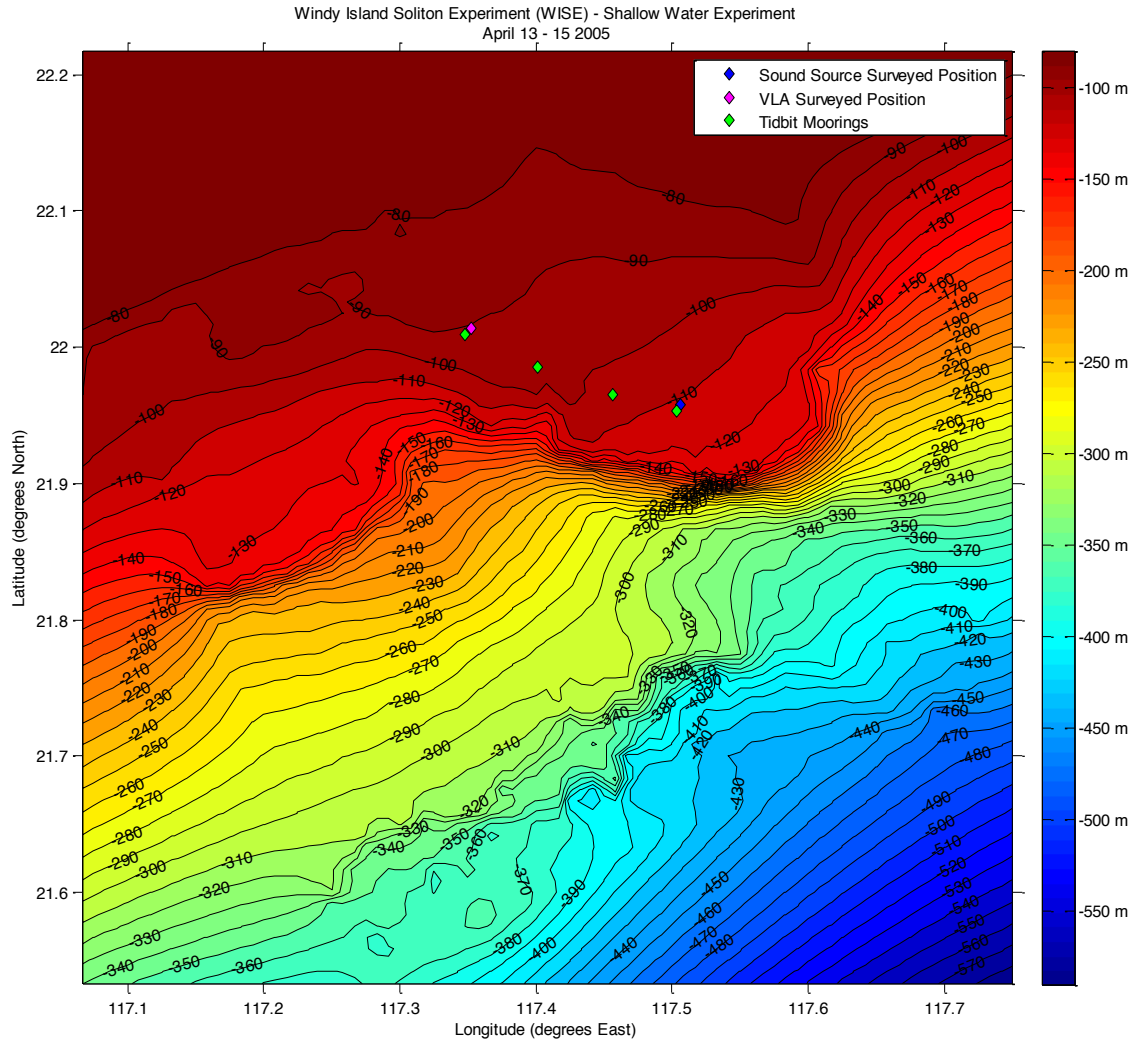
Figure 3. Plane-view of the instrument orientation for the shallow-water component of WISE. The blue, green and magenta diamonds represent the sound source mooring, the TidbiT temperature moorings and the VLA mooring, respectively. The contours represent the isobaths and are depicted every 10 meters.
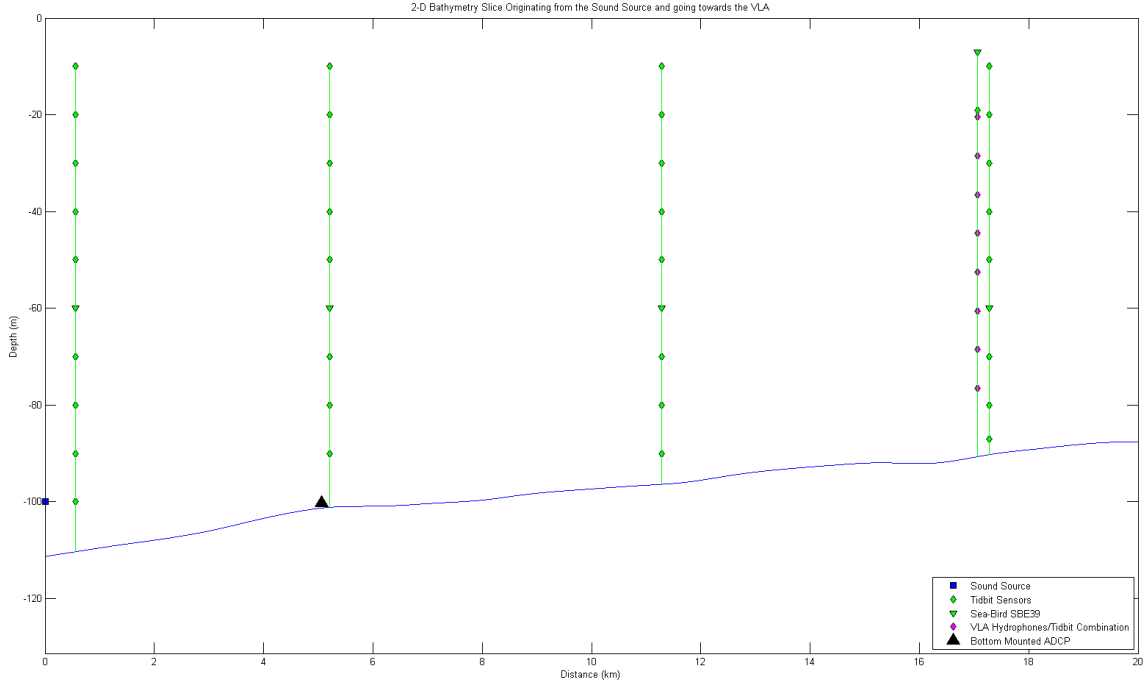
Figure 4.   2-D depth vs. range "slice" oriented downrange from the sound source. The bottom bathymetry is shown as the blue curve. The sound source mooring has been placed at the origin with the sound source (blue square) positioned at a depth of 100 meters (10 meters off the bottom). Starting from the origin, the S, T1, T2, VLA and T3 moorings have been plotted. The TidbiT sensors and the VLA hydrophones/TidbiT pairs are plotted as green and magenta diamonds, respectively. The SBE-39s are indicated by the inverted green triangle. A bottom-mounted Acoustic Doppler Current Profiler was deployed near the T1 mooring (black triangle). The horizontal axis is distance (km) and the vertical axis is the water depth (m).

c.   Oceanographic Data

(1) Temperature Data. Temperature data were collected from two types of sensors (SBE-39 and TidbiT) located on multiple moorings. There were a total of four dedicated temperature moorings deployed. Starting from the vicinity of the sound source mooring and heading toward the VLA mooring, they were S, T1, T2, and T3, respectively. Additionally, temperature sensors were placed near each hydrophone along the VLA mooring, providing a fifth vertical temperature profile (Fig. 4).

The main temperature sensor used on all five temperature moorings were the Onset Computer Corporation's StowAway TidbiT temperature logger.

17

Although capable of sampling every 30 seconds, a previous study conducted by Woods Hole Oceanographic Institution (WHOI) determined the temperature response time of the sensor to be approximately 10 minutes. Consequently, the TidbiT units were set to sample at depth at 10 minute intervals.

More frequent temperature sampling was performed by the use of five SeaBird SBE-39 temperature sensors. Four SBE-39s were deployed at 60-m on the S, T1, T2, and T3 mooring. The fifth SBE-39 was attached to the VLA mooring and was deployed at 7-m (Fig. 4). The SBE-39s sampled the water column every 30 seconds throughout the three day experiment.

(2) Current Data. An upward facing, bottom-mounted Acoustic Doppler Current Profiler (ADCP) was deployed next to the T1 mooring (Fig. 4). With a sampling rate of two samples per minute and a vertical spacing between samples of 4-m, the ADCP measured the horizontal and vertical velocity of the ocean currents during the three day experiment.

B.   CHARACTERISTICS OF THE OBSERVED SOUND-SPEED FIELD

The first step in this objective was to properly identify when either elevation or depression waves enter and evolve along the acoustic path. Figure 5 shows the temperature time-series for each of the five environmental moorings. The poor temporal resolution due to the low sampling rate of the TidbiT sensors made it difficult to properly identify when a series of high frequency elevation or depression waves were occupying the acoustic path using the raw data. Using the technique published by Chiu et al. (2004), the temperature time-series, after being converted into a sound-speed time-series, was spectrally decomposed into the mean sound-speed profile, and a low frequency and high frequency sound-speed perturbation time-series. The linear decomposition of the sound-speed field not only aided in the proper identification of elevation/depression wave episodes, but the decomposed fields were later used to develop a spatially and temporally continuous empirical sound-speed field along the transmission path that could be used in the acoustic model. This method is discussed next.
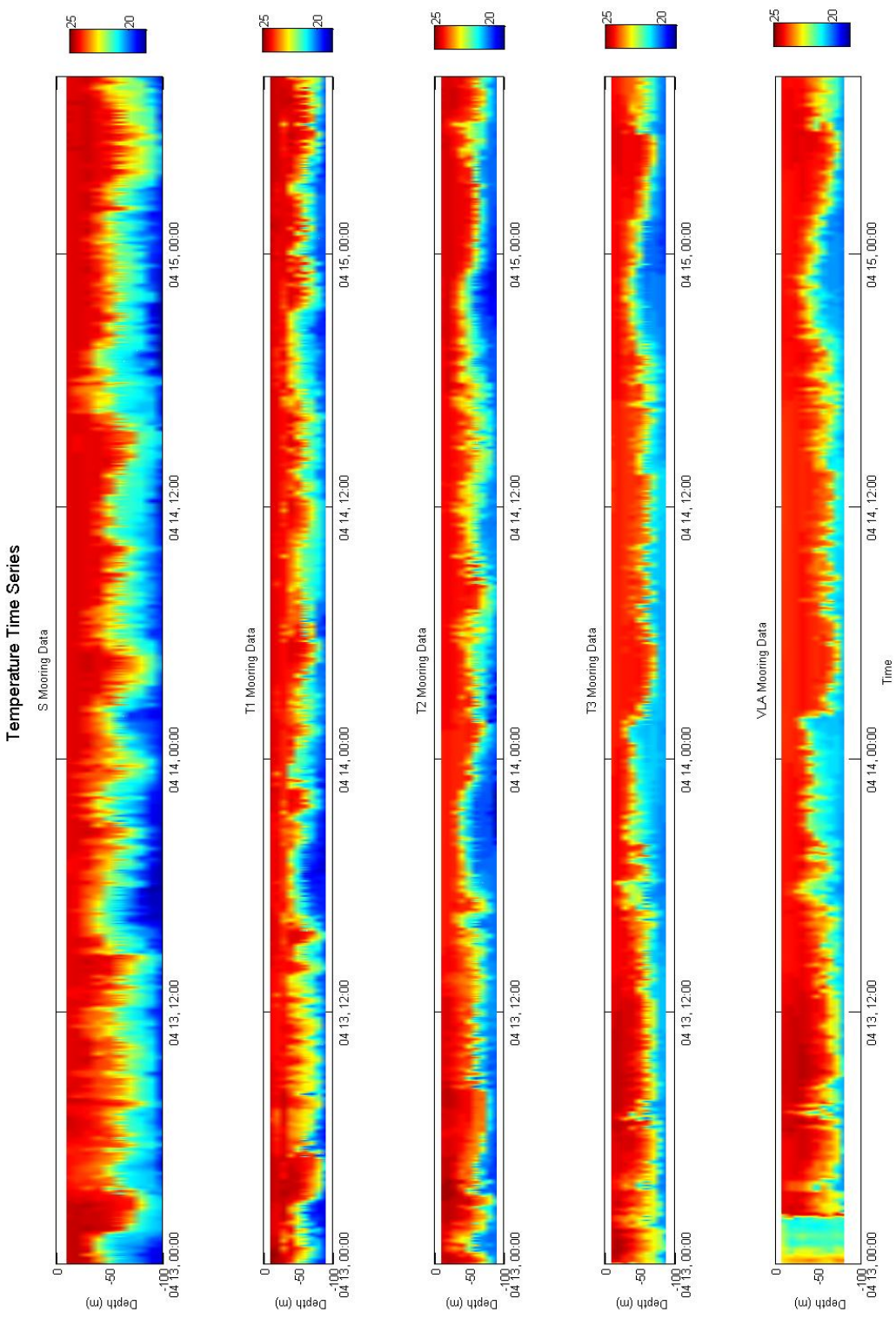
Figure 5.   Temperature time-series measured in Celsius (°C) recorded by the five environmental moorings. The horizontal axis is time (GMT). Depth (m) is on the vertical axis.

1. Empirical Orthogonal Function Decomposition of the Sound-speed Time-series

Spectral densities of the sound-speed time-series calculated from the temperature data recorded by the SBE-39s located on the five moorings were used to aid in the proper selection of the two spectral bands. Spectral analysis (Fig. 6) of the three day time-series was expected to reveal two spectral bands, namely, tidal (i.e., internal tides) and super-tidal (i.e., internal waves) processes (Note that a consistent color scheme of red, blue, green, magenta and light blue is used in this Section to denote the data from S, T1, T2, T3 and the VLA moorings, respectively). The temperature time-series recorded at each of the five environmental mooring were converted into sound-speed time-series using an empirical formula (Medwin, 1975) and an approximate salinity value of 35 psu. Spectral peaks are clearly evident at 1, 2, 3 and 4 cycles per day (cpd) which are associated with the diurnal, semi-diurnal internal tides and higher order tidal harmonics observed on the continental shelf. The spectral energy found in the frequency bands above four cpd diffuses rapidly and is associated with higher frequency internal waves. Consequently, the tidal band was defined to have a period longer than 5 cpd, whereas the super-tidal band was defined to have periods shorter than 5 cpd. The use of 5 cpd to separate the two spectral bands is consistent with the results published by Chiu et al. (2004). It is interesting to note the vertical energy distribution measured by SBE-39s. Four of the SBE-39s were located in the lower half of the water-column (60-m) where the Brunt-Vaisala buoyancy frequency was observed to have a maximum. The fifth SBE-39 was deployed at a much shallower depth (near the top of the VLA mooring (7-m)) with the intention to help in the determination of mooring motion from the pressure measurements. As expected, the higher energy measured across all spectral bands by the deeper temperature sensors suggests that the sound-speed perturbation maxima for both bands will be found in the lower half of the water column.
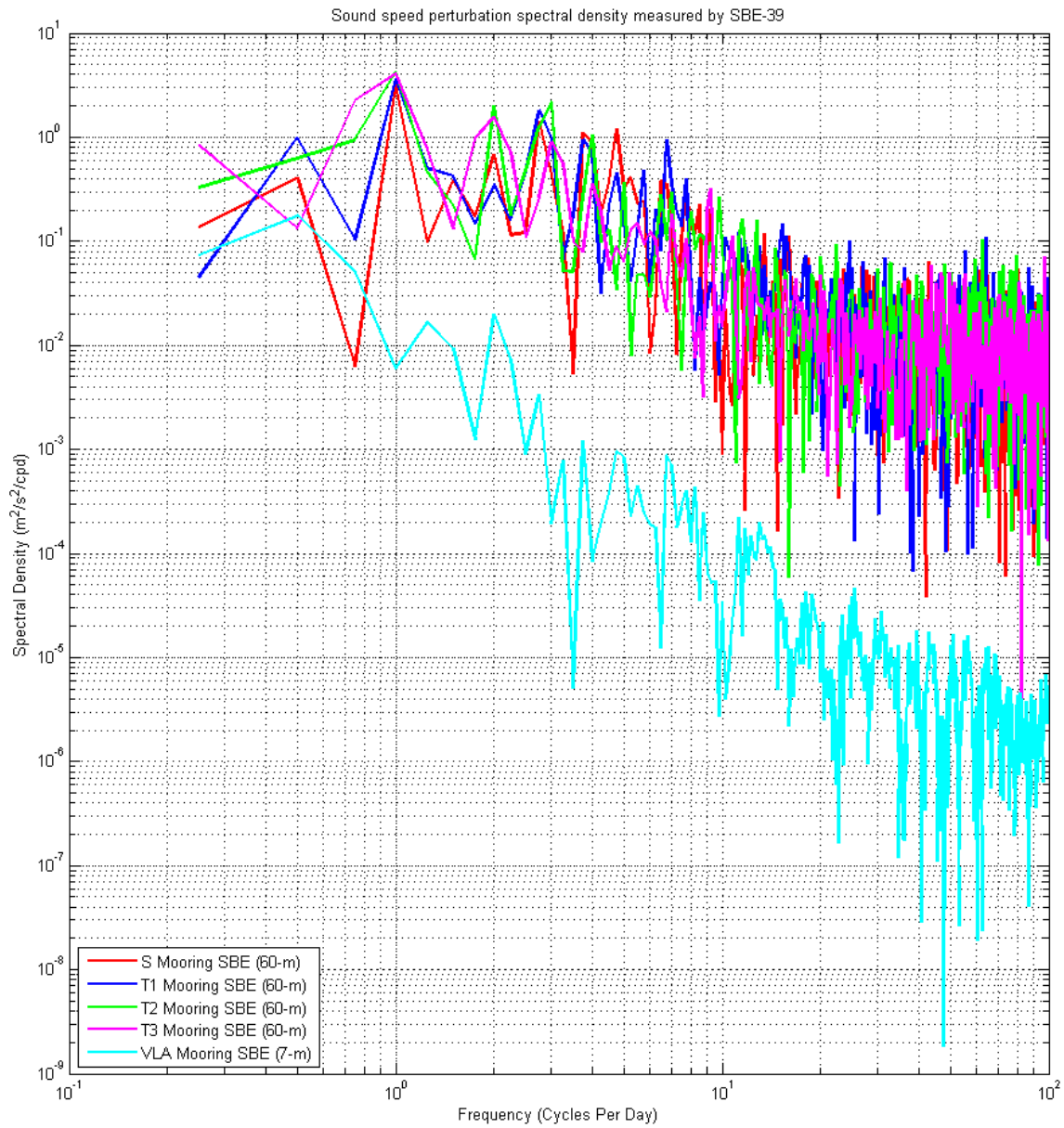
Figure 6.   Spectral density of the calculated sound-speed time-series based on the data recorded by the five SBE-39s located on the S mooring (red), T1 mooring (blue), T2 mooring (green), T3 mooring (magenta) and the VLA mooring (light blue). Note that the SBE-39 on the VLA mooring was significantly shallower (positioned at 7-m) than the SBE-39s on the other four environmental moorings (positioned at 60-m).

21

Based on two spectral bands, the sound-speed time-series for each mooring was expanded into a linear summation of the mean profile, $\bar{c}$, plus the perturbation components:

$$c(r,z,t) = \bar{c}(r,z) + \delta c_T(r,z,t) + \delta c_{IW}(r,z,t) \qquad (1)$$

where δc_T and δc_{IW} represent the variations of the sound-speed contributed by the tidal and super-tidal (i.e., internal waves), respectively, in non-overlapping frequency bands. The mooring's horizontal distance from the sound source is defined by r, z is depth and t is time. Furthermore, for each frequency band, i, and for each mooring location, r, the sound-speed perturbation time-series, δc_i, can then be decomposed into a linear combination of vertical, empirical orthogonal functions (EOFs) or modes, $f_n^{(i)}$, weighted by the corresponding amplitude time-series, $a_n^{(i)}$.

$$\delta c_i(r,z,t) = \sum_{n=1}^{N} a_n^{(i)}(r,t) \cdot f_n^{(i)}(z,r) \qquad (2)$$

The EOFs and their amplitudes were obtained using principal component analysis followed by projecting the data on the EOFs. Because the sampling rates differed between the SBE-39 sensors (sampling every 30 seconds) and the TidbiT sensors (sampling every 10 minutes), the data were linearly interpolated to a common sampling rate of 30 seconds prior to the EOF decomposition which essentially low-pass filtered the sound-speed time-series. Thus any internal wave with a period less then 10 minutes would not be accounted for in the linearly decomposed sound-speed time-series for each of the environmental moorings. Once the interpolated sound-speed time-series were generated, temporal and spatial structures of the sound-speed field were separated into the mean sound-speed profile and sound-speed perturbation in the tidal and internal wave bands using butterworth filters at each environmental mooring.

Figure 7 shows the mean sound-speed profile for all five of the environmental moorings. All five sound-speed profiles are nearly identical to each other indicating a strong, downward refracting, range-independent mean sound-speed field along the transmission path.

22
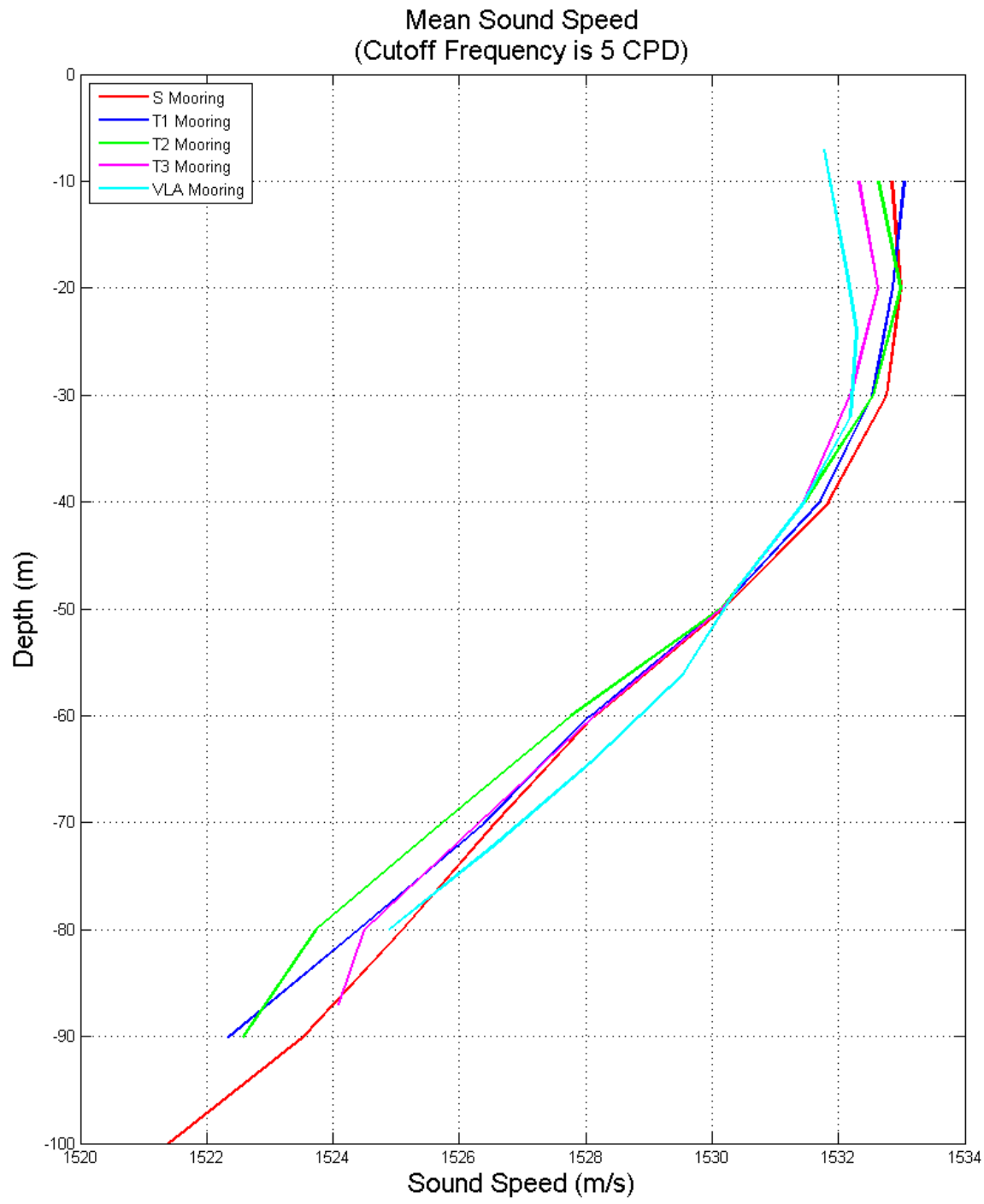
Figure 7.   Mean sound-speed profile measured at the S mooring (red), T1 mooring (blue), T2 mooring (green), T3 mooring (magenta) and the VLA mooring (light blue).

Similar to the results found by Chiu et al. (2004), EOF decomposition of the sound-speed perturbations proved to be an effective way to represent the vertical structure and its associated temporal fluctuations within each spectral band. Table 1 shows the amount of temporal variance captured by the first two modes in both the tidal and super-tidal bands. In the tidal band, over 92% of the temporal variance at each of the five environmental moorings was captured in just the first two modes. The higher frequency band was almost as good, with 73% (or higher) of the variance captured within the first two modes. Ignoring the VLA mooring, the principal mode (i.e., mode 1) alone captured over 80% (57%) of the sound-speed perturbation variance found in the tidal (super-tidal) band. For both the tidal and super-tidal bands, the principal mode modal maxima was consistently located at 60-m along the transmission path. The 60-m correlated well with the depth where the previously measured Brunt-Vaisala buoyancy frequency reaches the maximum value (Fig. 8).

Further analysis of the EOF decomposition revealed a couple of additional significant findings. First, the amount of variance captured by the first mode for both spectral bands was range dependent. A larger portion of the temporal variance is captured by the principal mode from the deeper moorings (i.e., moorings S and T1); however, examination of the remaining moorings reveals that the amount of temporal variance captured by the first mode decreases as the water depth decreases. This result suggests that as the waves travel toward shallower water, the bottom is modifying their structure and transferring energy into higher empirical modes (i.e., Mode 2, Mode 3, etc). Secondly, although the first two modes from the VLA mooring and the T3 mooring captured 93% (73%) of the variance in the tidal (super-tidal) band, there was a distinct difference between the percentage of variance captured by the principal mode when comparing the EOF decomposition of the sound-speed perturbation field measured by the T3 mooring and the VLA mooring. The principal mode from the VLA mooring captured between 15% (2%) less than the first mode in the tidal (super-tidal) band from the T3 mooring. This difference will be an important consideration when "tuning" the empirical sound-speed model.

Mooring	Tidal		Super-Tidal		Variance Captured from Modes 1 & 2	
	Mode 1	Mode 2	Mode 1	Mode 2	Tidal	Super-Tidal
S	85.1%	7.4%	69.4%	9.6%	92.5%	79.0%
T1	84.8%	8.8%	68.8%	8.9%	93.6%	77.7%
T2	80.3%	12.7%	68.8%	9.5%	93.0%	78.3%
T3	80.0%	12.5%	57.3%	15.3%	92.5%	72.6%
VLA	65.7%	27.3%	55.4%	18.7%	93.0%	74.1%

Table 1.   Variance captured (percentage) per spectral band by the first two modes.

In a previous study, Chiu et al. (2004) was able to use the amplitude time-series from his study (May 8, 2001, respectively) to isolate and track large amplitude solitons (i.e., individual waves) as they traveled from the deeper South China Sea basin across the shelf-break. Analysis of the dominant modal amplitude, $a_1^{(i)}$ with $i = iw$ (Fig. 9, right), indicated that the super-tidal amplitude time-series from Chiu's study and the super-tidal amplitude time-series from this study were radically dissimilar. In Chiu's study, the large amplitude transbasin solitons dominated the deep water, high-frequency internal wave field found just off the shelf-break. Conversely, the complex, internal wave field observed on the shelf during the shallow-water component of WISE was composed of numerous smaller amplitude internal waves originating from various sources. As previously mentioned in Section II.A.2, it was expected (and had been previously observed during ASIAEX, Ramp et al. (2004)) that the observed high frequency internal wave field on the shelf would be a complex wave field comprised of shoaling transbasin solitons, the associated elevation waves forming behind the shoaling transbasin solitons, local internal tides and internal waves excited by internal tides flowing over the nearby shelf-break. All of these processes facilitate the generation of a complex, energetic internal wave field inside the shelf-break. Although the method of using the dominant

modal amplitude, $a_1^{(i)}$ time-series to track individual elevation or depression waves along the acoustic path as outlined by Chiu et al. (2004) proved unfeasible due to the complex internal wave field observed on the shelf, the EOF decomposition was able to clearly identify elevation and depression wave packets (i.e., episodes) once the sound-speed time-series was reconstructed using equation (1) and the dominant mode for each spectral band (Fig. 8). Analysis of this field is discussed next.
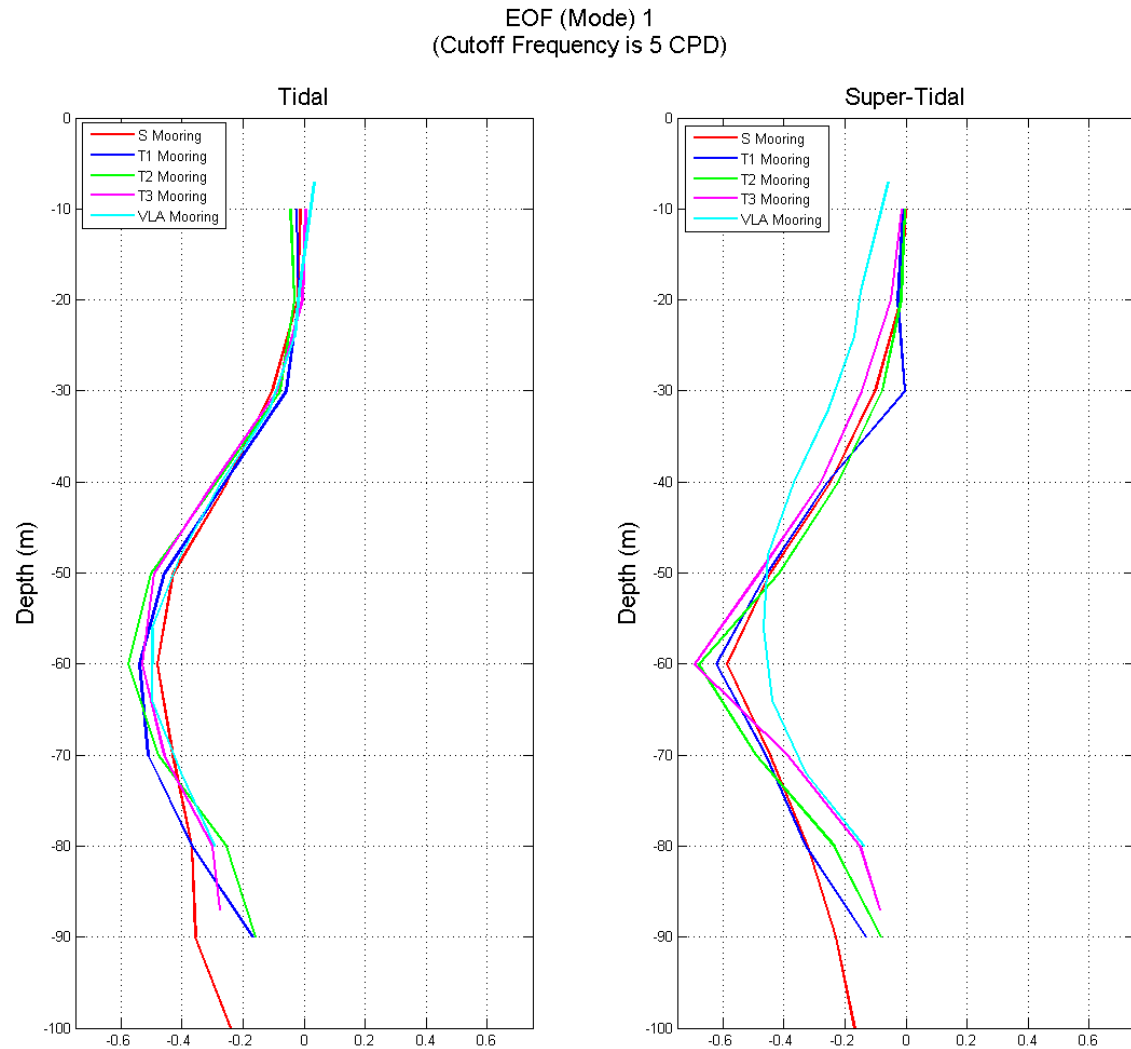
Figure 8.   Principal mode (i.e., mode 1) vertical structure based on the EOF decomposition of the sound-speed perturbation time-series measured at each mooring. The principal mode for the tidal band is on the left and principal mode for the super-tidal band is on the right.

27
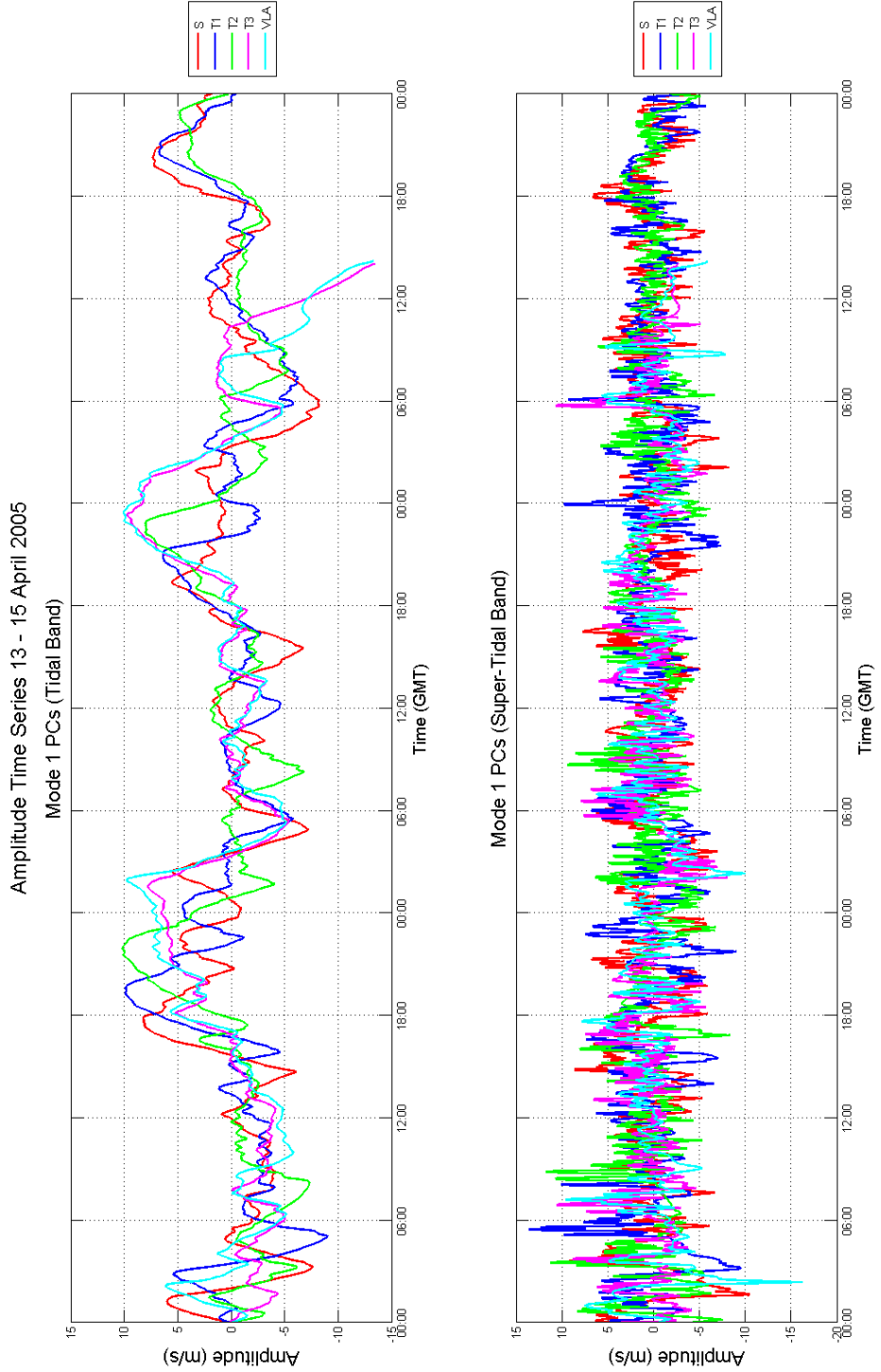
Figure 9.   Spanning 13-15 April 2005, the amplitude (Principal Component) time-series of the principal mode associated with the tidal (left figure) and super-tidal (right figure) band. Starting from the sound source and continuing along the transmission path are the S (red), T1 (blue), T2 (green), VLA (light blue) and T3 (magenta) moorings.

2. Identifying Periods when Elevation Waves and/or Depression Waves Occupy the Acoustic Path

Examination of the mode 1 sound-speed time-series identified two periods (white and light blue arrow in Fig. 10, respectively) when the thermocline was depressed and a series of elevation waves were found along the transmission path. In both cases, a series of depression waves enter the acoustic path near the S mooring (Case 1: from approximately 06:00 until 15:00 on April 13; Case 2: 21:00 on 13 April until 05:00 on 14 April). As the depression waves evolve along the acoustic path into shallower water, the depression waves begin to widen and compress the sound-channel toward the bottom. By the time the depression waves reach the T2 mooring, the depression waves have expanded significantly and several elevation waves have formed behind the lead depression wave. As the depression wave continues to move toward the VLA (or the nearly adjacent T3 mooring, the shoaling depression wave continues to expand horizontally resulting in a broad region where the sound-channel is compacted and the trailing elevation waves have become more pronounced. This is especially apparent when examining the reconstructed sound-speed time-series for the T3 mooring from 06:00 – 13:00 on April 14 (Fig. 10). This wave transformation is consistent with the observations published by Ramp et al. (2004) during ASIAEX. The subsequent analysis and discussion will focus on the elevation waves found in Case 2 for several reasons. First, the elevation waves in Case 2 appear stronger in amplitude and are well defined. Second, prior to the entrance of broadening depression wave, a time period exists of little internal wave activity. The thermocline remains relatively fixed at 40-m for several hours prior to the entrance of the leading edge of the depression wave observed on the S mooring at approximately 20:00 on April 13. This "calm period" should contribute minimal fluctuations to the observed sound intensity. Lastly, although the experiment was conducted over three days, the record length of the data collected by the environmental moorings did not cover the entire three day experiment due to mooring recovery. This abbreviated time-series placed temporal constraints on the empirical sound-speed model (which will be discussed in further detail in Section III.D). Case 2 occurs near the middle of the experiment when there is sufficient acoustic and environmental data to properly

29

examine how elevation wave packets induce fluctuations in the observed acoustic intensity and the phenomenology behind it. (It should be noted that the sound-speed time-series for the VLA mooring stops abruptly shortly after 08:00 on April 15. This "data gap" corresponds with the mooring recovery).

Now that a period has been identified when elevation waves occupy the acoustic path, the next step is to identify a period when depression wave(s) are observed along the acoustic path. The depression wave observed at the S mooring around 14:00 on April 13, 2005 was chosen for a few reasons (red arrow, Fig. 10). First, this depression wave maintains its structure as a depression wave as it travels along the acoustic path into shallower water. Unlike the transforming depression waves observed during elevation wave case study, this depression wave does not transform into a broader depression wave and elevation waves do not form behind it. Second, a calm period of minimal internal wave activity exists following the passage of this depression wave at each of the environmental moorings. As can be observed from the T3 mooring in Fig. 10, the depression wave exits the acoustic path at approximately 18:00 on 13 April. This occurs roughly the same time as the series of transforming depression waves indentified earlier in the elevation case study enters the acoustic path (i.e. approximately 18:00 at the S mooring). Finally, the depression wave occurs when there is sufficient environmental and acoustic data to support statistical and physical analysis of the sound intensity fluctuations.

Thus an extended period has been identified (i.e., approximately from 14:00 on April 13 through 13:00 on April 14) where a series of elevation wave packets or depression wave packets occupies the transmission path. The next Section will discuss the statistical analysis of sound intensity fluctuations which was accomplished by examining the data collected by the vertical line array (VLA). The characteristics of the sound intensity field during this extended period will be discussed next.
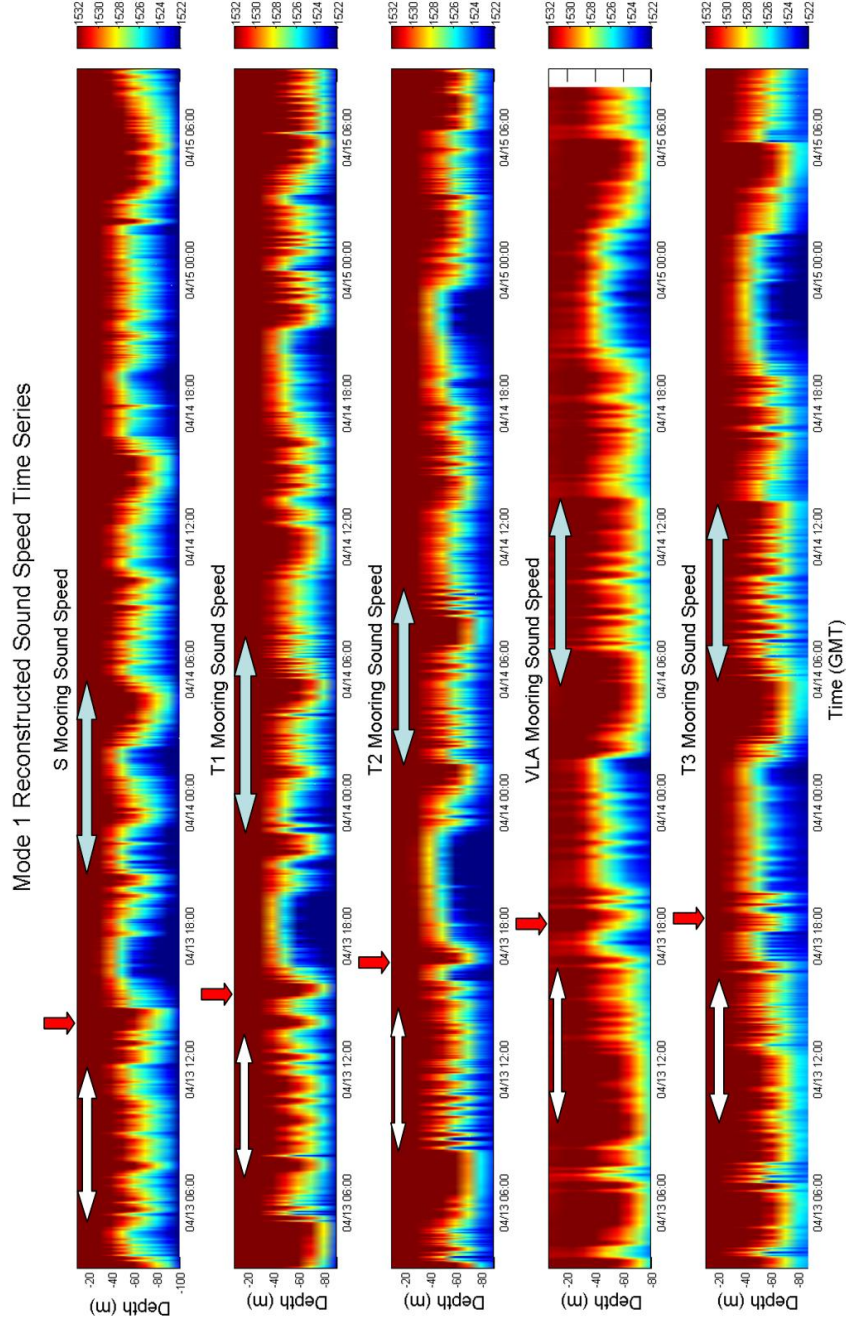
Figure 10.   Reconstructed sound-speed time-series for each of the five environmental moorings using only the dominant mode and its associated amplitude time-series. The time-series begins at 00:00, April 13, 2005 and ends at 12:00, April 15, 2005. The far left graph starts near the sound source (S mooring) and each consecutive figure follows along the transmission path (i.e., T1, T2, VLA, and T3 mooring). Two periods where elevation waves form along the acoustic path have been identified: Case 1 (white arrow) and Case 2 (light blue arrow). Additionally, a depression wave transiting along the acoustic path has been identified (red arrow).

31

C. CHARACTERISTICS OF THE SOUND INTENSITY

The 400-Hz sound source began its broadcast schedule at 03:00 (GMT) on April 13, 2005. The VLA digitizer recorded the acoustic transmissions from the sound source for approximately the next 53 hours until the VLA mooring was recovered at 08:20 (GMT) on April 15, 2005. Initial examination of the recorded sound pressure fields by the VLA digitizer revealed that the top five hydrophones experienced a sporadic hardware failure during the experiment. An example of this is depicted in Fig. 11. Both spikes and shorts could be seen in the raw voltage data. Post-experiment examination of the hydrophone array revealed wire damage to the array termination (which most likely occurred during deployment) which resulted in the intermittent failure to hydrophones 1 thru 5. Obviously, the observed voltage spikes and shorts in the hydrophone data would need to be removed from the VLA data set. Otherwise, the calculated sound intensity measurements from the hydrophone data would contain significant errors. The procedure describing how these corrupted segments were removed from the raw data is discussed next.

Both objectives of this dissertation focus on the characteristics of the sound intensity statistics. For any calculated statistical measurement, the confidence level associated with that value is dependent upon the number of samples used to derive it. Consequently, in order to ensure a high degree of confidence in the statistical analysis of this dissertation, only the corrupted segments were removed in order to maintain the largest possible sample population. Remembering that each sound source transmission was comprised of thirty 5.11 second m-sequences, the voltage time-series was subdivided into 30 segments, each with a period of 5.11 seconds. Each of these 30 segments was individually checked for either spikes in the voltage recordings or shorts. If a spike or short was found in the 5.11 second recording, the data segment was thrown out. The end result was removing corrupted transmission recordings while maintaining the largest possible sample population. With a maximum number of 30 m-sequences per transmission, Fig. 12 shows the percentage of good m-sequences that were recorded by

each of the hydrophones over the three day experiment. Because of the wiring damage, no acoustic data was collected from the majority of the middle to upper portion of the water column.
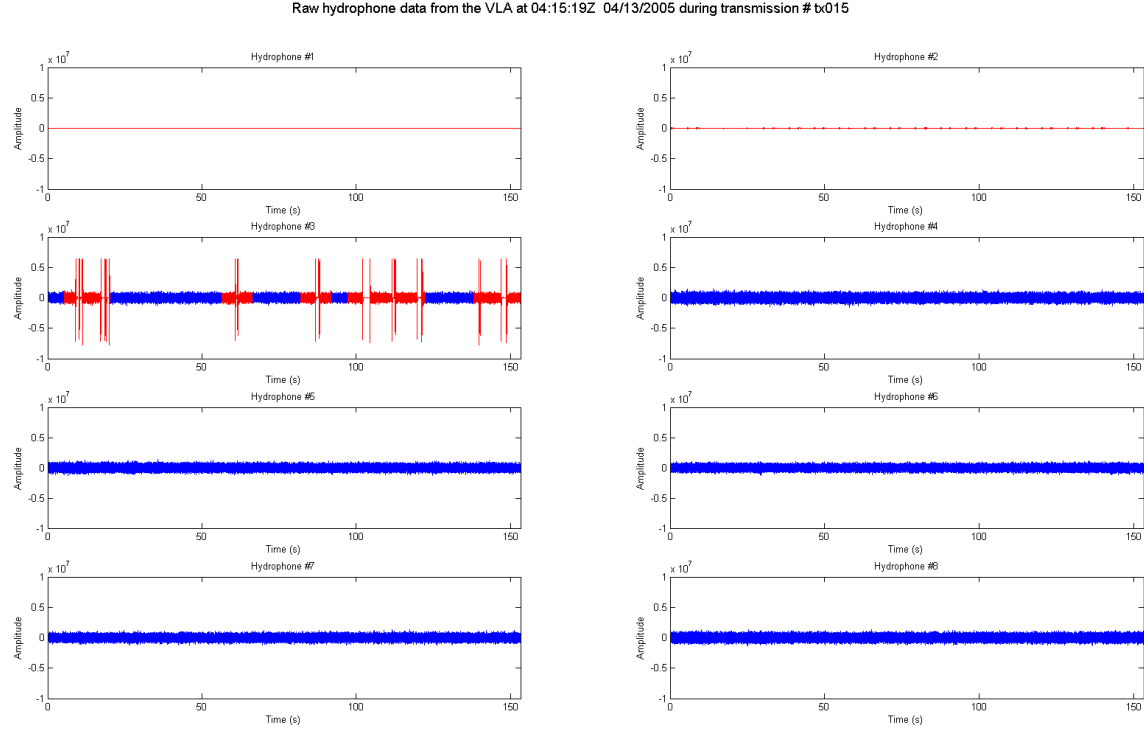
Figure 11.   An example of a raw voltage plot from the eight hydrophones on the VLA. Spikes and shorts that occurred during one of the thirty 5.11-s m-sequence transmissions have been highlighted in red. These voltage segments were removed from the hydrophone data before sound intensity levels were calculated.
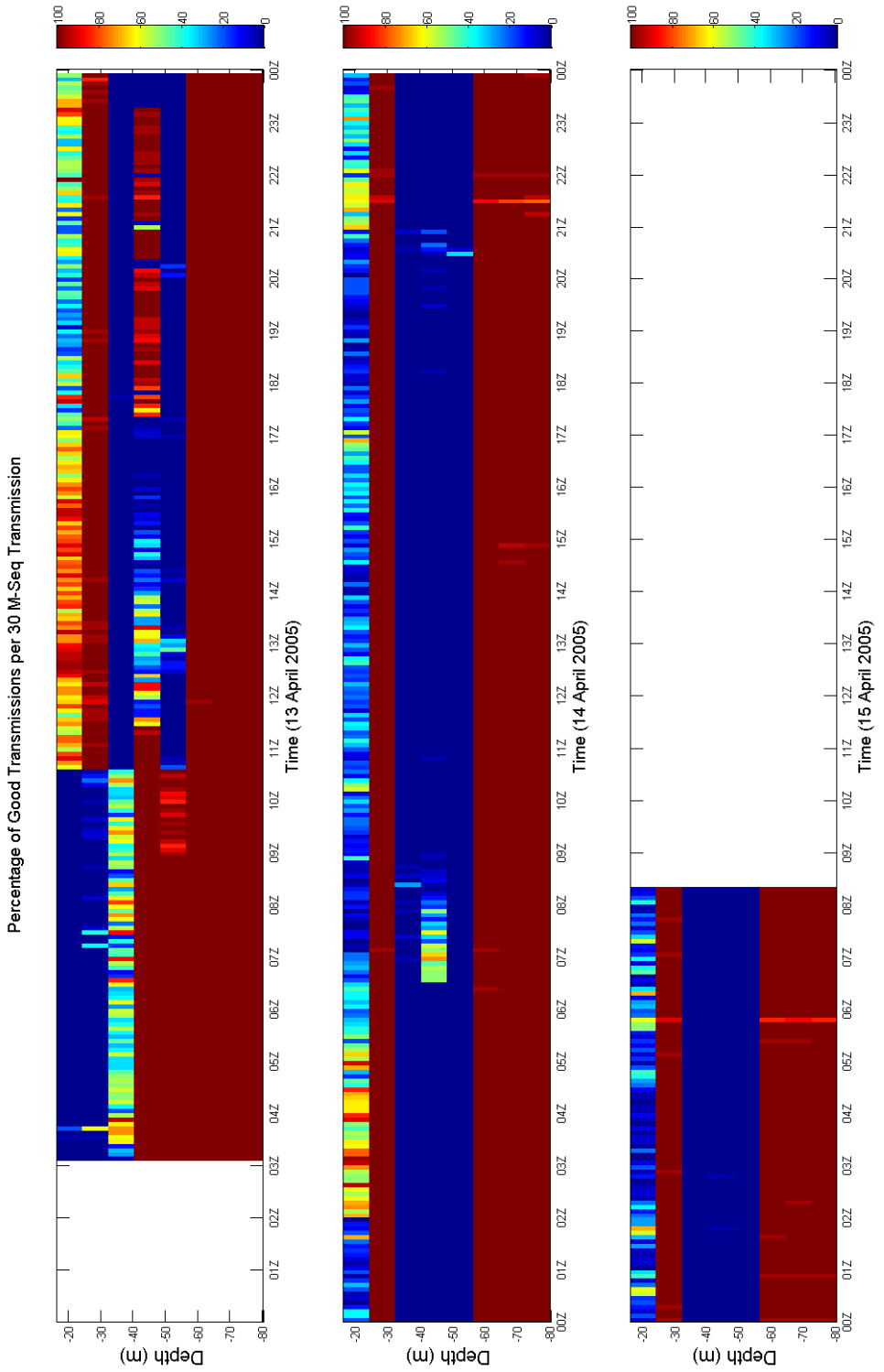
Figure 12.   The percentage of good m-sequence transmissions that were recorded on each of the eight hydrophones. Examination reveals a significant lack of reliable acoustic data in the mid- to upper-portion of the water column.
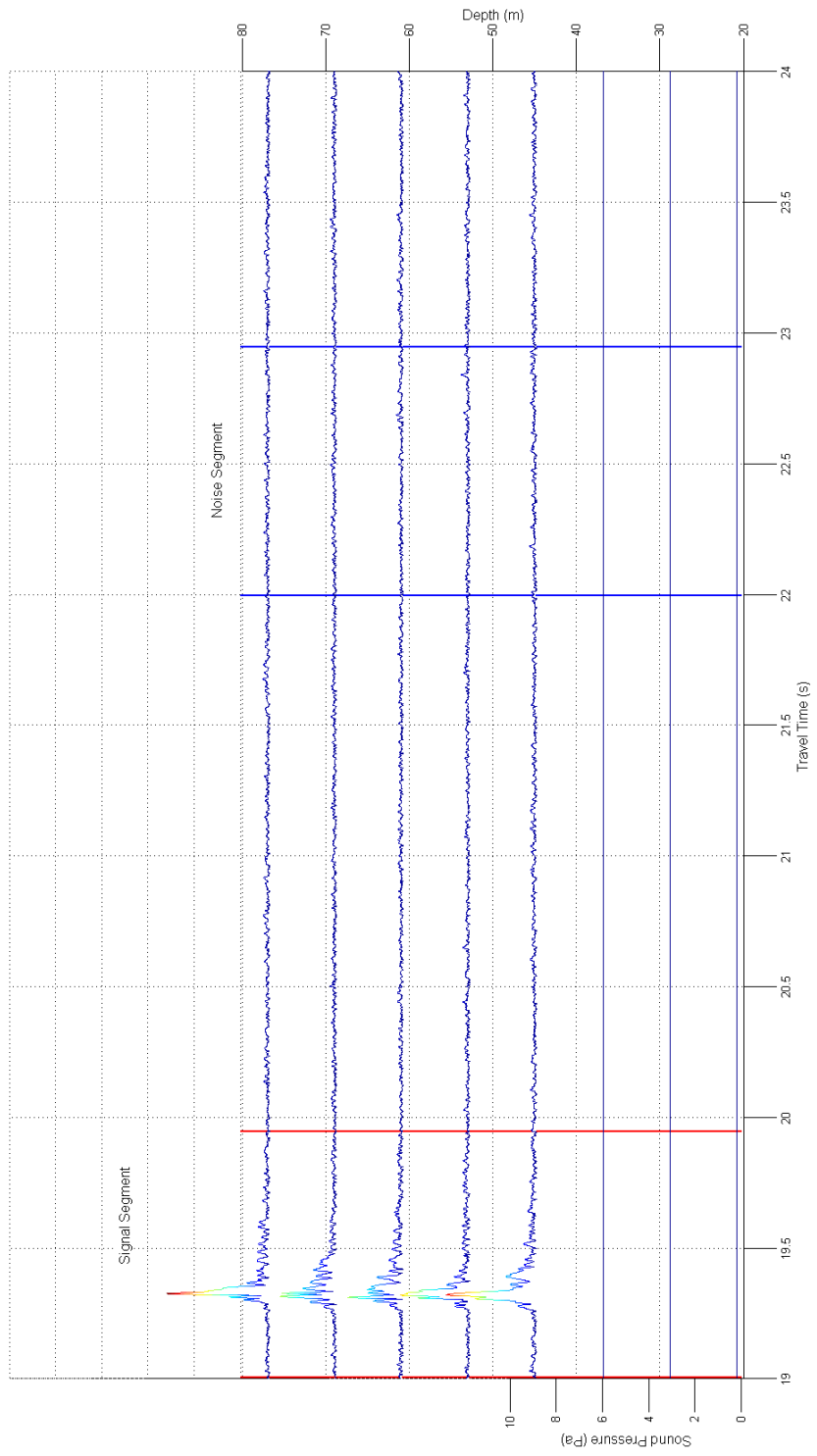
Figure 13.   The third arrival structure as recorded by all eight hydrophones at 04:15 on April 13. The integration window (i.e., T) used to calculate the sound intensity level is outlined in red, whereas a noise segment of equal duration is outlined in blue.

Once the raw hydrophone data were reprocessed, the sound intensity levels of the acoustic transmissions were calculated. First, each of the 30 m-sequence segments was processed using a matched-filter to generate an arrival structure of the compressed pulse (i.e., the pulse response) (Fig. 13). The individual arrivals in the arrival structure correspond to the multipath transmissions of the compressed pulse as a function of time. An example of a measured arrival structure is displayed in Fig. 13. This arrival structure corresponds with the voltage time-series as shown in Fig. 11. Because the voltage recordings on the top three hydrophones were corrupted and removed, there is no associated pulse response with those hydrophones. The multipath spread of the signal segment (i.e., T) (bounded between the red lines in Fig. 13) was 0.95 seconds in length and was consistent throughout the data set.

As previously mentioned in Section II.D, the sound intensity level (SIL) was defined as

$$SIL = 10\log\left(\frac{\frac{1}{T}\int_T p^2(t)\cdot dt}{(1\mu Pa)^2}\right)$$

where T is the multipath spread of the signal (i.e., 0.95 seconds) and p is the pressure of the signal segment in the matched-filter output.

Although pulse-compressing the hydrophone data significantly increased the signal-to-noise ratio, the SIL estimates contain matched-filtered noise, n. Because this noise introduces an error in the SIL estimates, it would be useful to quantify the accuracy of sound intensity level estimates. In a previous study, Chiu et al. (2004) had derived the following equation that relates the standard deviation of the error σ_ε associated with the SIL estimates to the standard deviation of a noise segment, σ_n.

$$\sigma_\varepsilon = \left(\frac{20\log(e)}{\sqrt{f_s}}\right)\cdot\frac{\sigma_n}{\sqrt{\int_T p^2(t)dt}}$$

In the equation above, f_s is the sampling frequency of the signal and σ_n is the standard deviation of a noise segment of the same length as the multipath spread of the signal (i.e.,

36

T). Using Chiu's equation and the noise segment depicted in Fig. 13, the maximum standard deviation of the error in the SIL estimates for three day experiment was less than 0.15 dB. Thus, a high level of confidence can be associated with SIL estimates and the resulting statistical analysis in both Objective 1 and Objective 2 of this dissertation.

The next two Sections will discuss the analysis of both the observed sound intensity levels and its associated statistics during the 24-hour period identified earlier as a series of depression or elevation waves occupied the acoustic path. To aid in this discussion, the measured SIL and its associated standard deviation are presented now. The graph on the left in Fig. 14 is the SIL estimates time-series as measured by the hydrophones, while the graph on the right shows the standard deviation of the measured SIL time-series. Because it was desirable to examine the SIL fluctuations resulting from the high frequency internal wave field rather than the internal tides, the standard deviation of the observed SIL over a 30 minute interval (i.e., the length of the temporal window) was calculated. Also, as mentioned earlier, the EOF fields used to initialize the empirical sound-speed model (which will eventually be used to initialize the acoustic model) do not contain nonlinear internal waves with a period shorter than 10-mintes. Due to this temporal constraint in the empirical sound-speed model, the acoustic model cannot model sound intensity fluctuations resulting from nonlinear internal waves whose temporal scale is less than 10 minutes. Thus, calculating the fluctuations of the SIL using a 30 minute temporal window should facilitate the comparison between the observed variability and the modeled results.

Finally, to prevent erroneous SIL estimates resulting from timing errors where only a portion of the m-sequence was contained in either the first or last 5.11-s segment of the hydrophone data, the first and last m-sequence for each broadcast was discarded. Consequently, only 28 out of the 30 possible SIL estimate "samples" contained in each broadcast were used when generating the statistics of this study.

1.   Vertical Structure of the SIL Time-series

Comparison of the SIL estimates (Fig. 14, second from right) with the sound-speed time-series from the T3 mooring (Fig. 14, second from left) reveals that the long

(i.e., broad) wave pattern correlates extremely well with the SIL estimates. This suggests that the mean vertical distribution of the acoustic energy was driven by the longer spatial scale internal waves (i.e., the broad expansion and compression of the sound-channel) rather than the higher frequency internal waves superimposed on it. Note that when the sound-channel was compressed near the VLA mooring, namely, between 03:00 and 17:00 on April 13, 02:00 and 13:00 on April 14, and finally from 03:00 until 09:00 on April 15, the acoustic energy was primarily confined to the lower layer of the water column. During these periods, the SIL estimates indicate that the energy remains focused near the bottom due to a compacted sound-channel near the VLA until the long-wave pattern expanded the sound-channel allowing acoustic energy to fill the middle portion of the water column once again. A good example of when the sound-channel expanded and acoustic energy was allowed to fill the middle portion of the water column occurred between approximately 19:00 on April 13 and 01:00 on April 14. During this time frame, the sound-channel remained expanded with the thermocline positioned at approximately 40-m near the VLA mooring. The SIL estimates again show a broad period of time when the sound energy was allowed to fill the middle portions of the water column. Similarly, examination of the sound-speed time-series near the VLA prior to 18:00 on April 13, the sound-channel was compacted toward the bottom. Again, the focusing of energy near the bottom can be observed when examining the SIL estimate time-series prior to 16:00 on April 13. It is interesting to note the periodicity of the sound-channel compression near the VLA. Spaced roughly 24-hours apart (i.e., tidal periodicity), the sound-channel is routinely driven toward the bottom in the vicinity of the VLA/T3 mooring sometime between 02:00 and 06:00, where it remains compacted for approximately the next 12 to 14 hours. This cyclical nature of the long-wave pattern is most likely associated with the internal tides. The variability of the measured SIL is discussed next.

2.   SIL Fluctuations Due to Nonlinear Elevation or Depression Waves near the Source or the Receiver

Eight standard deviation maxima in the measured SIL have been identified (Fig. 14, far right). These maxima were observed to occur when either depression or elevation

waves were in the vicinity of the sound source or the hydrophone array. The standard deviation maxima were observed to occur during three episodes.

The first episode of standard deviation maxima occurs when the sound-channel is compacted near the receiver and a series of elevation waves transit across the hydrophone array (identified as events 1, 5, and 6 and on the T3 mooring sound-speed time-series (Fig. 14, second from the left). During all three events, the sound-channel associated with the long-wave pattern is compacted toward the bottom as elevation wave packets transit across the hydrophone array. Note that during this episode, the vertical distribution of the standard deviation is concentrated toward the lower half of the water column. This makes sense if one takes into account the compacted sound-channel associated with the long-wave pattern. As mentioned earlier, when the sound-channel is compacted, most of the acoustic energy will be focused toward the bottom, thus only the lowest acoustic modes would reach the hydrophone array as higher modes would be quickly stripped away by the bottom. Note, however, that the trailing and leading edge of the wave front provides a sharp horizontal sound-speed gradient that could allow acoustic energy trapped in the lowest acoustic modes to scatter into neighboring higher modes. While the elevation wave front may allow for the scattering of sound energy into neighboring acoustic modes, the compressed sound-channel would refract this energy back toward the bottom with a steeper incidence angle, thus quickly stripping this energy away before it was able to reach the hydrophones. This may explain why the measured standard deviation maxima of the SIL occur as the elevation waves are transiting across the hydrophone array (i.e., an extremely localized event).

The second episode occurs when depression waves are near the source (identified as events 2, and 4 on the S mooring sound-speed time-series (Fig. 14, far left)). During both events, the narrow nonlinear depression waves are superimposed on the expanded sound-channel of the long-wave pattern. Note that the vertical distribution of the standard deviation is similar to that observed during the first episode in that it is concentrated toward the lower half of the water column. This result is expected. Unlike the previous episode, the expanded sound-channel associated with the long-wave pattern would allow for the propagation of higher acoustic modes along the transmission path. However, when

39

the depression enters the acoustic path, the sound-channel is compacted near the source thus reducing the number of acoustic modes excited near the source. Consequently, higher acoustic modes would be suppressed along the acoustic path when the depression wave is in close proximity to the sound source. Again, with the acoustic energy limited to the lowest acoustic modes, any scattering (i.e., coupling) of acoustic energy along the acoustic path would be restricted to neighboring low modes. Consequently, because the acoustic energy is focused near the bottom (i.e., low modes), the greatest variability should occur in the lower half of the water column as acoustic energy is scattered out of the lowest modes. This may explain why the measured standard deviation maxima of the SIL are confined to the bottom of the hydrophone array.

The final episode occurs when depression waves are in close proximity to the hydrophone array (identified as events 3, 7 and 8 on the T3 mooring sound-speed time-series (Fig. 14, second from the left). Notice that the vertical distribution of the standard deviation of the measured SIL is much more diffuse vertically. Again, this result is expected if one considers the sound-channel associated with the long-wave pattern. The narrow depression waves from events 3, 7 and 8 are superimposed on an expanded sound-channel. As mentioned earlier, the expanded sound-channel that followed these depression waves would allow for the excitation and propagation of higher acoustic modes. Unlike the previous two episodes where the acoustic energy could only be scattered into higher neighboring acoustic modes, the higher acoustic modes excited and propagating during this episode would allow for the scattering of acoustic energy into both higher and lower acoustic modes. Therefore, as the depression wave moves along the acoustic path, the trailing edge of the wave provides a sharp horizontal sound-speed gradient that could allow for the scattering of acoustic energy into both higher and lower acoustic modes, thus filling the water column with energy. This may explain why the measured standard deviation maxima of the SIL are more vertically diffuse during these events.

It is important to summarize the results from the observed data. First, the long-wave pattern along the acoustic path associated by the expansion/compression of the sound-channel associated with the internal tides appears to drive the mean vertical

structure of the measured SIL time-series. When the long-wave pattern expands the sound-channel, the measured SIL indicates a vertically diffuse acoustic energy field spanning the middle and lower portions of the water column. Conversely, when the sound-channel is compacted toward the bottom, the acoustic energy is more focused near the bottom.

Second, standard deviation maxima of the measured SIL occurred when either nonlinear depression or elevation waves were collocated with the sound source or the hydrophone array. The observed maxima in SIL fluctuations could be separated into three types of episodes. During the first episode, elevation wave packets were observed in the vicinity of the hydrophone array. With a compacted sound-channel, the standard deviation maxima were confined to the lower half of the water column presumably because the scattering of acoustic energy was limited to very low acoustic modes. Additionally, because the sound-channel was compacted toward the bottom, the energy that did scatter into higher modes was mostly likely stripped off after several interactions with the bottom, thus making it an extremely localized event (i.e., only when the elevation wave were in very close proximity to the receiver did scattered acoustic energy reach the hydrophone array). The events in the second episode were characterized by depression waves transiting over the sound source. Again, the variability in the SIL was confined to the lower half of the water column due to the suppression of higher acoustic modes near the sound source. With most of the sound energy initially limited to the lowest acoustic modes, acoustic energy could only be scattered out of the lowest acoustic modes, which consequently resulted in variance maxima observed near the lower half of the hydrophone array. In the final episode, standard deviation maxima occurred as depression waves transited across the hydrophone array. During these events, the expanded sound-channel associated with the internal tides presumably allowed for the excitation and propagation of additional acoustic modes. With a larger number of acoustic modes available to scatter energy, it is possible that the strong horizontal sound-speed gradient found along the trailing edge of these narrow, depression waves allowed for the scattering of acoustic energy into both higher and lower modes, thus scattering acoustic energy throughout the water column.

The next Section will discuss how a spatially and temporally continuous sound-speed field was generated for input into the acoustic model. This discussion will include what assumptions were made as well as limitations of the empirically derived sound-speed model.
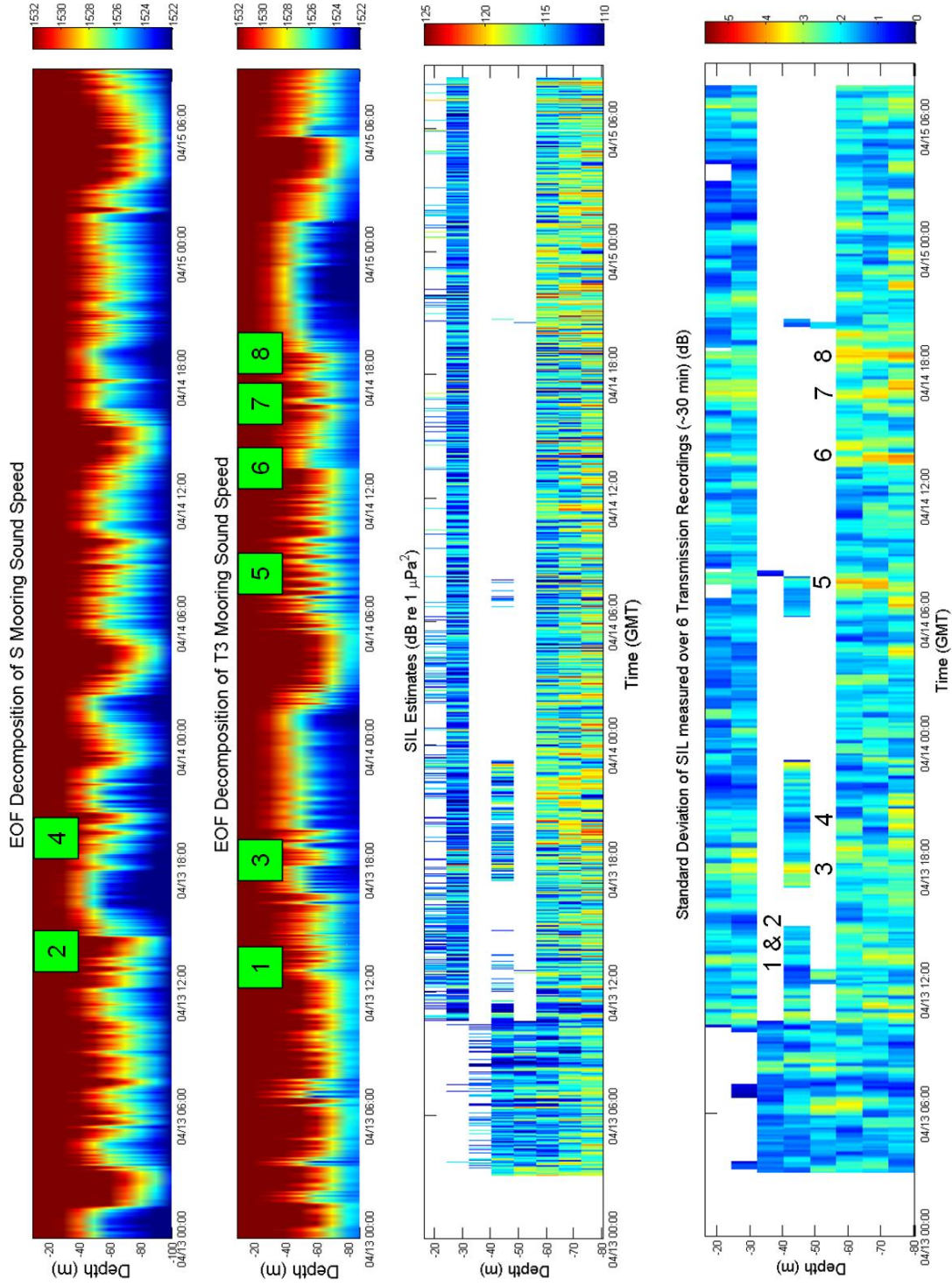
Figure 14.   The reconstructed mode 1 sound-speed time-series for the S mooring (far left) and the T3 mooring (second from left). Additionally, the sound intensity level (dB) time-series (second from right) and the standard deviation of the sound intensity level (dB) time-series as measured over approximately 30 minutes (far right). All are plotted as a function of depth (m) versus time (GMT).

43

D.   MODELING RESULTS

1.   Building a Model to Understand the Phenomenology of the Sound Intensity Field during Nonlinear Internal Wave Events

In order to properly interpret the phenomenology behind the observed sound intensity field and its associated statistics, the use of an acoustic model was required. The acoustic propagation model described by Chiu et al. (1995 and 1996) was used to examine the propagation physics of the sound intensity fluctuations. The basic formulation of the model involves decomposing the acoustic pressure into complex envelopes that modulate (mode by mode) analytic, rapidly varying, adiabatic-mode solutions. Given sound-speed, density, attenuation rate, and bathymetry as a function of space at discrete time increments, the acoustic solution was obtained by integrating a coupled set of differential equations governing the coupled modal envelopes. Model output contained sound pressure, transmission loss, and phase and amplitude of the individual acoustic modes (Chiu et al., 2004).

Chiu's coupled normal-mode model required a sound-speed field that was continuous in both space (range and depth) and time. The method for generating a synthetic sound-speed field for ingest into the acoustic model as outlined by Chiu et al. (2004) was followed. In short, the empirical sound-speed model used in this study was constructed by advancing the principal mode's amplitude time-series measured at the S mooring down-range (based on the time-step and observed wave speed in each of the spectral bands) at discrete time-steps and then reconstructing the sound-speed field using the principal mode interpolated at each range step and the corresponding amplitude value. Additionally, the S mooring sound-speed perturbations, δc_i, calculated with equation 2 were slightly modified in order to account for wave decay and the dispersive nature of the internal waves. This was accomplished using the following relationship:

$$\delta c_i(r,z,t) = \alpha \cdot a_1^{(i)} \left(\beta(t-t_0) - \frac{1}{c_w^{(i)}} \int_{r_0}^{r} \beta \cdot dr \right) \cdot f_1^{(i)}(r,z)$$

and

$$\alpha = \left(\frac{h(r)}{h_0} \right)^{\nu} \quad \text{and} \quad \beta = 1 + \mu \cdot \left(\frac{h(r) - h_0}{h_0} \right)$$

where $f_1^{(i)}(r,z)$ is the principal mode and $a_1^{(i)}$ is the corresponding mode-amplitude time-series for spectral band i, $c_w^{(i)}$ is the apparent internal wave speed along the transmission path and α and β are the wave decay and stretching dispersion parameters, respectively. These are dependent on the ratio of the range-varying bathymetry, $h(r)$, to the water depth, h_0, of the mooring used to initialize the empirical sound-speed model. With known bathymetry and the five environmental moorings' principal mode, $f_1^{(i)}(r,z)$, linearly interpolated along the transmission path and scaled by the local water depths, the model's only free parameters were simply ν and μ, and the internal wave speed along the transmission path for each spectral band, $c_w^{(i)}$. The estimation for the spectral band sound-speed perturbation, δc_i, was complete once these free parameters were tuned to obtain a good match between the model-evolved and the observed principal mode amplitude time-series at each mooring. The final two parameters required by the model were the bottom bathymetry and the acoustic impedance of the bottom.

A high resolution, bathymetric survey was conducted in June 2000 as part of the previous experiment ASIAEX. The results of this survey allowed for the extraction of a high resolution, three dimensional representation of bathymetry contours. A resultant bathymetric transect was constructed for use in the acoustic model as the lower boundary layer.

Lastly, realizing the acoustic path was strongly downward refractive, reasonably accurate measurements of the sediment sound-speed and density were needed for model

initialization. A dedicated, geo-acoustic survey was not conducted during WISE; however, due to its close proximity to ASIAEX, bottom sediment acoustic property estimates from two ASIAEX studies (Marburger, 2004 and Schock, 2004) were used. The bottom layer was assumed to be comprised of a single homogenous layer with a sound-speed of 1700 m/s, a density of 1800 kg/m^3 and an attenuation rate of 0.3 dB/m/kHz.

The empirical sound-speed fields generated and used in the acoustic model were based solely on the first mode. Because the percentage of the temporal variance captured by the principal mode in both spectral bands decreased concurrently with the bottom depth, there was concern that the primary mode (and its associated amplitude time-series) might well represent the sound-speed time-series measured at the deeper moorings, but might not fully capture the variance of the sound-speed measured at the shallower moorings. Additionally, because the decomposed amplitude time-series did not contain nonlinear internal waves with a period shorter than 10 minutes, there was concern that the use of solely the principal mode would not adequately capture the observed fluctuations in the sound-speed field. To help justify the use of the principal mode only, two figures were analyzed. First, the sound-speed time-series using the first mode was reconstructed at 60-m for moorings S, T1, T2 and T3. This time-series was then plotted against the measured sound-speed time-series as recorded by each of the SBE-39s (which were co-located at 60-m) (Fig. 15). The reconstructed sound-speed time-series (blue line in Fig. 15) and the sound-speed measurements (red-dashed line in Fig. 15) show excellent agreement. More importantly, for all mooring ranges, the principal mode time-series appear to capture both lower-frequency oscillations as well as most of the higher-frequency internal waves from the measured data. Additionally, the data from the Acoustic Doppler Current Profiler (ADCP) deployed near the T1 mooring was compared against the vertical sound-speed profile time-series (Figs. 16 and 17). The vertical sound-speed time-series for the T1 mooring has been reconstructed and plotted for April 13 and 14. By measuring the acoustic frequency shift associated with backscatter off of suspended particles, the ADCP can estimate the horizontal and vertical velocities within the ocean. Also, by knowing the estimated sound-speed and timing between the

46

transmitted and received signal, a depth estimate can be associated with the recorded velocity measurements. The vertical velocity measurements from the ADCP have been plotted on top of the sound-speed time-series. Again, for both April 13 (Fig. 16) and April 14 (Fig. 17), the agreement between the in-situ velocity measurements and the principal mode sound-speed time-series is excellent. As depression waves moved thru T1, thus forcing the thermocline toward the bottom, strong downward vertical velocity measurements were observed. Conversely, when elevation waves moved thru, pushing the thermocline toward the surface, strong upward vertical velocity measurements were observed. Also note the strong temporal agreement between the vertical velocity measurements and the sound-speed time-series, especially between 06:00 and 09:00 on April 14 when a series of depression and elevation waves propagated through. Based on the analysis of Figs. 15-17, use of only the low-passed principal mode to construct the 2-D empirical sound-speed field appears justified as the high frequency nonlinear internal waves with periods shorter than 10 minutes do not appear to contribute significantly to the sound-speed variability. The methodology used to determine the spectral wave speed and their associated tuning parameters is discussed next.
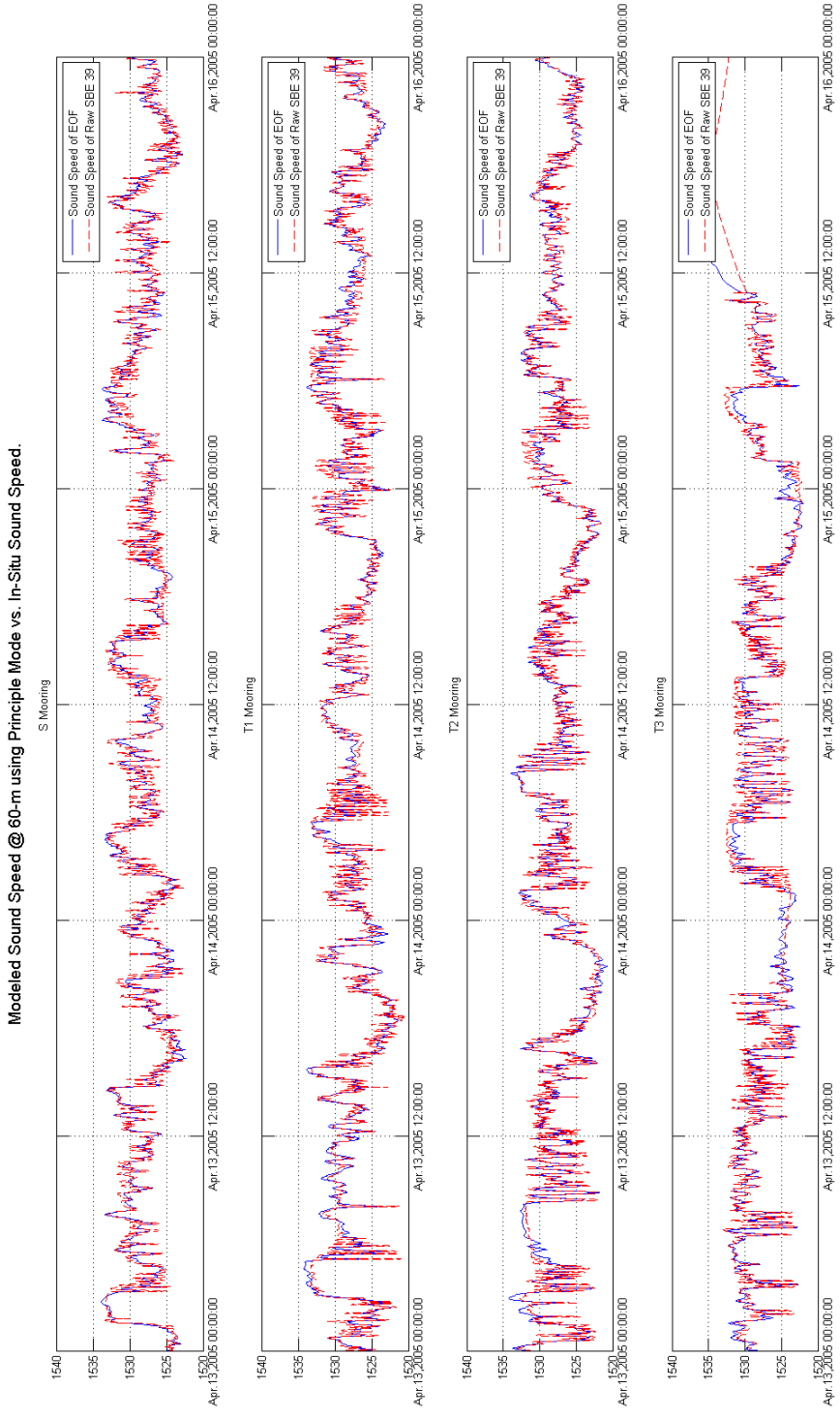
Figure 15.   Comparison between the sound-speed time-series observed by the SBE-39s
(red dashed line) and the EOF mode 1 reconstructed sound-speed time-series at
60-m (blue line) for moorings S, T1, T2, and T3.
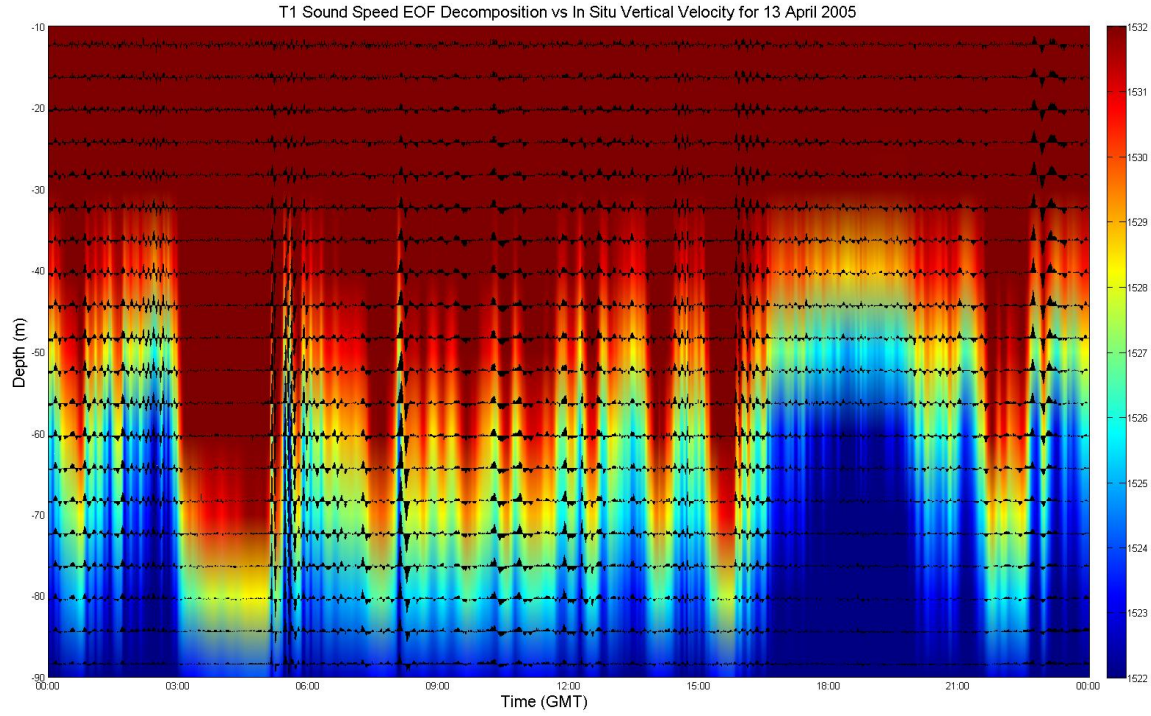
Figure 16. Comparison between vertical velocity measurements (black lines) as recorded by an ADCP co-located with the T1 mooring and the reconstructed mode 1 sound-speed (m/s) time-series for April 13.
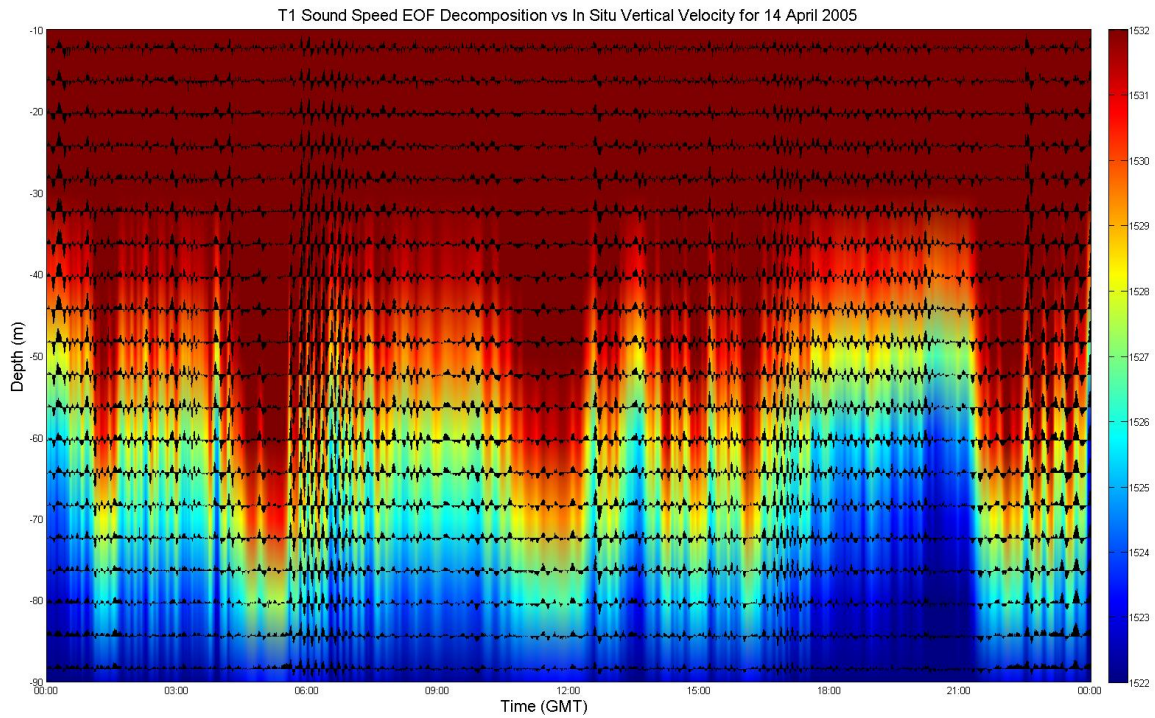
Figure 17. Comparison between vertical velocity measurements (black lines) as recorded by an ADCP co-located with the T1 mooring and the reconstructed mode 1 sound-speed (m/s) time-series for April 14.

Re-plotting the amplitude time-series (Fig. 9) using all three-dimensions (time, principal component amplitude and mooring distance) made the task of tracking wave packets feasible (Figs. 18 and 19). Wave speed was determined by measuring the time it took for distinct peaks (or troughs) to travel along the acoustic path. The wave speeds were estimated to be 0.8 m/s and 1.22 m/s for the super-tidal and tidal bands, respectively. These values were consistent with values determined by Chiu et al. (2004) and Ramp et al. (2004). It should be noted that the wave speeds were not constant due to the nonlinear dispersive effect of the shoaling waves as they interacted with the bottom. This dispersive effect can be seen in Figs. 18 and 19. Note the peaks (or troughs) observed at the deepest moorings, S and T1, are almost perfectly aligned in the vertical. However, as these peaks and troughs travel toward the shallower T2 and T3 moorings, their alignment shifts to the right. This indicates that the waves were slowing as they moved into shallower water. Additionally, as these waves began to shoal, the nonlinear bottom interactions stretched them horizontally. This was especially apparent when examining the peaks and troughs in the tidal band. As the waves transit from mooring S and finally reach mooring T3, they have been severely modified. Tuning of the empirical model is critical to mimic these effects.

With the wave speed established, the only free variables left to determine were the tuning parameters, ν and μ, for each of the spectral bands. These values were determined through a series of iterative comparisons between the empirically propagated amplitude time-series originating from the S mooring and the observed amplitude time-series from each of the five environmental moorings (Figs. 20 and 21). The dispersion parameter, ν, was stepped from 0 (no dispersion) to 4 (strong dispersion) at 0.1 increments, while the wave decay parameter, μ, was stepped from -3 (wave growth) to 3 (wave decay) at 0.1 increments. Optimum values of 3.5 and 0.7 (2.7 and 1.0) were determined for the parameters, ν and μ, for the tidal (super-tidal) band. As mentioned earlier, note that the empirically propagated amplitude time-series does not reach the T3 (or the adjoining VLA) mooring until approximately 10:30 on April 13. This is the temporal model constraint mentioned earlier that prevented the analysis of the first elevation wave train observed in the principal mode sound-speed time-series (white

arrows, Fig. 10). Prior to 10:30, the empirically modeled internal wave field had not reached the hydrophones on the VLA, thus preventing its use in the acoustic model.
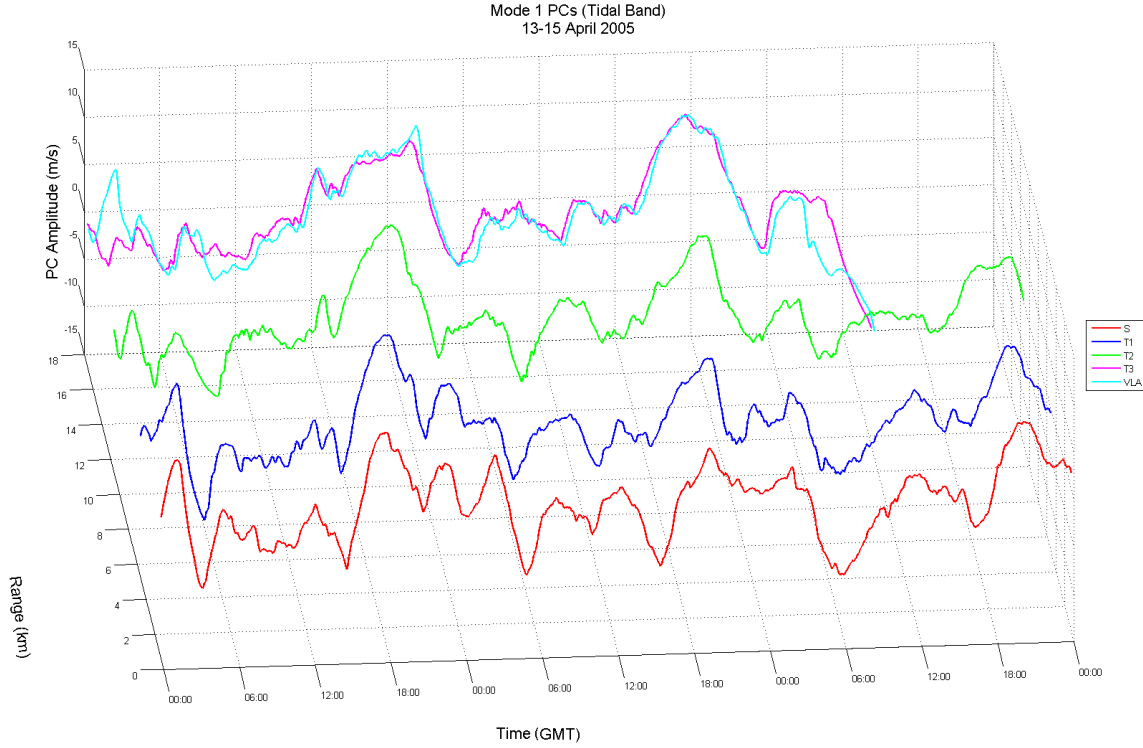
Figure 18.   Rotated view of the tidal band amplitude time-series for the S (red), T1 (blue), T2 (green), T3 (magenta) and VLA (light blue) moorings. Note the nonlinear dispersion and wave-decay as the waves evolve along the acoustic path toward shallower water.
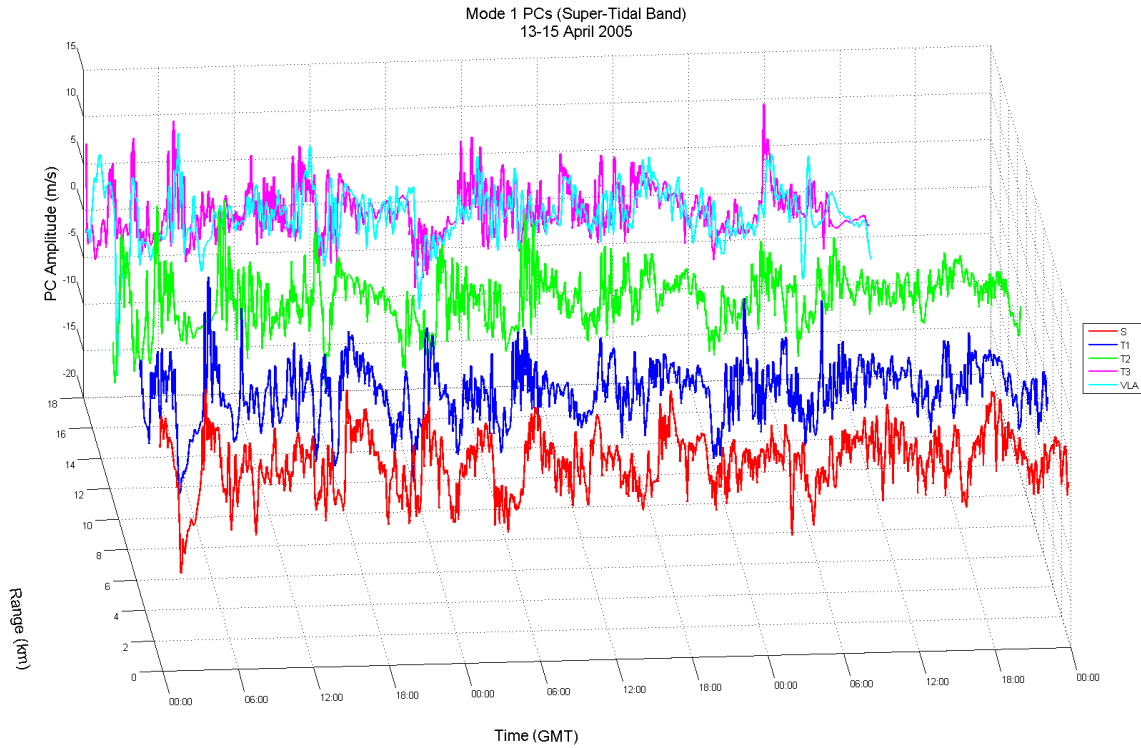
Figure 19.   Rotated view of the super-tidal band amplitude time-series for the S (red), T1 (blue), T2 (green), T3 (magenta) and VLA (light blue) moorings.
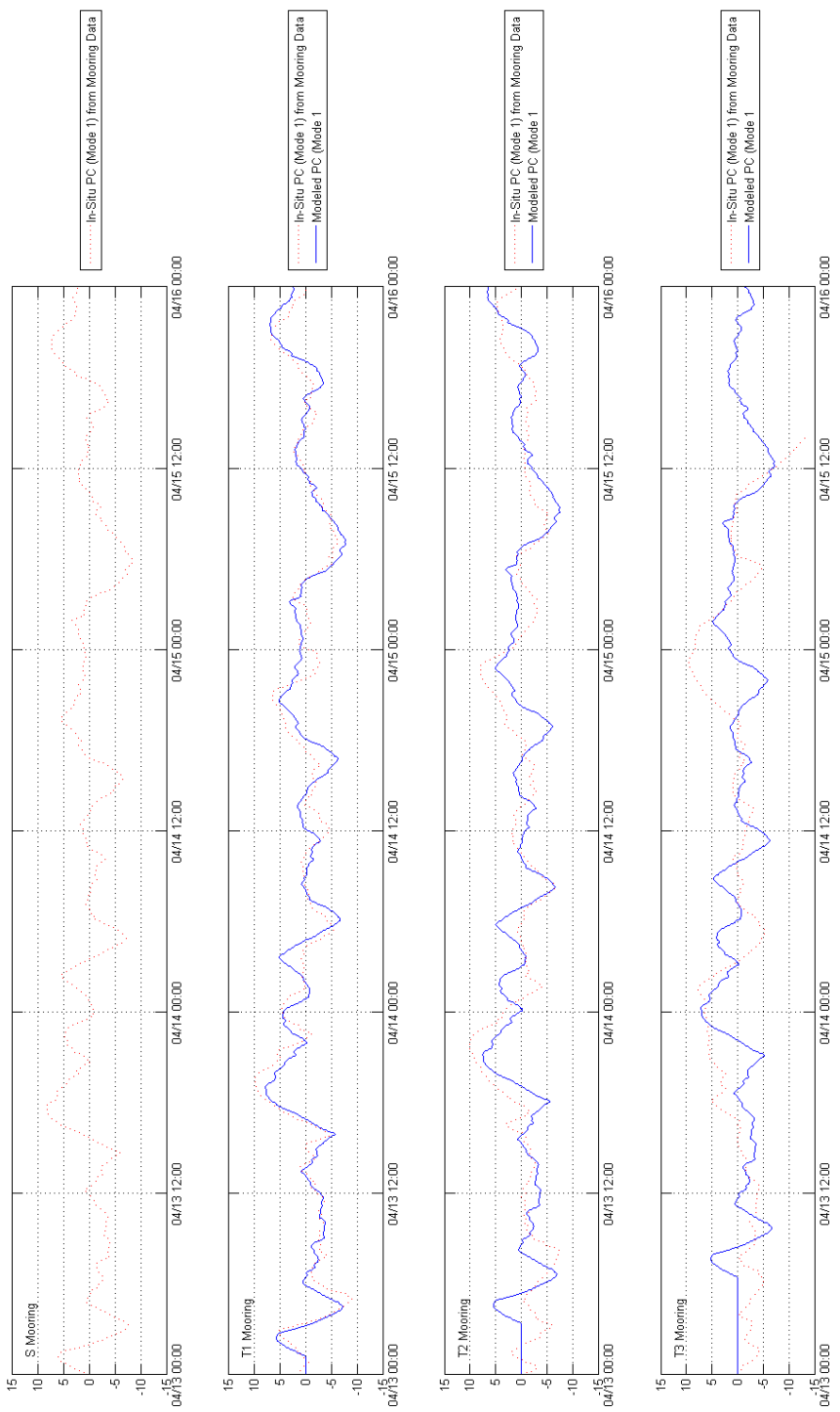
Figure 20.   Comparison between the empirically propagated amplitude time-series from the S mooring (blue) for the tidal band and the observed principal mode amplitude time-series from three of the environmental moorings, T1, T2 and T3, respectively (red dashed line).
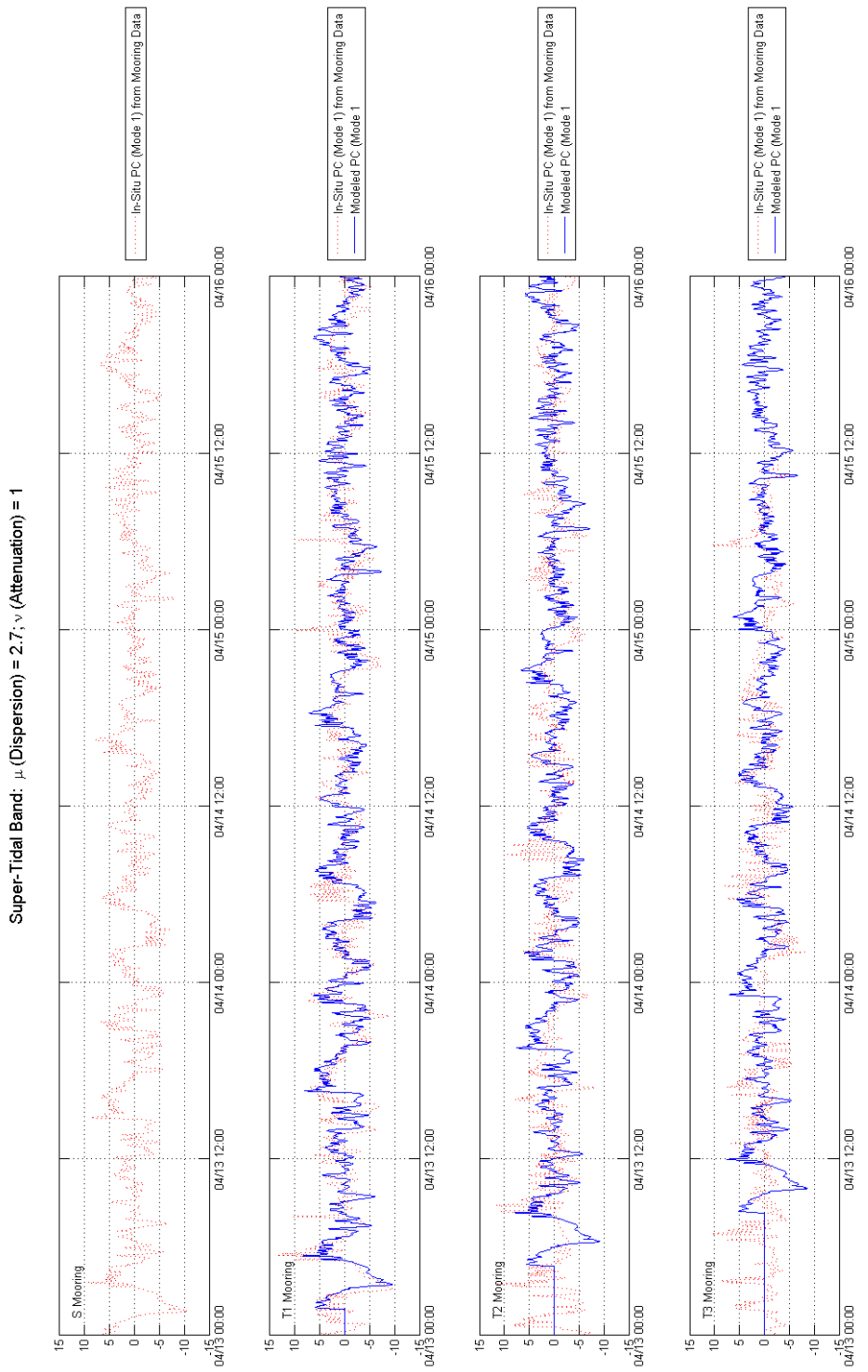
Figure 21.   Comparison between the empirically propagated amplitude time-series from the S mooring (blue) for the super-tidal band and the observed principal mode amplitude time-series from three of the environmental moorings, T1, T2 and T3, respectively (red dashed line).

Analysis of Figs. 20 and 21 reveals that the empirical model does not perfectly match the in-situ data. This result was expected for a few of reasons. First, the empirical model used is somewhat limited in its ability to reproduce not only the complex, nonlinear transformation of shoaling depression waves as they broaden, but also the associated elevation wave packets that form behind the lead depression wave. Second, this model assumes that all the waves that enter the acoustic path originated from the same direction. This assumption facilitates the tracking of wave packets in order to calculate wave speed and any associated wave dispersion. Consequently, it does not take into account waves that enter the acoustic path from multiple directions. Analysis of radar images from the oceanographic vessel, *Ocean Researcher 1*, collected during the three day experiment (not shown) showed the super-tidal wave field observed on the shelf was also comprised of solitons reflecting off of nearby Dongsha Island. Because these reflected waves were propagating in a different direction than the direct path, transbasin waves, they would appear to transit along the environmental moorings at a different speed than their direct path counterparts. Thus, it would be impossible to align these reflected waves with the empirically propagated amplitude time-series. Finally, this model can only propagate wave types (i.e., elevation or depression internal waves) measured by the environmental mooring used for model initialization (i.e., the empirically propagated amplitude time-series). The empirical model can not change the established wave types as they propagate away from the initialization mooring. This limitation is examined more in the next Section. However, even with these limitations, there appeared to be relatively good correlation between the empirically propagated amplitude time-series and the amplitude time-series observed at each of the environmental moorings for both spectral bands. Once properly tuned, the empirical 2-D sound-speed fields had a temporal resolution of 30 seconds and a spatial resolution of 10-m and 0.5-m in the horizontal and vertical, respectively.
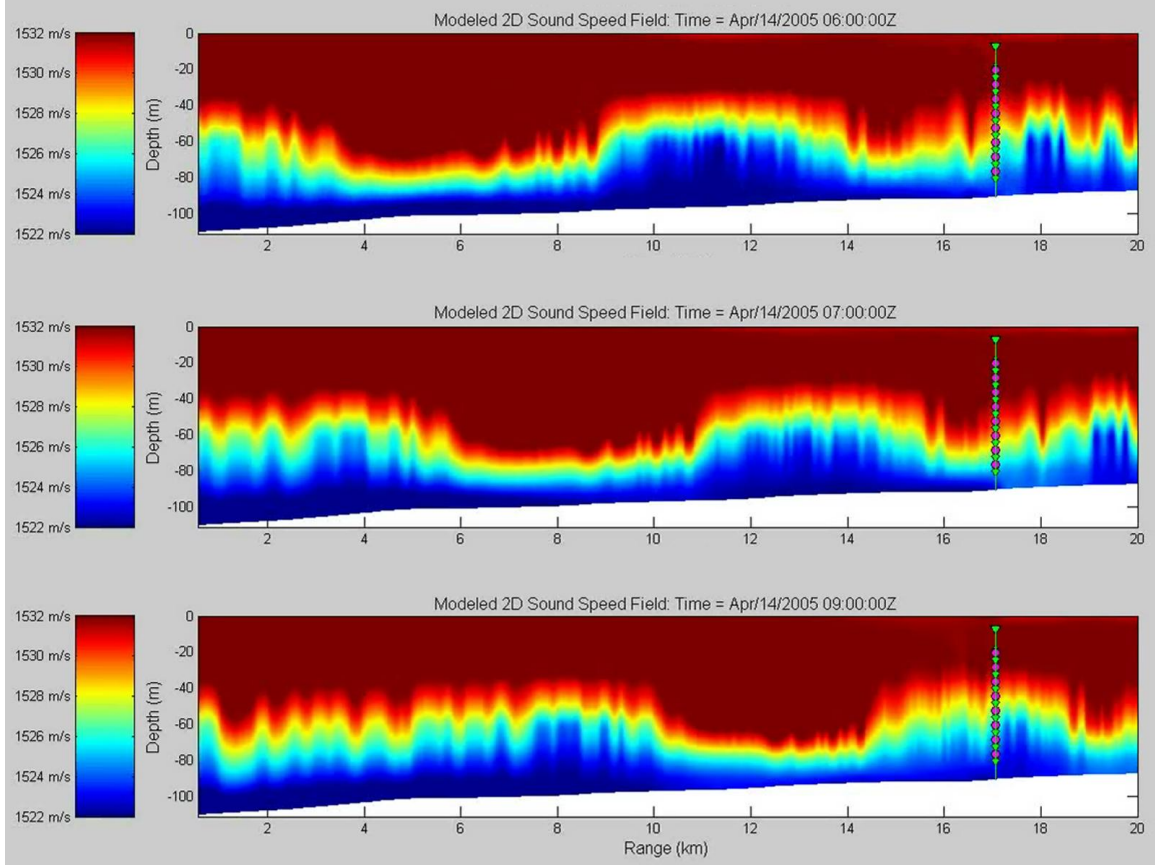
Figure 22.   Three snapshots from the empirically modeled sound-speed field along the acoustic path while elevation waves were observed at the VLA. Note that elevation waves observed at the VLA at 09:00 which resulted from a compacting sound-channel are not present in the modeled sound-speed field. The 400-Hz sound source is positioned at the origin and the VLA is approximately 17-km downrange.

2.   Empirical Sound-speed Model Limitations for Transforming Nonlinear Internal Waves

Figure 22 shows three snapshots of the empirically modeled sound-speed field when elevation waves were known to transit across the hydrophone array. Beginning at 06:00 on April 14 (top figure), the empirical sound-speed model depicts a series of compression and expansions of the sound-channel associated with the long-wave pattern along the transmission path. The broad depression of the sound-channel observed from approximately 3-km to 9-km downrange of the 400-Hz sound source corresponds with the compression of the sound-channel as measured by the S mooring from approximately

04:30 to 05:30 on April 14 (Fig 14). The second compression of the sound-channel in the empirical model was observed from approximately 14-km to 17-km downrange of the sound source. This compression corresponds to the broad depression of the thermocline observed on the S mooring at approximately 00:00 on April 14. Finally, in between the two sound-channel compressions, a broad area with an expanded sound-channel was observed in the empirical sound-speed model from approximately 9-km to 14-km downrange of the sound source.

Referring back to the sound-speed time-series in Fig. 14, if the sound-speed time-series during an elevation wave episode was properly modeled, then the expanded sound-channel observed between 01:00 and 03:00 on the S mooring should compress toward the bottom as it propagates along the acoustic path, during which a series of elevation waves will form in the center of depressed sound-channel. However, comparison between the empirical sound-speed model and the sound-speed time-series measured by the T2 mooring (located approximately 11.5-km downrange), indicates that by 06:00, the upper portion of the empirically modeled sound-channel is too shallow. The measured sound-speed time-series places the upper bounds of the sound-channel at approximately 60-m while the empirical sound-speed model positions it at approximately 40-m. Additionally, as observed in the measured data, while propagating from the T2 mooring to the T3/VLA mooring, the upper portion of the sound-channel should rapidly compress toward the seafloor and a series of well defined elevation waves should appear. Examination of the middle and lower figures in Fig. 22 clearly indicates that the expanded sound-channel never compressed as it propagated toward the VLA. The empirical model failed to reproduce the elevation wave packets observed by the environmental sensors on the VLA/T3 mooring. Re-examination of the empirically propagated amplitude time-series from Fig. 20 revealed why this may have occurred.

Examining Fig. 20, note the two "peaks" observed in the tidal band of the amplitude time-series on the S mooring centered at approximately 22:00 on 13 April and 02:00 on 14 April, which will be referred to the "early" and "late" peak, respectively. These two peaks correspond to two periods when the sound-channel had expanded, forcing the thermocline upward toward the ocean surface. Both of these periods were

observed on the S mooring time-series, positioned on either side of the broad depression wave centered at approximately 00:00 on April 14. As discussed earlier, the empirical model propagated these peaks along the acoustic path based on the wave speed and the selected tuning parameters. As these two peaks were propagated along the acoustic path, they differed from the measured amplitude time-series observed on the downrange mooring in two very significant ways.

First, when the "early" peak reached the T1 mooring (Fig. 20, second figure from the left), it correlates very well with the tidal band amplitude time-series from the T1 mooring; however, when the "late" peak reaches the T1 mooring, it does not correlate well with the measured data. The empirically propagated "late" peak retains its amplitude, thus maintaining the expanding sound-channel, while in reality, the sound-channel had compressed slightly between the two moorings. In-fact, comparison between the model propagated amplitude time-series and the amplitude time-series measured at both the T2 and T3 moorings indicate that the expanded sound-channel associated with the "late" peak was incorrectly maintained and propagated along the entire length of the acoustic path.

The second significant event occurs when the "early" peak propagates from the T1 mooring to the T2 mooring (Fig. 20, middle two figures). While transiting between the two moorings, the "early" peak maintains its convex shape, while the measured data from the T2 mooring shows a trough at approximately 02:00 on April 14. This is significant because the trough observed in the T2 mooring data signifies that the sound-channel is now compacting toward the bottom, rather than maintaining the thermocline near the surface (as indicated by the "early" peak). The trough is also observed to broaden as it propagates downrange to the T3 mooring which explains the broad period (i.e., two to three hours) when the thermocline is depressed toward the bottom as observed in the measured data from the T3 mooring (Fig. 20, far right figure). The empirically propagated "early" peak, however, continues to incorrectly model an expanded sound-channel in the vicinity of the VLA during this time.

This analysis showcases the empirical model's inability to properly model transforming wave types. Because the empirical model was initialized using the wave

types from the S mooring's amplitude time-series, it was unable to reproduce the evolution of the internal wave field into a series of elevation waves as observed in the vicinity of the VLA/T3 mooring. However, if the model was initialized using the amplitude time-series from the T2 mooring, the empirical sound-speed model may have provided a better representation of the sound-speed field as the elevation wave packets transformed along the acoustic path.

With known empirical model limitation, the sound-speed fields were used within the acoustic model in order to generate a modeled SIL time-series. With sound pressure as a model output, modeled sound intensities were compared against the observed sound intensities and are discussed next.

3. Examining Modeled Sound Intensity Levels during Both Elevation and Depression Wave Events

With a known equivalent sound level (SL_e) and range averaging the narrow-band transmission loss TL fields from the acoustic model into the corresponding broadband TL fields associated with a 100-Hz bandwidth signal (Harrison and Harrison, 1995), the modeled sound intensities were calculated and examined (Fig. 23). Note that an abbreviated time-series (i.e., approximately 24-hours) has been presented. This time period corresponds with the previously identified episodes when elevation or depression waves were collocated with either the source or the receiver.

The modeled SIL appears to have captured several key characteristics from the measured SIL. First, as observed in Section III.C, the acoustic model realistically captured the redistribution of acoustic energy throughout the water-column associated with the expansion of the sound-channel at approximately 18:00 on April 13. Additionally, the sound-channel remained expanded until 02:00 on April 14, allowing acoustic energy to fill the middle and lower portion of the water column. During this same time-period, the modeled SIL had also expanded vertically, expanding with the sound-channel. Later, the sound-channel was observed to re-compress toward the bottom between 02:00 and 04:00 on April 14 as a series of elevation waves were observed to form along the acoustic path. Likewise, during this period, the acoustic model focuses the

59

sound energy toward the bottom with minimal energy escaping into the higher modes. In short, the modeled SIL appears reasonably consistent with the observed intensity measurements. The vertical distribution of the modeled sound intensity follows the compression/expansion of the sound-channel which was driven by the long-wave pattern observed along the acoustic path. A comparison between the fluctuations observed in SIL estimates and the standard deviation of the modeled intensity will be discussed next.

Figure 24 depicts the observed standard deviation of the acoustic intensity of the received 100-Hz bandwidth signal using a 30 minute variance window (second from the right) and the variance calculated from the modeled SIL (far right figure). To facilitate this discussion, the corresponding reconstructed mode 1 sound-speed time-series (with the previously identified nonlinear internal wave events) for the S mooring (figure, far left) and the T3 mooring (second from the left) are also presented. Finally, the periods previously identified when the empirical sound-speed model failed to properly replicate the elevation wave packets have been delineated.

When examining the entire record length, the modeled standard deviation appears to correlate reasonably well with the observed variance of the received signal, with two exceptions. First, the variability of the modeled sound intensities when compared against the measured intensity fluctuations during the passage of the elevation wave packets is significantly weaker. As discussed earlier, examination of the empirically modeled sound-speed fields revealed that the elevations waves were not properly modeled.

The second exception is that the overall magnitude of the model variance appears to be slightly less than the variance from the observed sound intensities. This is an expected result for two reasons. First, as mentioned previously, only the principal mode was used in the empirical sound-speed model (i.e., the temporal variability of the sound-speed field resulting from higher empirical modes was not captured). As such, when the mode 1 sound-speed fields were used with the acoustic model, the resulting modeled sound intensity fields would not contain the variability resulting from both the higher empirical modes of the sound-speed perturbation time-series as well as nonlinear internal waves with periods shorter than 10 minutes. Consequently, the modeled standard deviation time-series was expected to be less when compared against the in-situ

measurements. Second, because a more detailed sediment model was not available, the bottom was approximated as a bottom with uniform sediment properties. When comparing the modeled sound intensities to the measured sound intensities (Fig. 23), modeling the bottom as a homogeneous layer appears to be a reasonable approximation; however, when the real bottom was replaced with a homogeneous layer in the acoustic model, variability introduced to the sound intensity measurements by the real bottom was reduced.

However, even with these two exceptions, the spatial and temporal variability of the sound intensities are reasonably well modeled. For example, from 17:00 to 21:00 on April 13, several standard deviation maxima in the measured SIL associated with events 3 and 4 were observed from the hydrophone data. The model captured these events rather well as shown by the standard deviation maxima from 17:00 to 19:00 (Fig. 24, far right). Additionally, when the sound-channel was observed to collapse toward the bottom around 03:00 on April 14 due to the transforming/broadening depression waves resulting in the formation of elevation waves along the acoustic path, a standard deviation maximum was observed in the acoustic intensity measurements. The model captured this event as well with a standard deviation maximum found at approximately 03:00 as well.

Using the results from both the empirical sound-speed model and the acoustic model, the final portion of this Section will conclude with a discussion relating the physical evolution of the measured sound intensity time-series observed during the passage of a depression wave along the acoustic path (i.e., events 2 & 3 identified earlier).
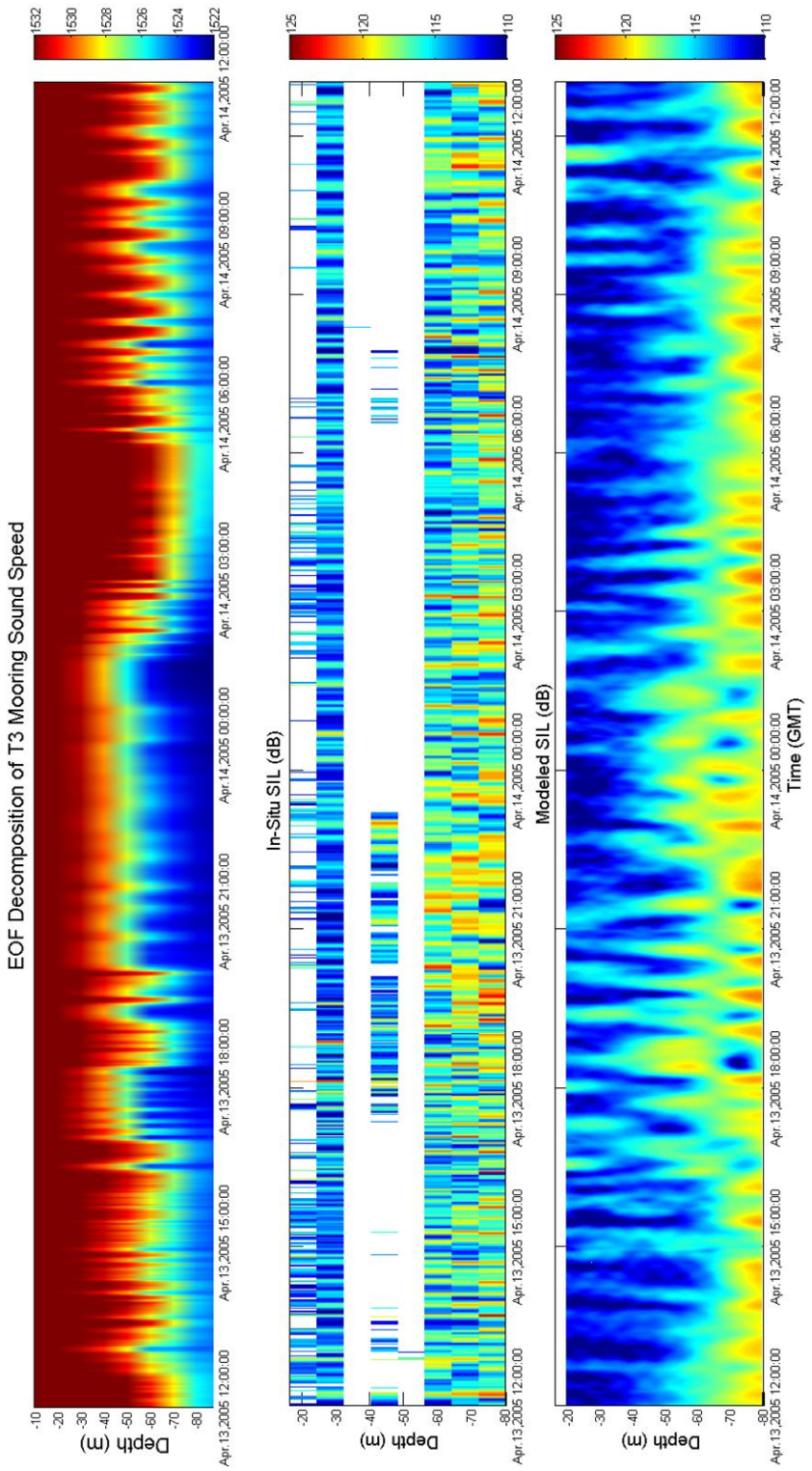
Figure 23. Reconstructed mode 1 sound-speed time-series for the T3 mooring (left). Measured sound intensity (dB) (center) versus modeled sound intensities (dB) (right) from 12:00 April 13, 2005 to 13:00 April 14, 2005.
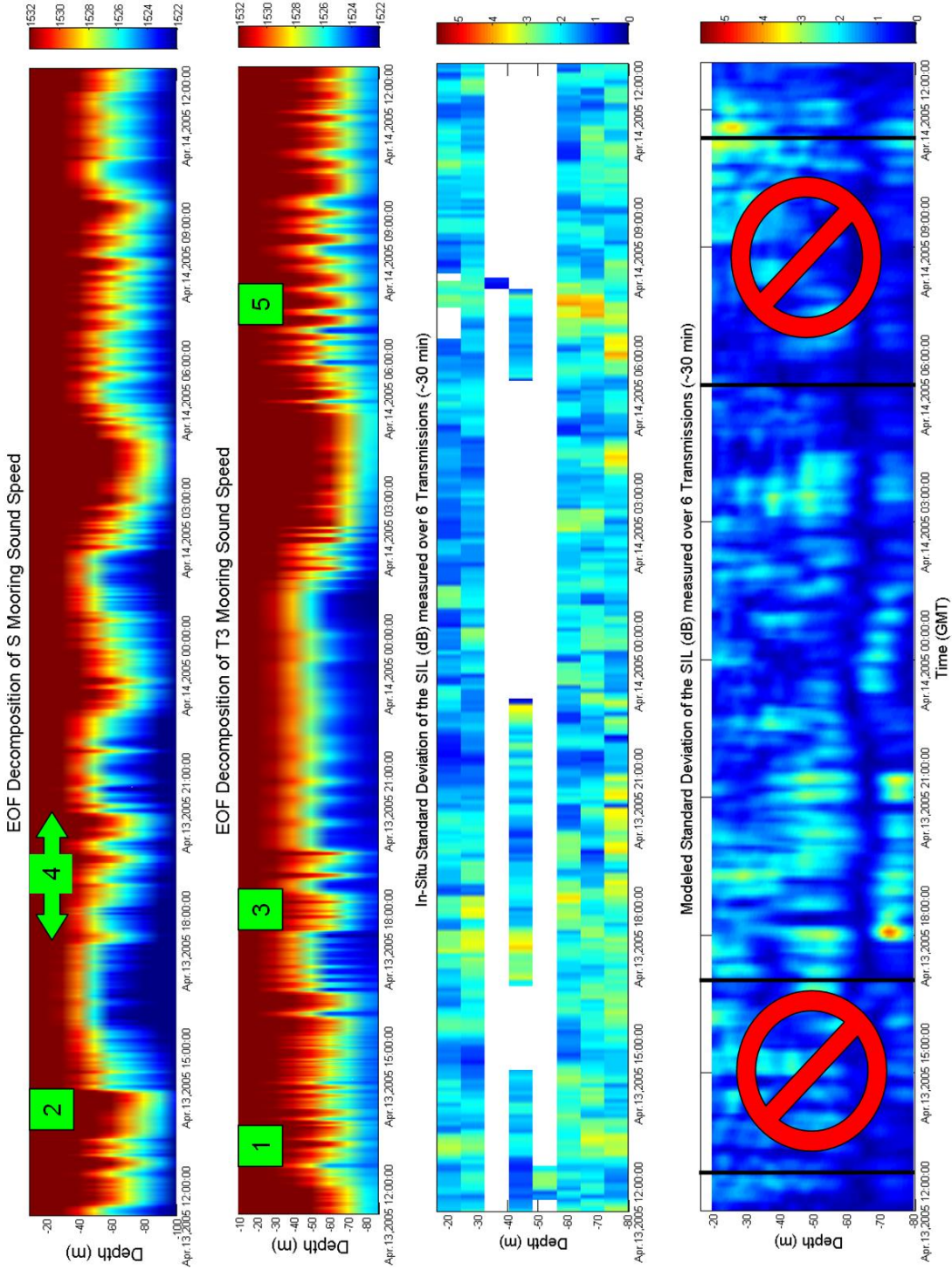
Figure 24.   Reconstructed mode 1 sound-speed time-series for the S mooring (far left) and the T3 mooring (second from left). Additionally, the observed standard deviation of the sound intensity fluctuations (dB) (second from right) is compared against the modeled standard deviation (dB) (far right) using a 30-min window. The two periods delineate when elevation waves were observed near the receiver (which the empirical sound-speed model failed to replicate).

63

4. Examining the Phenomenology When Depression Waves Occupy the Acoustic Path

Figures 25 - 27 show three modeled snapshots from the depression wave case study. Each of the three figures contains the empirically modeled sound-speed field (top), the modeled transmission loss TL (middle) and the relative modal magnitude from the acoustic model (bottom). Figure 25 depicts the broad depression wave from events 2 and 3 shortly after it enters the acoustic path. As previously mentioned, the downrange sound-channel is compacted toward the bottom between the source and the receiver. At this instant, the relative modal magnitude indicates that three groups of modes are initially excited near the sound source. The first group corresponds with the acoustic energy trapped by the predominately downward refracting sound-speed field found in the compacted sound-channel (i.e., low mode group). This mode group propagates from the source at low angles, with minimal interactions with the bottom. The second group of modes that are excited is modes 8 through 16 (i.e., intermediate mode group). These intermediate modes propagate away from the sound source at slightly higher angles. Based on their steeper trajectory and the geometry of the shallow-water experiment, the intermediate modes appear to interact with both the surface and bottom boundaries. Although the relative modal magnitude indicates that some acoustic energy from the intermediate modes is reaching the hydrophone array, it is significantly weaker when compared to the sound intensity contributed by members of the low mode group. The last group of modes (18-25) (i.e., high mode group) corresponds to rays that initially have very steep launch angles. In all three snapshots, these high angle modes are initially excited, but are quickly attenuated (i.e., stripped away) after several interactions with the bottom.

In this first snapshot (Fig. 25), note that the sound-channel is compacted the length of the transmission path. With a compacted sound-channel, the majority of the acoustic energy was focused toward the bottom as can be observed in the transmission loss and relative modal magnitude figures. This agrees with the observed vertical distribution of the sound intensity from Fig. 23 (center). Note that at this time, only the lowest members (1-3) of the low mode group are excited and propagate the length of the

transmission path. Additionally, the intermediate mode group was contributing little (if any) acoustic energy to the measured SIL as it was fairly well stripped out by the bottom before reaching the hydrophones. The acoustic energy from the high mode groups was completely stripped away and did not contribute to the measured SIL. Also note that weak mode coupling is observed along the length of the transmission path. This first snapshot provides some insight into episodes 1 and 2 (i.e., elevation waves near the receiver and depression waves near the source, respectively). As previously inferred, the compression of the sound-channel has suppressed all but the lowest members of the low mode group. With all the acoustic energy confined to the lowest members of the low mode group (i.e., 1-3) the scatter of acoustic energy along the acoustic path is limited to neighboring higher acoustic modes. Thus, as previously concluded, the intensity fluctuations resulting from the scattering of acoustic energy out of the lowest members of the low mode group will be confined to the lower half of the water column.

In Fig. 26, the depression wave is now centered approximately 4-km downrange of the sound source (top). The sound-channel remains compressed for the majority of the transmission path; however, as mentioned early, there is a rapid expansion of the sound-channel behind the depression wave. In this region between the sound source and the trailing edge of the nonlinear depression wave, additional members (1-6) of the low mode groups have been excited. Downrange of the depression wave, the sound-channel remains compacted, thus focusing the acoustic energy toward the bottom of the water column. Both the relative modal magnitude and the transmission loss plot support this conclusion. Note that the sharp horizontal sound-speed gradient formed during the rapid expansion of the sound-channel (i.e., on the trailing edge of the depression wave) is resulting in moderate mode-coupling, which is scattering acoustic energy into both higher and lower acoustic modes. The acoustic energy scattered into the lower members of the low mode group remains focused near the bottom due to the compacted sound-channel, while the acoustic energy scattered into the higher mode is stripped away approximately 11-km downrange, presumably due the increased number of bottom interactions associated with the scattering of acoustic energy into the higher modes. As observed in the previous snapshot, the intermediate and high mode groups are contributing little (if any) acoustic

energy to the SIL. The second snapshot provides some additional insight into the events comprising the first episode (i.e., elevation waves near the hydrophone array). Previously, the standard deviation maxima of the measured SIL were observed to occur when the elevations were in the vicinity of the VLA. It was suspected that any acoustic energy scattered into higher acoustic modes would be quickly stripped out as the compacted sound-channel strongly refracted this energy toward the bottom, thus making the scattering of acoustic energy into higher modes an extremely localized event.

The final snapshot (Fig. 27) captures several of the possible processes (i.e., phenomenology) affecting the vertical distribution of the sound intensity time-series. First, note the broad expanded sound-channel behind the depression wave (top). As can be observed in the transmission loss figure (center) and the relative modal magnitude (bottom), the expansion of the sound-channel has allowed the excitation of additional members (i.e., 1-5) of the low mode group and acoustic energy has spread to fill the middle of the water column from the sound source to the trailing edge of the depression wave. Second, the sound-channel remains compressed for roughly the second half of the transmission path, thus tending to focus the acoustic energy near the bottom. However, strong mode-coupling along the trailing edge of the nonlinear depression wave has scattered acoustic energy from modes 1 thru 5 into acoustic modes 5 thru 7. Unlike the previous snapshot, the energy scattered into the higher acoustic modes is not stripped away by the bottom, but rather has filled the water column between the trailing edge of the depression wave and the VLA with acoustic energy. Additionally, as suspected in the third episode (i.e., depression waves near the receiver), strong mode-coupling is occurring along the trailing edge of the depression wave. Because additional members of the low mode group were initially excited, acoustic energy is scattered into both higher and lower acoustic modes, thus vertically scattering the acoustic energy throughout the water column. The scattering depicted in the modeling results may explain the vertically diffuse standard deviation maxima associated with the events comprising the third episode (i.e., events 3, 7 and 8).

In conclusion, the modeling results are in good agreement with the observed acoustic intensity measurements and help explain its associated phenomenology. First,

the vertical structure of the SIL time-series follows the long-wave pattern observed along the transmission path. When the sound-channel was depressed (Fig. 25), the acoustic energy was focused toward the bottom as higher members of the low mode group were suppressed (i.e., episodes 1 and 2); however, when the sound-channel expanded (Fig. 27), the acoustic energy filled the sound-channel as additional members from the low mode group are excited (episode 3). Second, the rapid relocation of the thermocline (i.e., sound-channel compression or expansion) and its associated sharp, horizontal sound-speed gradient found on the trailing edge of a nonlinear depression/elevation wave was suspected to result in acoustic variability (episodes 1-3). Figs. 26 and 27 clearly show the strong mode coupling that can occur along this interface as energy is scattered into higher modes (episodes 1-3). And finally, even though a rapid relocation of the thermocline may occur, enabling acoustic energy to scatter into higher modes through mode-coupling along the interface, the strong, downward refracting properties that are observed during a compressed sound-channel may strip out the acoustic energy in a relatively short distance from the point of scattering, thus possibly making the associated intensity fluctuations an extremely localized phenomena (episode 1).

5.   Examining the Phenomenology When Elevation Waves Occupy the Acoustic Field near the Receiver

As previously discussed, because it was initialized using the amplitude time-series from the S mooring, the empirical sound-speed model could not properly model the transformation of a broad depression wave into a series of trailing elevation waves; consequently, the acoustic model provided limited insights into the phenomenology of the intensity statistics as related to mode-coupling when elevation waves occupy the acoustic field near the receiver. However, the analysis of the acoustic modeling results in the previous section have provided some insight into the possible phenomenology of the distribution of the acoustic intensity when elevation waves pass by the hydrophone array.
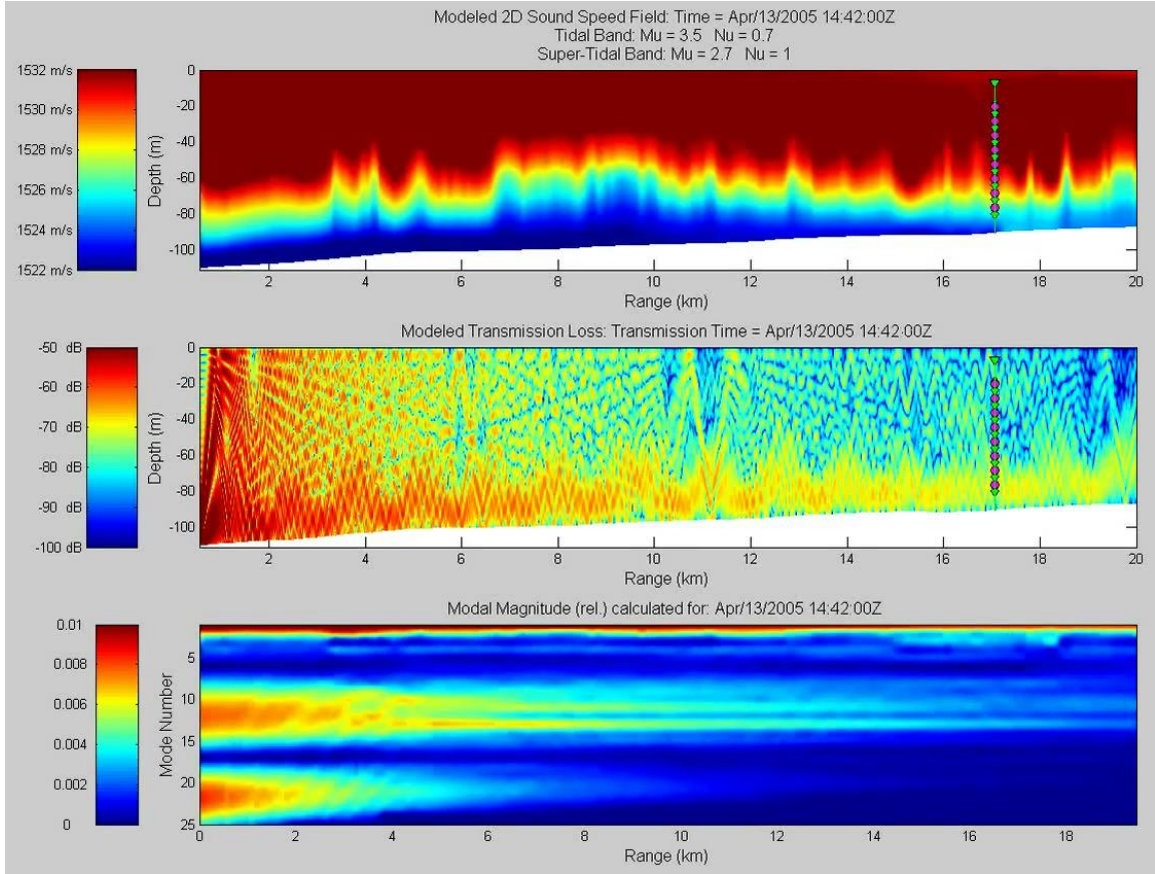
Figure 25.   Combined modeled results from the empirical sound-speed model (top), the modeled transmission loss (middle) and the relative modal magnitude from the acoustic model (bottom) as a depression wave moves along the acoustic path. This first snapshot depicts the center of the depression wave at approximately 2-km with the trailing edge of depression wave located above the sound source (i.e., at the origin) (top figure).
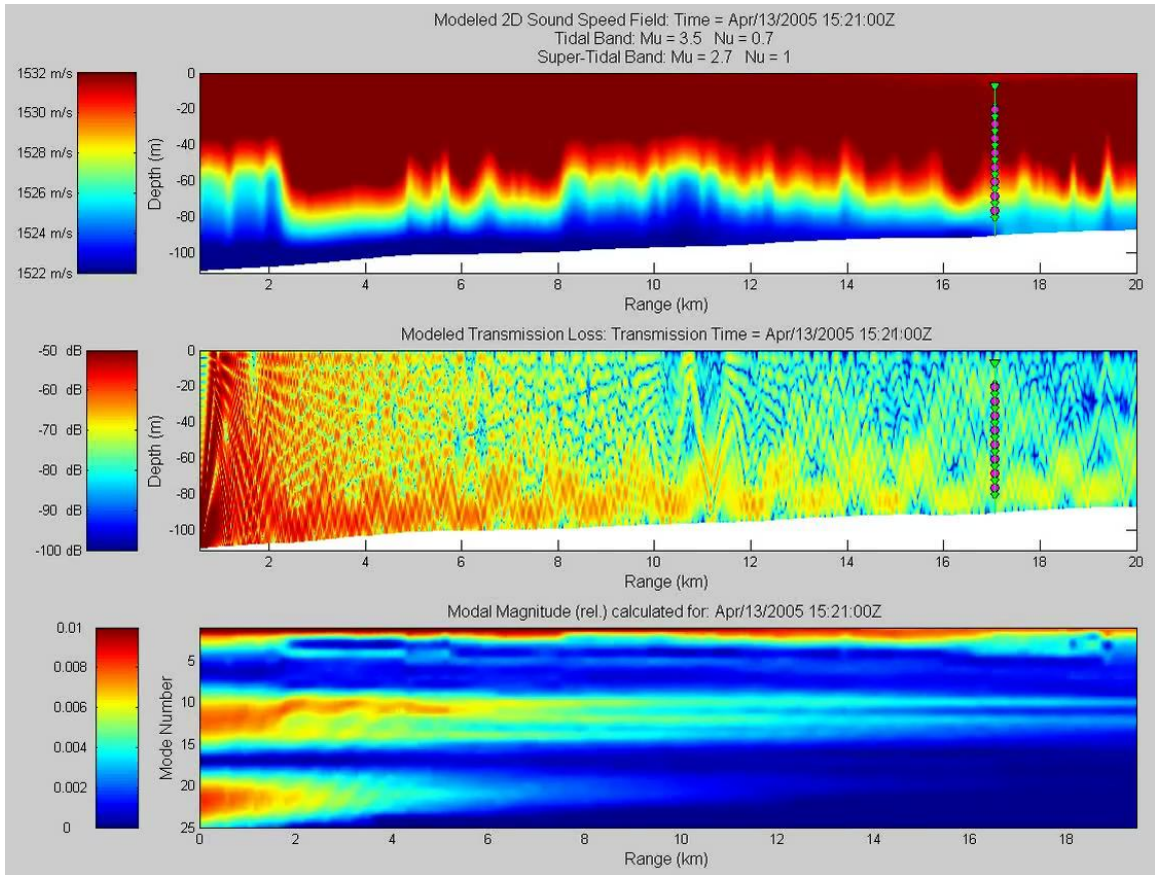
Figure 26.   Combined modeled results from the empirical sound-speed model (top), the modeled transmission loss (middle) and the relative modal magnitude from the acoustic model (bottom) as a depression wave moves along the acoustic path. This second snapshot depicts the depression wave centered approximately 4-km downrange from the acoustic source (top figure).
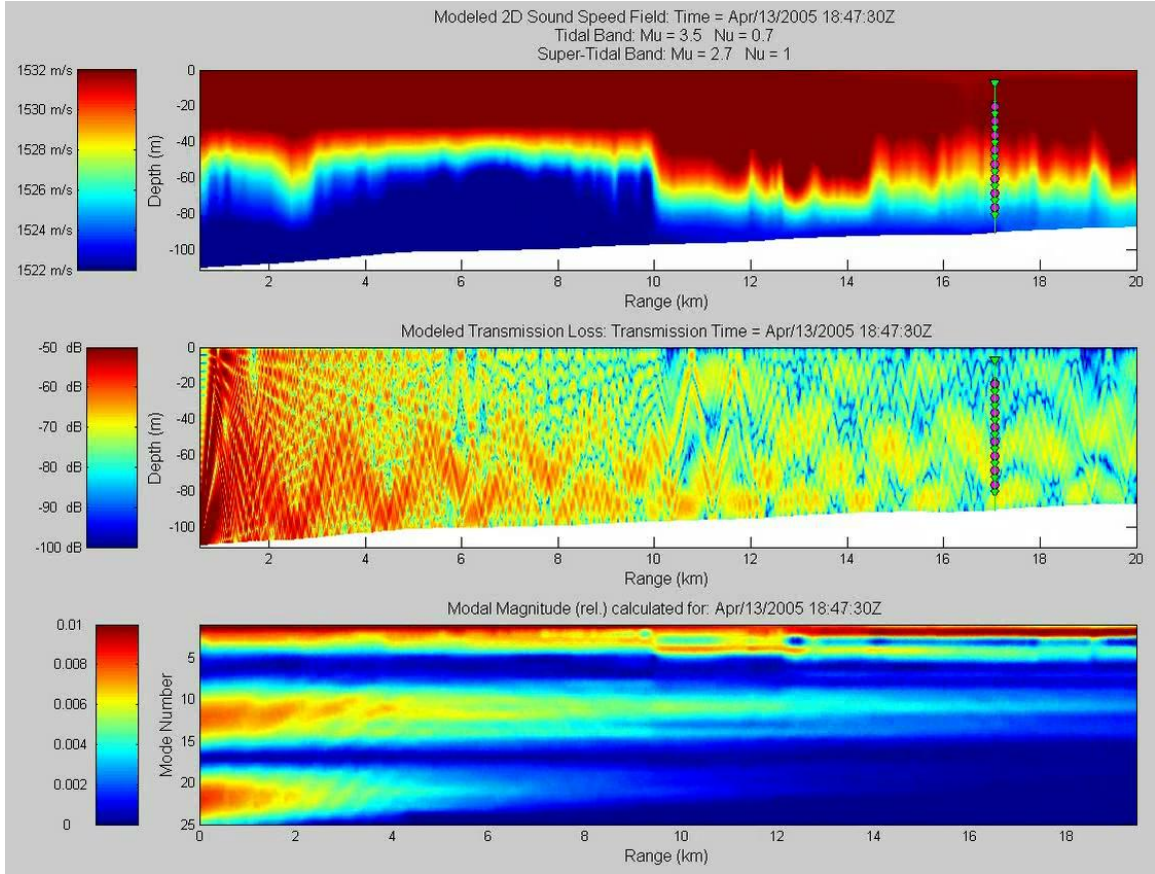
Figure 27.   Combined modeled results from the empirical sound-speed model (top), the modeled transmission loss (middle) and the relative modal magnitude from the acoustic model (bottom) as a depression wave moves along the acoustic path. This third and final snapshot depicts the depression wave centered approximately 11-km downrange from the acoustic source (top figure).

IV.   OBJECTIVE TWO: PROPOSE AND VALIDATE AN EXPANDED STATISTICAL HYPOTHESIS RELATING THE MEASURED VARIANCE TO THE NUMBER OF RESOLVABLE ARRIVALS

In Section I.C. of his paper, Dyer (1970) proposed that the statistics of an ambient noise field could be reasonably predicted if one considered that the acoustic field was generated by multiple distant, spectrally separated acoustic sources. The received multipath signal from each individual noise source, whose phase was uniformly random, would produce mean-square pressure fluctuations that would follow an exponential (i.e., Chi-squared with two degrees of freedom) distribution. As the number of distant "sources" increases, the following will occur. First, for each additional spectrally separated noise source, the degrees of freedom will increase by two. Second, the statistics of the mean-square pressure field from the noise sources will approach a Gaussian distribution as the number of noise sources becomes large. And finally, as the degrees of freedom for the Chi-squared distribution increases, the variance of the noise fluctuations will decrease. In his paper, Dyer presented a set of equations (i.e., his equations 6, 28 and 29) relating the standard deviation of the noise intensity level (dB) to the number of sources, specifically:

$$\sigma_\eta = \frac{10}{\ln(10)} \sqrt{\frac{\pi^2}{6} - S_2(l)}$$

where

$$S_2(1) = 0 \qquad \text{or} \qquad S_2(l) = \sum_{w=1}^{l-1} \frac{1}{w^2}$$

and l is defined as the number of spectrally separated noise sources. This relationship has been plotted in Fig. 28.
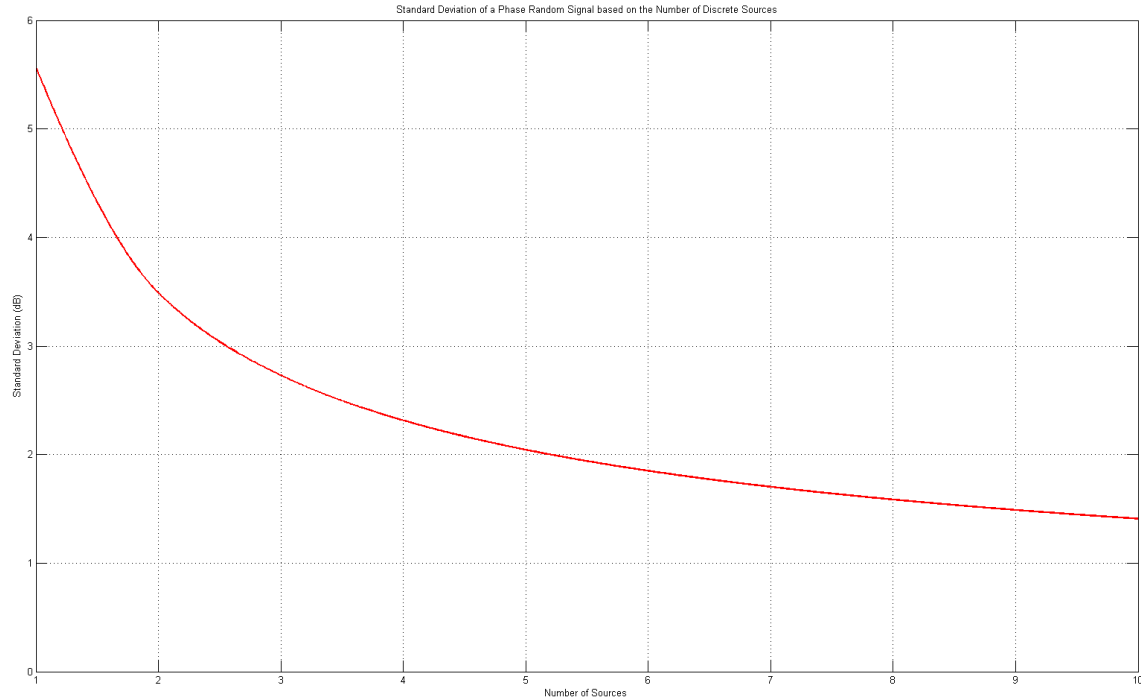
Figure 28.   Expected standard deviation for a phase-random signal based on the number of spectrally separated noise sources (Dyer, 1970).

Realizing that each arrival in any given arrival structure is statistically similar to Dyer's "individual distant noise source," it is hypothesized that the density of the sound intensity fluctuations will follow the log of a Chi-squared distribution where the degrees of freedom are determined by the number of resolvable arrivals (i.e., Fig. 2) thus allowing the prediction of SIL/TL variability based on the number of resolvable arrivals. It is further postulated that as the number of resolvable arrivals increases, the measured variance of the sound intensity distribution will follow the expected changes in the statistical distribution as predicted by Dyer's statistical theory of a noise field (1970). The proposed hypothesis states that the degrees of freedom will be determined by twice the number of resolvable arrivals. Similar to Dyer's theory, as the number of resolvable arrivals increases, the variance of the sound intensity is expected to decrease as the distribution approaches the log of a Gaussian distribution. The relationship between the measured standard deviation of the acoustic intensity and the number of resolvable arrivals as specified in the proposed hypothesis are expected to follow the curve shown in Fig. 28. Furthermore, it is hypothesized that resolvability of the arrivals is sensitive to

72

both the bandwidth of the received signal and the spacing of the multipath travel times. In short, each arrival is hypothesized to represent an independent intensity and the number of resolvable arrivals (i.e., degrees of freedom) drives the statistics. The next Section discusses two acoustic parameters that can affect the resolvability of an arrival.

A.   PARAMETERS INFLUENCING ARRIVAL RESOLVABILITY

1.   Temporal Variability Induced by the Transmission Medium

Incessant, small-scale changes in the sound-speed field along the transmission path due to micro-scale processes result in a continuously changing multipath propagation. Because the transmission path is in a constant state of flux, the travel time (the time it takes for the pulse signal to propagate from an acoustic source to a receiver) is changing as well. Therefore, due to their fluctuating travel time, individual arrivals depicted on an arrival structure will oscillate about a "mean travel time." Two adjacent arrivals may be well separated and show up as two distinct independent pulses on an arrival structure. However, if adjacent arrivals experience a large enough variation in their travel time and are spaced within a close proximity to one another, then there may be times when the adjacent arrivals overlap one another. This overlap will lower the number of resolvable arrivals, reduce the degrees of freedom and alter the statistics.

2.   Bandwidth Sensitivity

An additional parameter that will influence the resolvability of an individual arrival is its pulse-width (which is inversely proportional to the bandwidth of the received signal). If the pulse-width (i.e., the temporal resolution of the pulse signal) is allowed to increase, broad individual adjacent arrivals will have a greater tendency to overlap and will be more difficult to resolve than narrower ones. This would also reduce the degrees of freedom and alter the statistics. Therefore, this suggests that the statistics of the sound intensity fluctuations, which is hypothesized to depend upon the number of resolvable arrivals (i.e., degrees of freedom), is sensitive to both the degree of the travel time

fluctuations and the pulse-width of the arrival. Both modeled and in-situ measurements were analyzed for bandwidth sensitivity and are discussed next.

B.   STATISTICAL ANALYSIS OF THE MODELED INTENSITY

The modeled transmission loss was based on a continuous wave signal and would first need to be transformed into the corresponding transmission loss fields associated with a broadband source. Given the fractional bandwidth of the known (or desired) broadband signal, and the distance separating the source and receiver, the model output was transformed into a broadband signal using a range averaging technique outlined by Harrison and Harrison (1995). Consequently, transmission loss fields for a modeled 10-, 25-, 50-, 75-, 100-, 200- and 400-Hz bandwidth signal were calculated (not shown). Once the TL fields for the seven modeled broadband sources were calculated, the intensity fluctuations from the modeled transmission loss fields were analyzed (Figs. 29 and 30).

1.   Sensitivity of the Statistics to the Bandwidth of the Modeled Pulse

Figure 29 depicts the modeled standard deviation calculated over a 30 minute window for the seven modeled broadband signals. The statistical results from the 10-Hz bandwidth signal are presented in the upper graph followed by the results from the modeled 25-, 50-, 75-, 100-, 200- and 400-Hz bandwidth signal respectively. By examining this figure, two important observations can be made. First, note the inverse relationship between bandwidth of the received signal and the magnitude of the standard deviation of the modeled signal. Specifically, the magnitude of the standard deviation decreases as the bandwidth increases. Even when the variance window was extended to 180 minutes, this relationship still exists (Fig. 30). This model result is in compete agreement with the proposed hypothesis. Second, the standard deviation values are non-stationary (i.e., time dependent). By choosing such a temporally short variance window, the intensity fluctuations depicted in Fig. 29 are known to be associated with the high frequency internal wave field as discussed in Section III. Even when the variance window is extended to 180 minutes, the standard deviation values continue to be time variant, suggesting that these values are still being influenced by the time-varying, high frequency

74

internal wave field. Discussed in detail in the next Section, this finding will be an important consideration when attempting to estimate the degrees of freedom associated with the measured data.
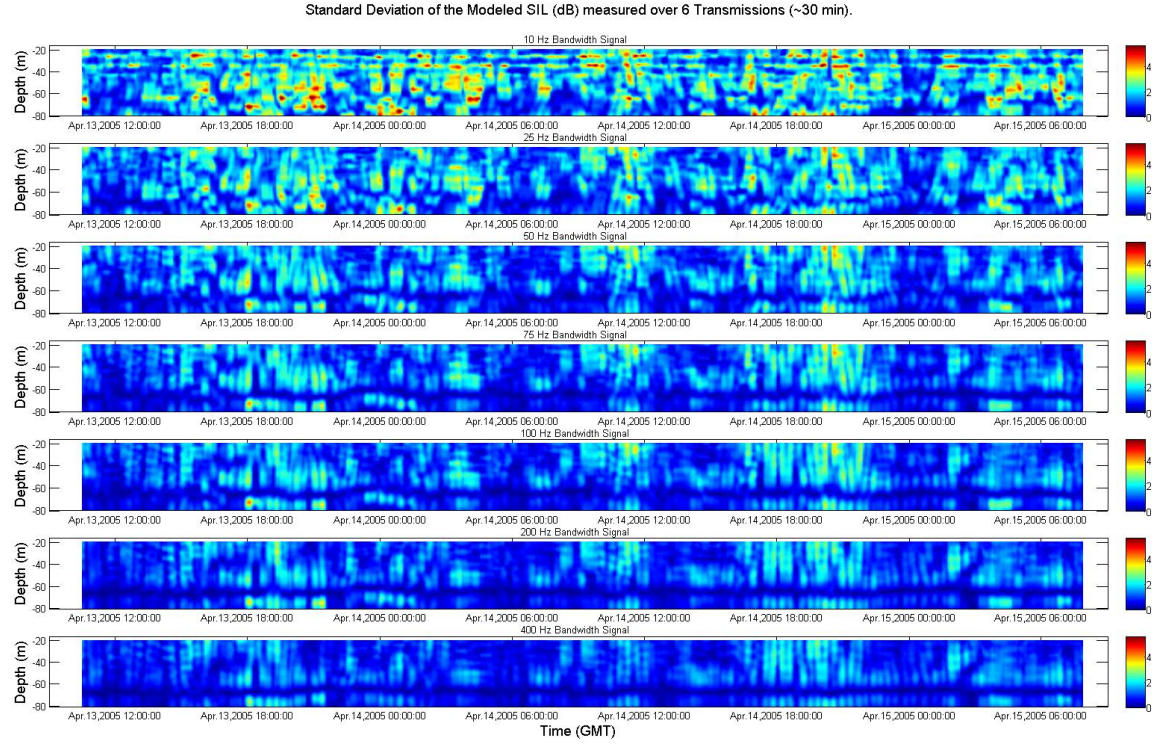
Figure 29.   The standard deviation of the modeled sound intensity (dB) associated with a 10-, 25-, 50-, 75-, 100-, 200- and 400-Hz bandwidth signal. The standard deviation was calculated from the modeled broadband TL using a 30 minute window.
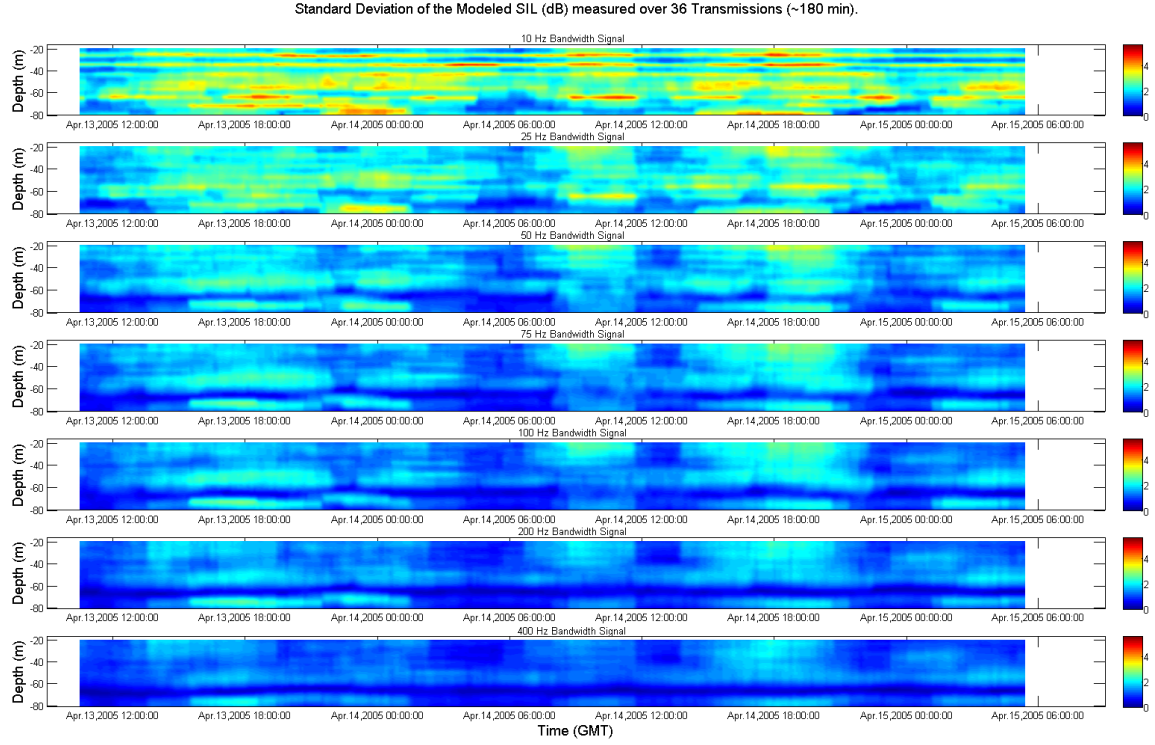
Figure 30.   The standard deviation of the modeled sound intensity (dB) associated with a 10-, 25-, 50-, 75-, 100-, 200- and 400-Hz bandwidth signal. The standard deviation was calculated from the modeled broadband TL using a 180 minute window.

C.   STATISTICAL ANALYSIS OF THE MEASURED INTENSITY

The 100-Hz bandwidth signal collected on the VLA was bandpass filtered in order to generate a 10-, 25-, 50-, and 75-Hz bandwidth signal, thus providing acoustic intensity measurements from five broadband sources. When the bandwidth of the original broadband signal was narrowed through the use of a butterworth bandpass filter, the pulse-width of the recorded signal was increased. This effect can be easily observed when the resulting arrival structures from the bandpass filtered signal are plotted (Fig. 31). The intensity statistics of these five broadband signals will be discussed next.

1. Sensitivity of the Statistics to the Bandwidth of the Received Pulse

The effect of decreasing the bandwidth of the received signal to the temporal resolution of the arrival (i.e., pulse-width) is apparent in Fig. 31. Narrowing the bandwidth of the received signal will result in fewer individual arrivals. For example, note the two separated arrivals located at approximately 19.36-s and 19.38-s associated with the 50-, 75- and 100-Hz bandwidth signal. When the 100-Hz bandwidth signal was filtered to produce a 25-Hz bandwidth signal, the two arrivals broadened and merged into a single arrival. Furthermore, when the signal was ultimately filtered to a 10-Hz bandwidth signal, the once identifiable individual arrivals across the 25-, 50-, 75- and 100-Hz arrival structures have been lumped together into a single broad arrival. Thus, the direct relationship between the number of arrivals and the bandwidth of the received signal is once again observed and in strong agreement with the proposed hypothesis. In order to facilitate a direct comparison with the statistics of the modeled acoustic intensities, the standard deviation of the received signals from the five broadband sources was calculated using a 30 minute and 180 minute variance window and is discussed next.
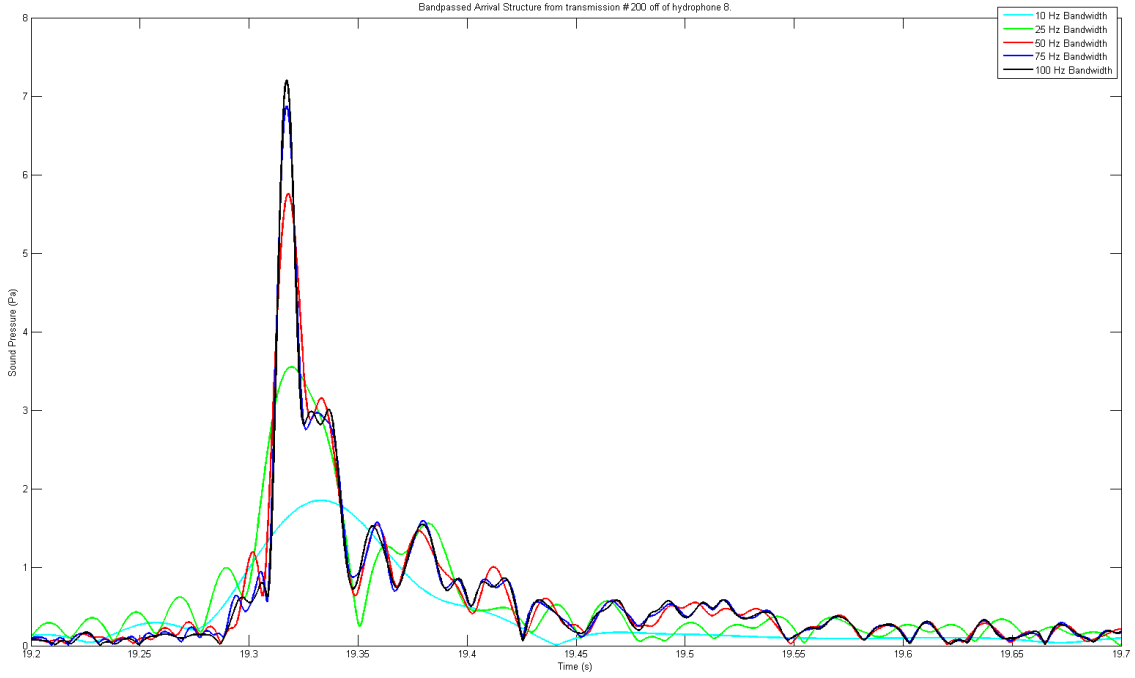
Figure 31.　　Starting with the 100-Hz bandwidth arrival structure (black), the broadband signal was bandpass filtered to derive the arrival structures for a 10-Hz (light blue), 25-Hz (green), 50-Hz (red), and 75-Hz (blue) bandwidth signal.

Examination of both Fig. 32 and Fig. 33 reveals that the measured standard deviation of the sound intensity exhibits a bandwidth sensitivity similar to that depicted in the model results from the previous Section. Namely, the magnitude of the standard deviation decreases as the bandwidth of the broadband signal increases regardless of the variance window used. Also consistent with the statistical analysis of the modeled intensity, Figs. 32 and 33 suggest that the statistics of the measured intensity are time-variant and are being driven by the high frequency, internal wave field. Additionally, there appears to be a tidal-scale periodicity associated with the standard deviation maxima, suggesting that the high-frequency internal wave field is periodic. Two standard deviation maxima were observed 24-hours apart at approximately 18:00 on both April 13 and April 14. It is interesting to note that during ASIAEX, transbasin solitons were observed to reach the 120-m bathymetric curve around 16:00 each day. Considering the close proximity of the shallow-water component of WISE to the ASIAEX site, the

78

standard deviation maxima observed at 18:00 on both days may be the result of shoaling solitons, propagating along the acoustic path.
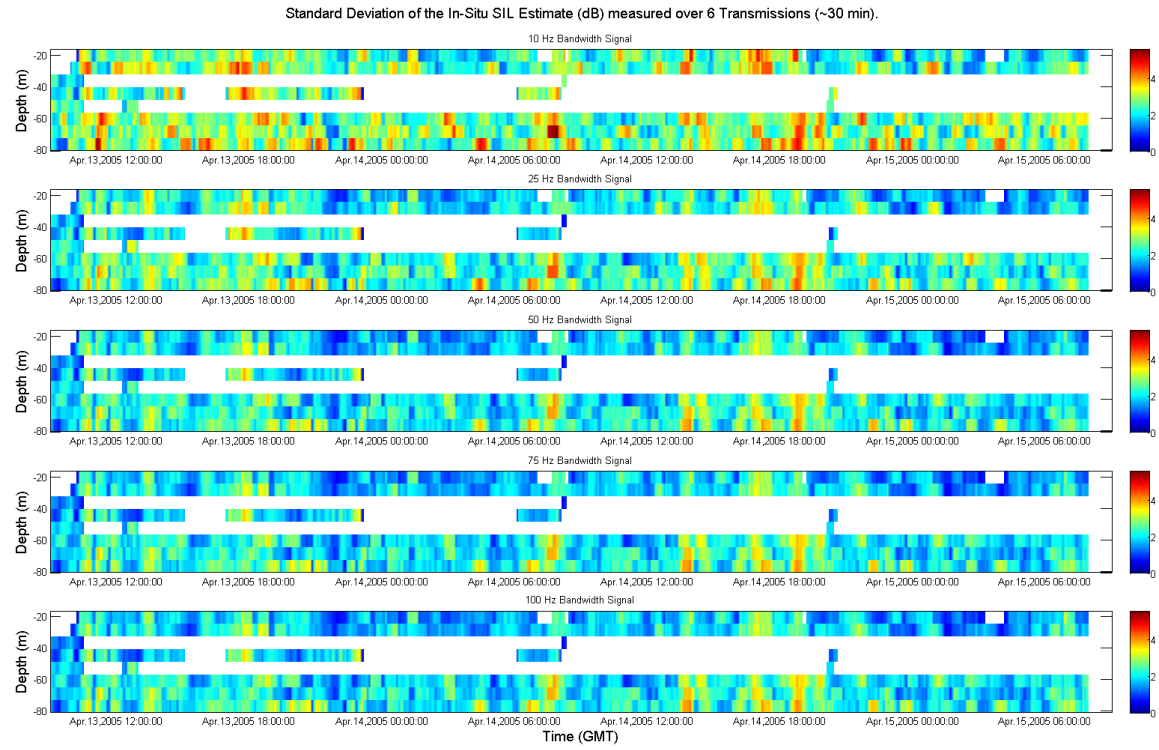
Figure 32.   The standard deviation of the measured sound intensity (dB) associated with the bandpass filtered 10-, 25-, 50-, and 75-Hz bandwidth signal as well as the original 100-Hz bandwidth signal. The standard deviation was calculated from the measured intensities using a 30 minute window.
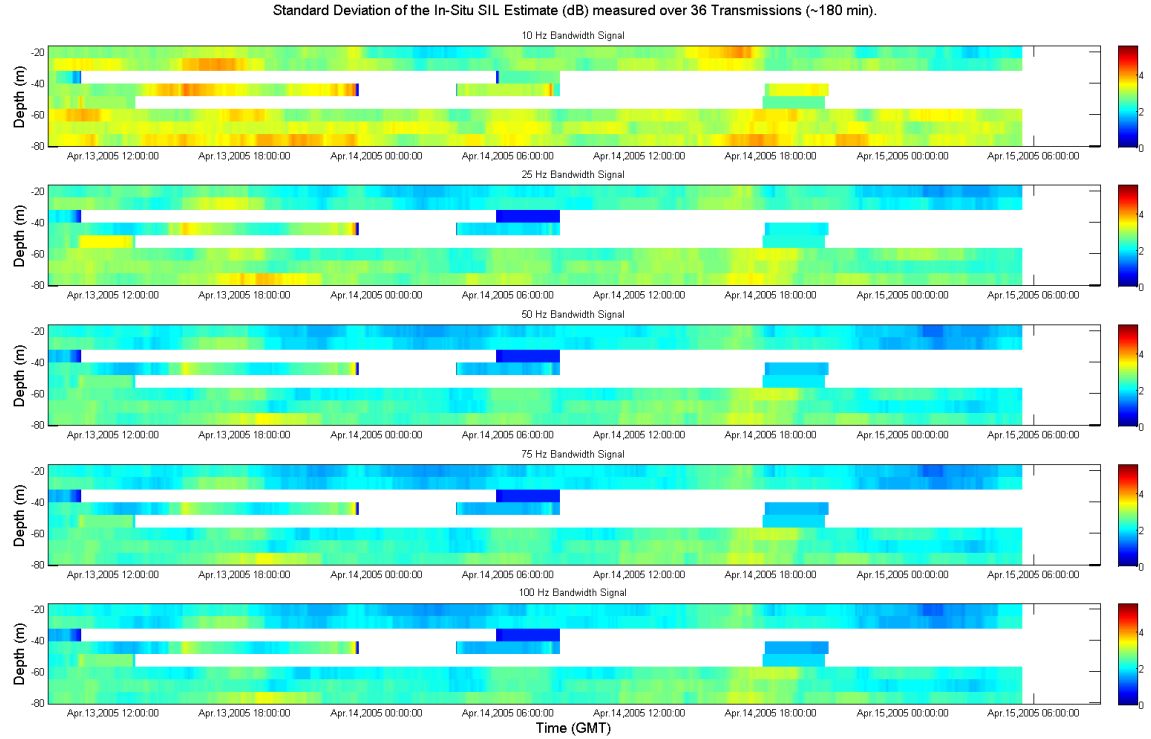
Figure 33.   The standard deviation of the measured sound intensity (dB) associated with the bandpass filtered 10-, 25-, 50-, and 75-Hz bandwidth signal as well as the original 100-Hz bandwidth signal. The standard deviation was calculated from the measured intensities using a 180 minute window.

Before proceeding to the next Section, it is important to summarize the results from the statistical analysis thus far. First, the statistics of both the modeled and measured intensity are clearly sensitive to the bandwidth of the received signal. The variance of the sound intensity was observed to increase (decrease) as the bandwidth decreased (increased). Second, because the pulse-width of an arrival (i.e., its temporal resolution) is inversely proportional to the bandwidth of the received signal, the ability to resolve two adjacent arrivals depends not only on their temporal separation, but also on their pulse-width (Fig. 31). Thus, based on these two observed results, it can be inferred that as the pulse-width of the individual arrivals increases (decreases) due to narrowing (broadening) of the received signal's bandwidth, adjacent arrivals will begin to overlap one another (become well separated from one another) resulting in both fewer (more) independent arrivals and an increase (decrease) in the magnitude of the variance. These results are in complete agreement with the proposed hypothesis. Lastly, the variance associated with

80

the intensity fluctuations are time-dependent, whose magnitude is heavily influenced by the periodic presence/absence of a highly energetic internal wave field. However, expanding the temporal window of the variance measurements acted to "smooth out" the temporal variations of the calculated variance and converged the variance perturbations towards a constant value. The convergence of the variance perturbations to a constant value suggests that the statistics of the SIL estimates, if calculated over a long enough temporal "window," which would include numerous high frequency wave events, will reach saturation. This will be a critical concept in the next Section when validating the proposed hypothesis. The final remaining task in Objective 2 is to devise a method that will reliably determine the number of arrivals and relate them to the observed variance. The methodology used to determine the number of arrivals for each bandwidth will be discussed next.

D. RELATING THE OBSERVED STATISTICS TO NUMBER OF ARRIVALS (VALIDATING THE HYPOTHESIS)

1. Determining the Number of Arrivals

An objective approach was taken when attempting to determine the number of arrivals present in the signal segment. Originally, in order to be consistent with the previous Section in this dissertation, the signal segment from 19.0-s to 19.95-s (blue segment, Fig. 34) was used when calculating SIL estimates and the noise segment from 22.0-s to 22.95-s (green segment, Fig. 34) was used for noise analysis. The first task was to establish a signal-to-noise threshold that would, when applied, confidently and consistently identify arrivals associated with the received signal and not a peak resulting from matched-filter noise. This signal-to-noise threshold (green horizontal line, Figs. 34 and 35) was calculated by finding the peak value in the noise segment, and doubling it. This method established a dynamic signal-to-noise threshold based solely on the maximum noise level recorded in the noise segment. For a peak to be considered a significant arrival, the magnitude of the peak must be +6 dB (i.e., twice the amplitude of the peak noise value) above the noise. Arrivals found to exceed this threshold were considered significant arrivals originating from the sound source rather than processor noise.
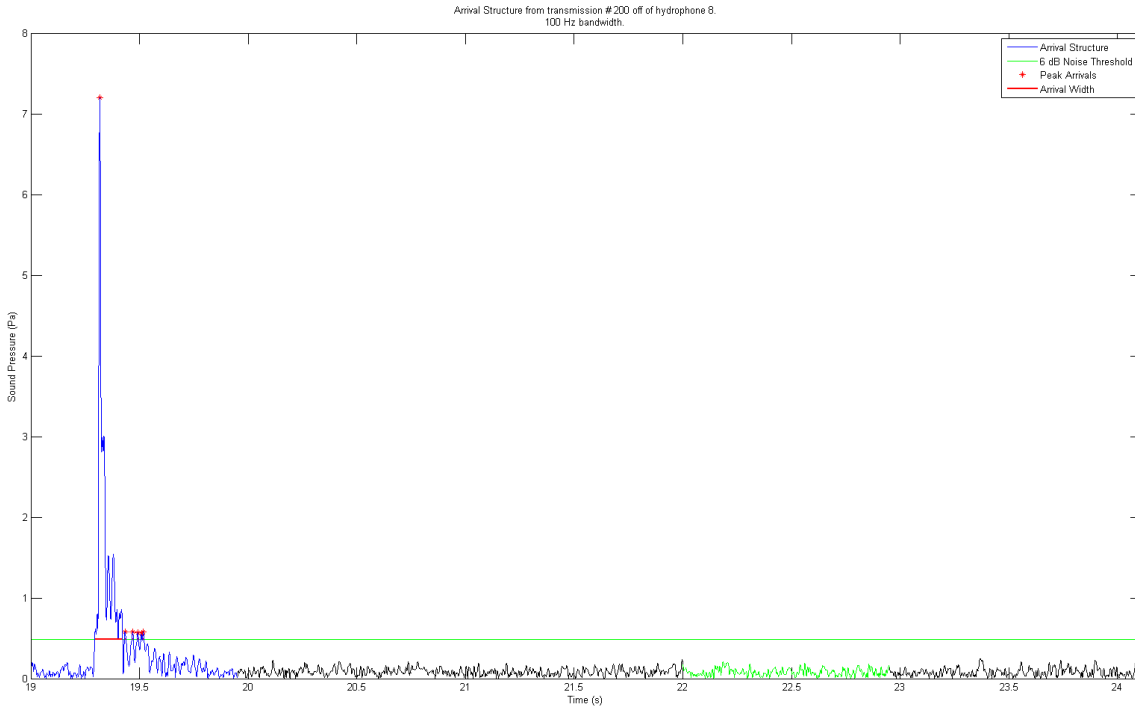
Figure 34.   Example arrival structure associated with a 100-Hz bandwidth signal. The signal segment used to generate the SIL estimates has been colored blue, while the noise segment has been colored green. The green horizontal line is the noise threshold which is 6 dB above the highest observed value in the noise segment.

Examining Fig. 35, one should note the long, temporal width of the first arrival (lasting from approximately 19.3-s to 19.42-s). This arrival is obviously composed of several overlapping individual ray/mode arrivals and raises the following questions: Do the smaller amplitude, later arrivals that exceed the noise threshold contribute to the sound intensity level variance? Additionally, what temporal separation should be required between two adjacent arrivals in order to be classified as two independent arrivals (i.e., "well separated")? All of these factors were investigated during the course of this research and will be discussed in the subsequent paragraphs.
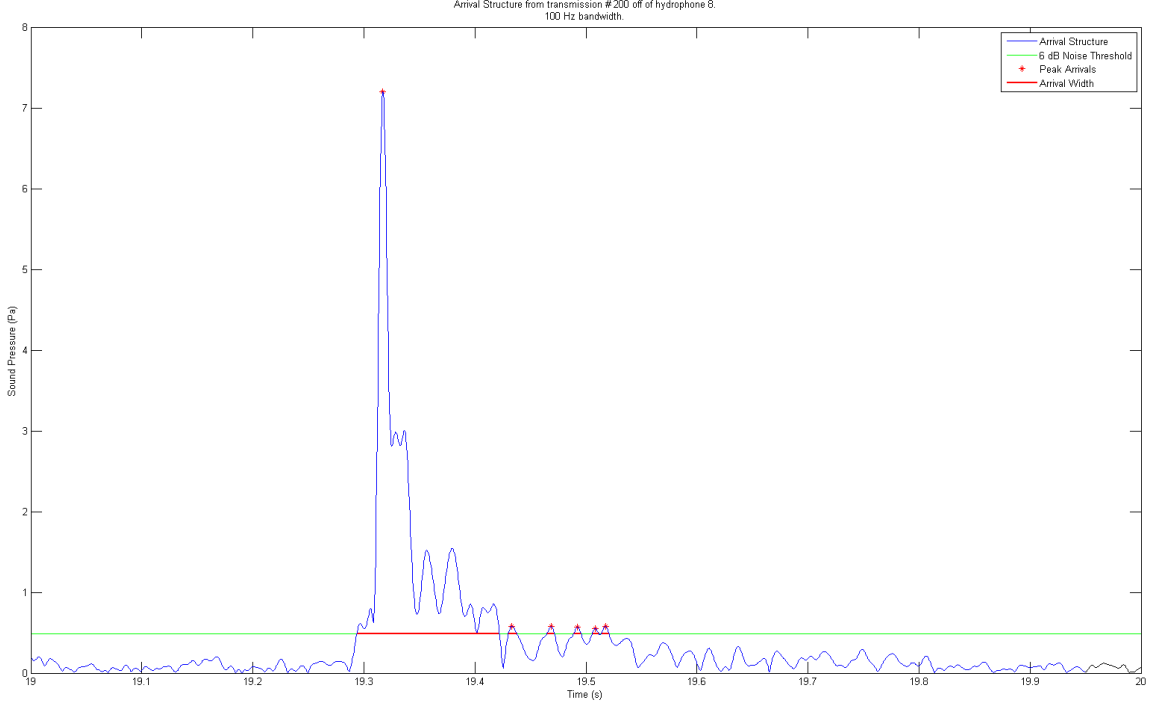
Figure 35.   Same as Fig. 34, however, the signal segment has been enlarged in order to show the temporal width of each arrival (red line) within this arrival structure. The peak values within each arrival have also been identified (red asterisk).

a.   *Arrivals Found within the Full Signal Segment*

To examine the significance of the late arrivals, two methods were used to analyze the signal. The first method considered all arrivals that exceeded the noise threshold over the full temporal length of the signal segment (i.e., from 19.0-s to 19.95-s) as significant and were used when calculating the DOF. The second method (to be discussed in paragraph IV.D.1.b.) would remove many of the later, smaller amplitude arrivals by only using the arrivals found to exceed the noise threshold in an abbreviated signal segment (i.e., from 19.0-s to 19.4-s) when estimating the DOF. The final question to be addressed is assigning the appropriate number of DOF to the arrivals. Although other methods were examined (and will be briefly mentioned in the closing paragraph), treating broad, overlapping groups of arrivals that were sufficiently separated from adjacent arrival groups (i.e., based on the temporal separation requirement) as independent degrees of freedom proved the most successful and is discussed next.

Using the +6 dB noise threshold as a guide to confidently identify multipath arrivals from processor noise, a method was devised that treated overlapping arrivals (hence, arrival groups) as a significant, independent arrival. This method calculated the DOF based on two parameters. The first parameter was simply calculating the number of "arrival groups". An "arrival group" value of one was assigned to any portion of processed signal that exceeded the noise threshold. It simply assigned any signal segment that exceeded the noise threshold two degrees of freedom. For example, in Fig. 35 there were six signal segments where the amplitude of the processed signal exceeded the noise threshold; consequently, twelve degrees of freedom were assigned to this arrival structure.

The second parameter this method attempted to quantify is when adjacent arrivals should be treated as independent arrivals, vice grouped together. For example, in Fig. 35, the last two arrivals are very closely spaced. If the noise threshold were to decrease slightly, then these two arrivals would no longer be separated and the degrees of freedom would decrease by two. Consequently, because the noise threshold is somewhat arbitrary and the temporal position of these arrivals will oscillate slightly about a mean travel time over the course of several arrival structures, there could be inconsistency on the degrees of freedom assigned to them. To prevent this, a temporal separation requirement between adjacent arrivals was established to aid in the proper DOF calculation. This requirement essentially separated independent arrivals from a group of adjacent arrivals by examining their temporal separation. If the spacing between two adjacent arrival groups exceeded the temporal threshold, then the arrival groups were treated as two independent arrival groups and were assigned four degrees of freedom. Conversely, if the separation between the two adjacent arrival groups did not exceed the defined temporal separation, then the two arrival groups were treated as one, broad arrival group and were assigned two degrees of freedom.

Two different definitions of pulse-width were used during this study. The first, which will be referred to as the "narrow" pulse-width, was defined as twice the temporal width between the peak value and a 3 dB decrease in amplitude. The other, which will be referred to as the "broad" pulse-width, was determined by the temporal

width of the base of the pulse. Utilizing the two pulse-width definitions as the temporal separation requirement, two different thresholds were used in an attempt to isolate independent arrival groups.

The estimated DOF calculated by the "group" method, utilizing either the "narrow" or "broad" pulse-width as the temporal separation requirement, are presented in Figs. 36 and 37, respectively. Analysis of Figs. 36 and 37 indicate that the estimated DOF experiences severe fluctuations when using either the "broad" and "narrow" temporal separation requirement. This was a surprising result and a significant observation of this research. The cornerstone of Dyer's statistical theory and the proposed hypothesis in this dissertation is the assumption that the arrival structures are stable and the statistics of the intensity fluctuations result primarily from the phase randomness of the received signal. Both Figs. 36 and 37 suggest that the arrival structures are not stable, but rather changing in time possibly due the high-frequency wave field. In order to determine if the periodic, high frequency internal wave field is causing fluctuations in the estimated number of arrivals, a comparison between the standard deviation of the estimated DOF and the standard deviation of the estimated SIL was made and is discussed next.

Figure 38 shows the standard deviation of the fluctuations in the SIL estimates using a 10 minute window, while Figs. 39 and 40 show the standard deviation of the estimated DOF measured over the same temporal range. Examination of Fig. 38 reveals four broad periods during which the standard deviation of the SIL estimate reaches a maximum. Although present in all five bandwidths, the maxima are more pronounced in the 50-, 75-, and 100-Hz bandwidth signals. The variance of the SIL estimates were observed to increase from 13:00 – 21:00 April 13, 03:00 – 09:00 April 14, 13:00 – 21:00 April 14, and 05:00 – 08:30 April 14, 2005.

Comparison between of Fig. 38 and Figs. 39 and 40 reveal a striking correlation between high variance periods observed in the SIL estimates to the variability observed in the DOF estimates. Regardless of the pulse-width definition, roughly five periods of standard deviation maxima in the DOF estimates were observed, namely, 13:00 – 22:00 April 13, 03:00 – 09:00 April 14, 13:00 – 21:00 April 14, 22:00 – 01:00 April 14, and 05:00 – 08:30 April 14, respectively. With the exception of the fourth high

variance period observed in the DOF estimate time-series, the periods of variance maxima between the SIL estimates and DOF estimates almost perfectly coincide.

Before proceeding to the next Section, it is important to summarize the results from the statistical analysis of the DOF estimates and their correlation to the sound intensity variance. First, DOF estimates are highly variable. This variability indicates that either the arrival structures are unstable or the noise threshold is fluctuating (i.e., the amount of the signal that exceeds the noise threshold is fluctuating which, in turn, affects the number of significant arrivals (red line, Figs. 34 and 35)). Second, periods of variance maxima between SIL estimates and DOF estimates appear to correspond. This is significant because the statistics of SIL estimates are not dependent upon the noise threshold. Consequently, any observed variability in the intensity measurements is completely dependent on the fluctuations of the arrival structure, not the noise threshold used in this Section to detect significant arrivals. Because the standard deviation maxima and minima of the DOF estimates and the SIL estimates show such a strong correlation with each other, one can infer that the cyclical high frequency nonlinear internal wave field, rather than the random process of ambient or processor noise, is driving the statistics. Consequently, if noise isn't causing the fluctuations observed in the DOF estimates, then the shape of the arrival structure (i.e., both amplitude/phase and travel time) must be changing. This is a significant result. Not only are the arrival structures unstable (Figs. 36 and 37), but their variability (i.e., estimated DOF) appears connected to the variance induced by the high-frequency nonlinear internal wave field. In the next Section, the late arrivals will be removed from the analyzed signal and the statistics of the abridged signal are examined.
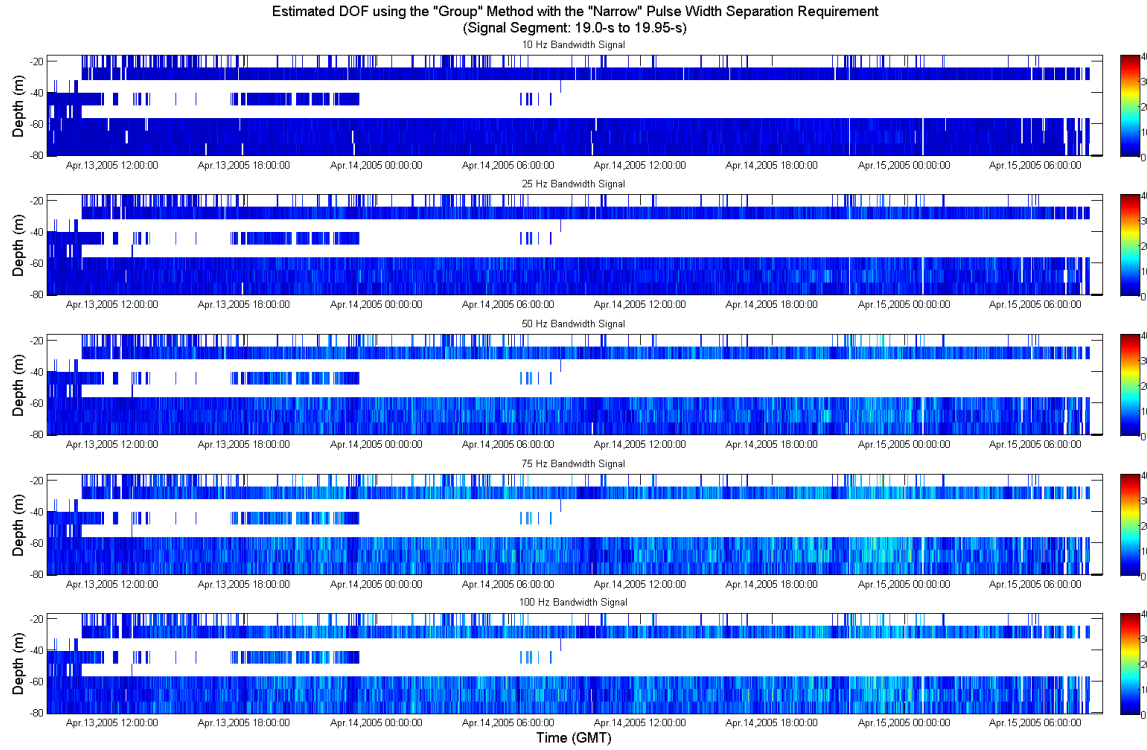
Figure 36.   Estimated DOF using the "group" method and the "narrow" pulse-width
separation requirement between adjacent arrival groups.
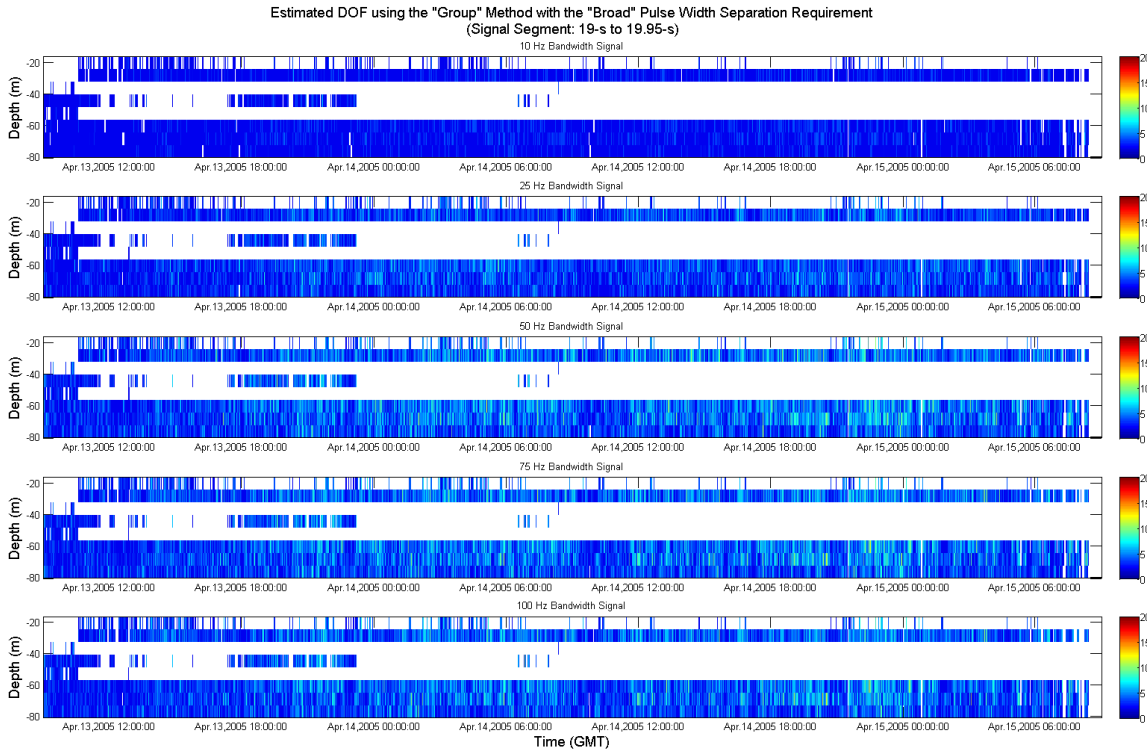
Figure 37.   Estimated DOF using the "group" method and the "broad" pulse-width
separation requirement. Note the range scale is different from that of Fig. 36.

87
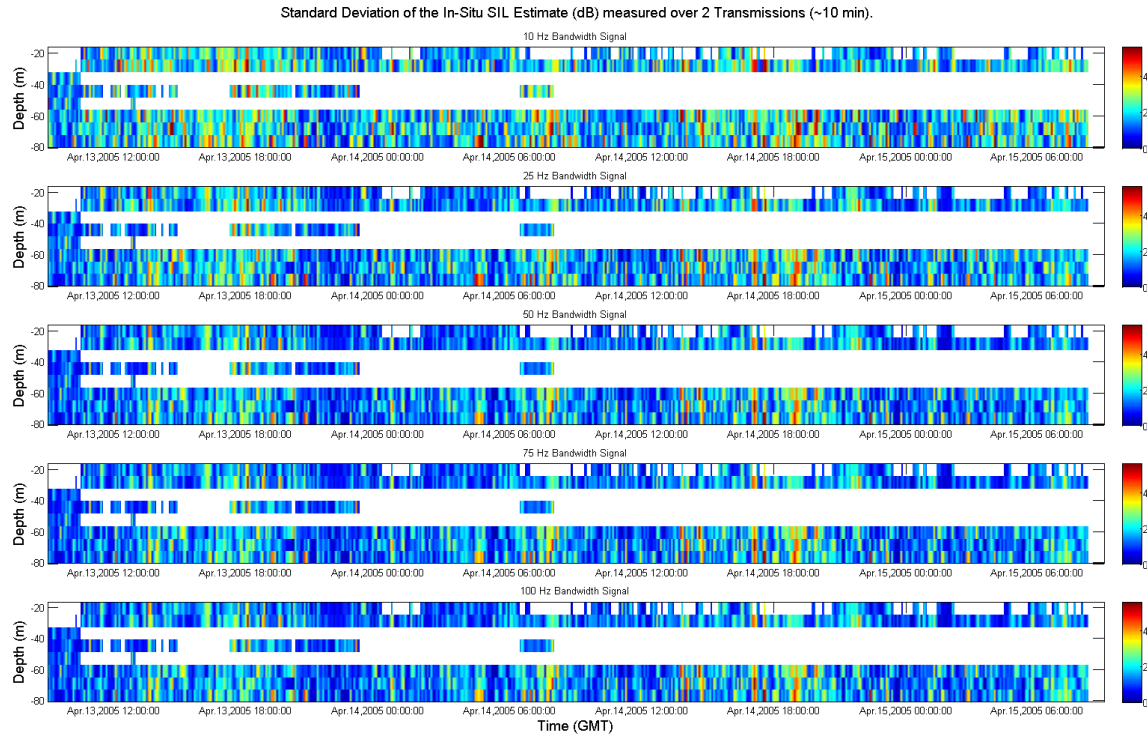
Figure 38.   Standard deviation associated with the measured SIL estimates (dB) as measured over 10 minutes.
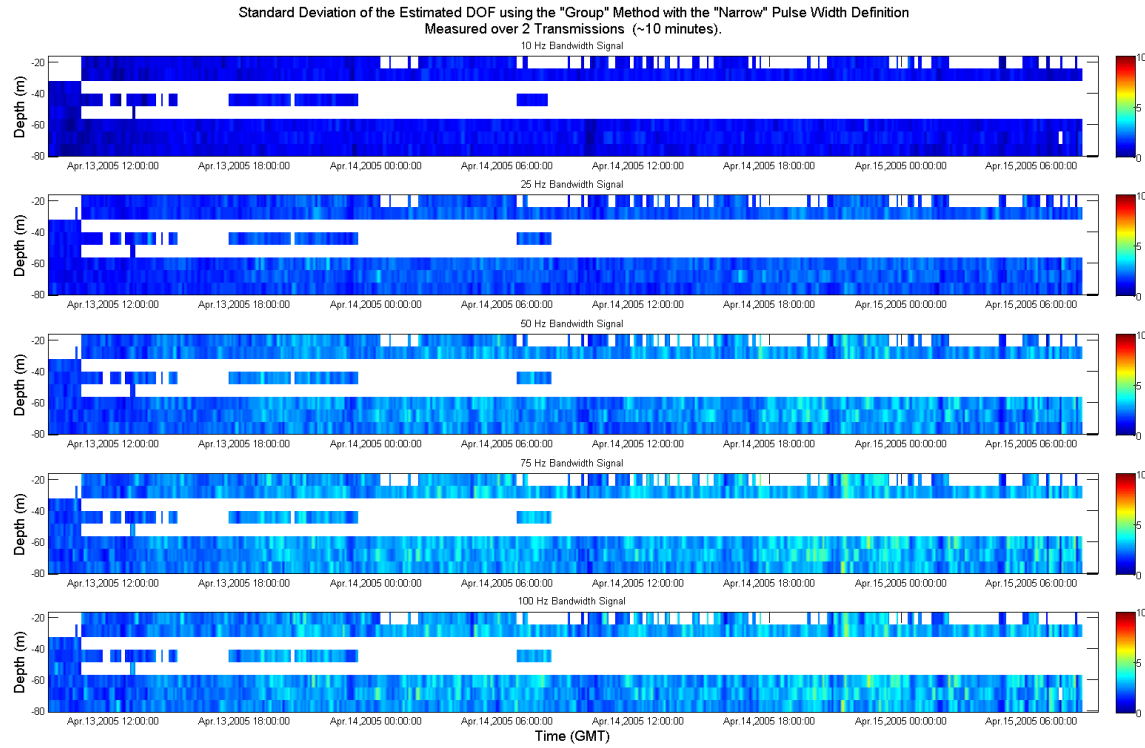
Figure 39.　Standard deviation of the estimated DOF from Fig. 36 (i.e., "group" method and "narrow" pulse-width).
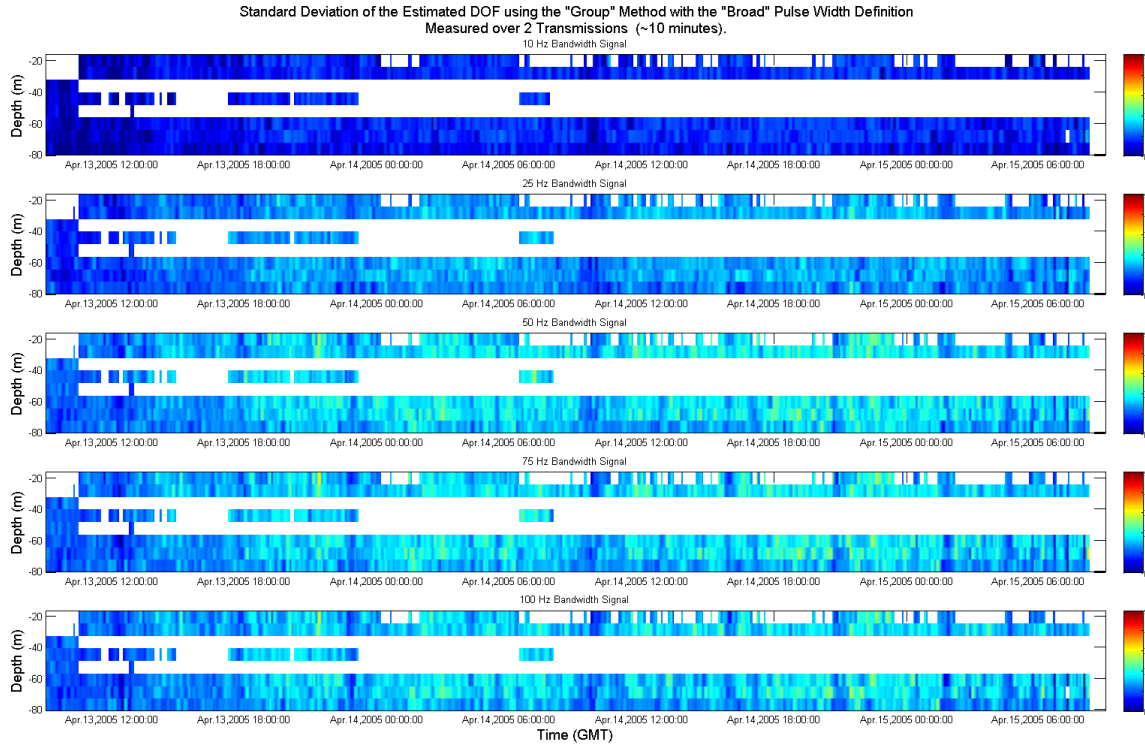
Figure 40.　Standard deviation of the estimated DOF from Fig. 37 (i.e., "group" method and "broad" pulse-width).

As mentioned before, an "abridged" portion of the signal was examined in order to analyze the significance of the late arrivals. The "abridged" signal was defined from 19.0-s to 19.4-s. The 19.4-s cutoff was selected because it was found to be a good separation point between the early, high amplitude arrivals and the later, small amplitude arrivals. It should be noted that the cutoff of 19.4-s was not fixed. In some cases, arrivals, whose amplitude exceeded the noise threshold, would extend beyond the 19.4-s cutoff. As long as more than 50% of its arrival width was found before the 19.4-s cutoff, the arrival was used to estimate the DOF. As before, both the "narrow" and "broad" pulse-width definitions were used as the temporal separation requirements between adjacent arrival groups and the results are discussed next.

Similar to results in the previous Section, the estimated degrees of freedom using the abridged signal segment fluctuated with time. Variability maxima in the DOF continued to coincide with variance maxima from the intensity estimates (not shown), again suggesting that the high-frequency nonlinear internal wave field was dominating the short-term statistics. Due to the "abridged" signal and temporal separation requirement between arrivals, a minimal number of DOF were calculated using both the "narrow" and "broad" temporal separation requirements. Because the main arrival group was very broad and dominated the "abridged" signal, this method significantly underestimated the estimated DOF.

2. Relating Average Number of Arrivals to the Measured Variance of the Sound Intensity Level

There are three critical points to understand how the proposed hypothesis relates the number of arrivals to observed variance of the intensity measurements. First, this hypothesis assumes that the arrival structure is stable (i.e., the number of non-overlapping arrivals is invariant or, if the estimated number of arrivals does fluctuate, then the deviation of the number needs to be small). Second, the phase randomness of each individual arrival resulting in either constructive or destructive interference of the pressure field when reaching the hydrophone concurrently with other arrivals will drive

the observed statistics of the intensity measurements. Third, the hypothesis requires a variance time window large enough to collect a sufficient number of samples from numerous wave events in order to reach phase randomness in the sample population.

The results from the estimated DOF study clearly suggest that arrival structures were not stable along the transmission path. The number of arrivals fluctuated as a result of the passage of nonlinear internal waves along the acoustic path. As a result, for each variance measurement of the acoustic intensity, the estimated number of arrivals fluctuated. Consequently, within each of these variance windows, there existed a sample population of estimated number of arrivals. Assuming the proposed hypothesis is valid and the three critical points are met, this sample population should be able to relate the estimated number of arrivals to the measured variance of the acoustic intensity (i.e., follows the curve in Fig. 28). Note that for each variance measurement of the sound intensity, there is a corresponding estimated DOF sample population distribution where both the mean number of arrivals and the variance of the number of estimated arrivals are always greater than zero. The fact that the estimated DOF has a distribution is an important concept. As with any distribution, there will be the most common value (i.e., the mean number of estimated DOF) and other moments that can be calculated. Thus, for each variance measurement of the sound intensity, there will be corresponding mean number of arrivals determined. Attempts to relate the most common (i.e., averaged estimated DOF) value to the observed intensity fluctuations will be discussed next.

Figure 41 depicts the evolution of a series of scatter plots based on the average number of arrivals and the corresponding variance in the acoustic intensity using progressively larger variance windows for four out of the five broadband signals. In other words, for each variance measurement of the acoustic intensity, an average estimated DOF (i.e., twice the averaged number of arrivals) was calculated from the sample population collected over the defined variance window. Once the averaged estimated number of arrivals and variance of the observed intensity was calculated, they were plotted against each other in Fig. 41. It should be noted that when the results from the 75-Hz and 100-Hz bandwidth signal were plotted, they tended to overlap each other. In this study, the received bandwidth of the 400-Hz sound source signal was assumed to be 100-

Hz. However, the true bandwidth of the received signal was probably closer to 75-Hz. This would explain why the results between the two broadband signals overlapped one another. Because plotting both the results from both broadband signals does not add any information to the analysis, only the results from one of the signals will be presented in the scatter plots (i.e., the original 100-Hz bandwidth signal).

If the proposed hypothesis is valid, the method of estimating the number of arrivals is correct, and the three critical requirements are met, then the scattered values from each of the broadband signals should converge toward the red line depicted in Fig. 28. Using the methodology from the "full signal" study and a temporal separation requirement equivalent to 80% of the "narrow" pulse-width definition, the average number of resolvable arrivals and the associated standard deviation of the acoustic intensity for four expanding variance windows were calculated and plotted. Starting in the upper left and working clockwise, Fig. 41 depicts how step increases in the variance window affects the distribution of the statistics of both the measured intensity variance and the average estimated number of arrivals. By increasing the variance window from 10 minutes to 90, 300 and finally 1440 minutes (i.e., 24 hours), the variance of the sound intensity for each broadband signal converged toward a constant value (i.e., less scattering along the vertical axis). Additionally, the larger sample size of the estimated number of arrivals drove the mean of the sample population toward the true mean of the parent population (i.e., less scattering along the horizontal axis). The agreement between the observed variance of intensity and the average number of arrivals found within the 24-hour variance window is excellent.

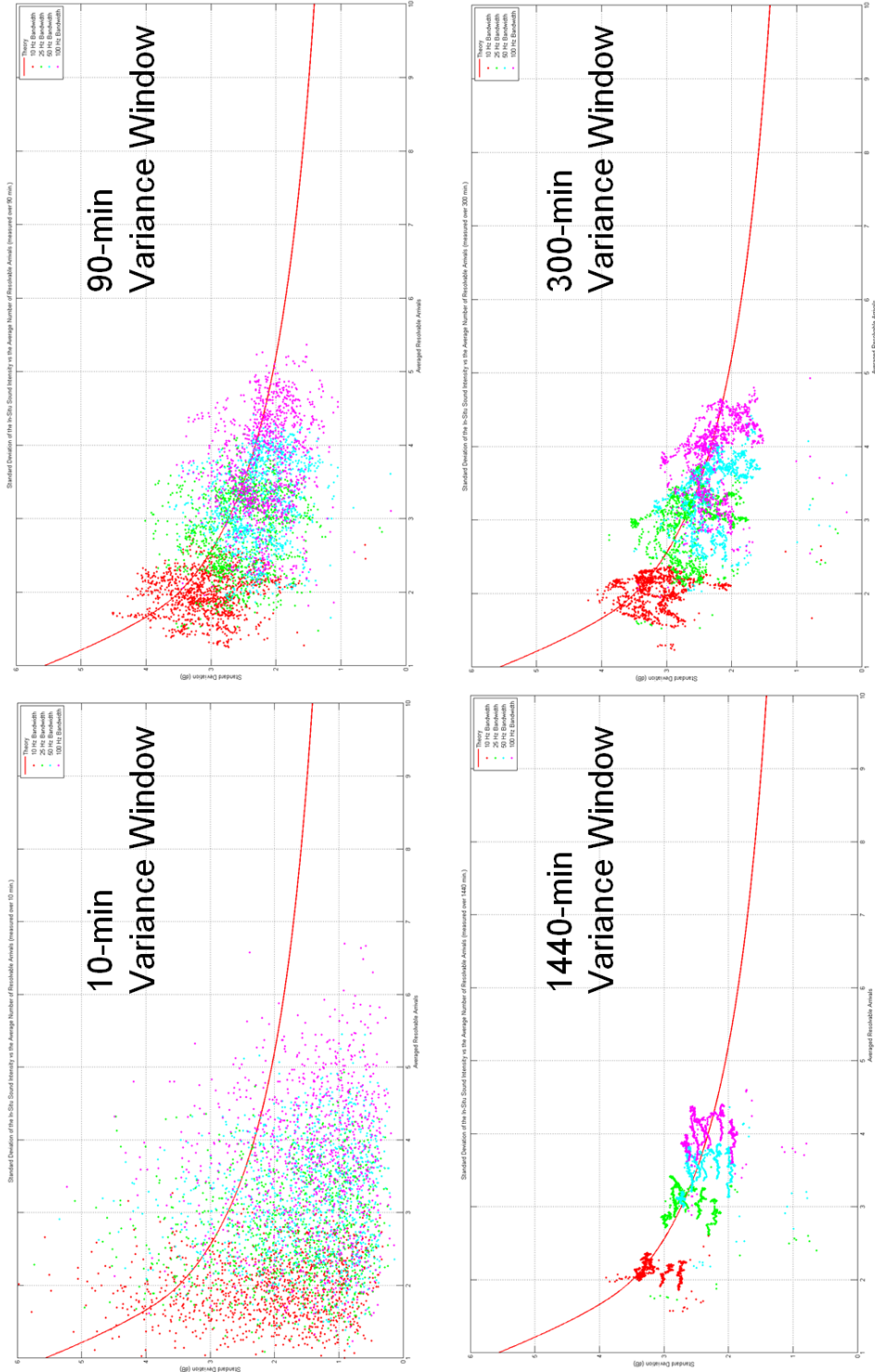Figure 41.   When the variance time window is extended temporally, the proposed
hypothesis that relates the average number of arrivals to the statistics of the
acoustic intensity converges toward the theoretical curve. Similar to Fig. 24, the
horizontal axis is the averaged estimated number of arrivals while the standard
deviation associated with the measured SIL (dB) is plotted on the vertical axis.

Taking into consideration the variance windows chosen when calculating the standard deviation of the intensity fluctuations and the mean of the estimated number of arrivals, the results analyzed in Fig. 41 were expected. When using a short-term variance window (i.e., 10 and 90 minutes), the scatter plots depict the attempt to relate the average number of arrivals to a statistical measurement that does not meet the three critical assumptions of the proposed hypothesis. As observed in the previous Section, when using such a short time window to estimate the DOF, the arrival structures were not stable and the variance of the estimated number of arrivals was large due to the presence/absence of highly energetic, nonlinear internal waves along the acoustic path. These temporally variant internal wave activities add significant variability to the short-term statistics of the acoustic intensity measurements and results in the vertical spread of their measured statistics in the scatter plots. Also consider that, at most, a 10 minute variance window only provides 448 independent realizations of the estimated DOF (assuming all eight hydrophones didn't experience any hardware failure). With such a limited sample size, the sample population will not contain enough samples from nonlinear wave events to ensure that the sample statistics originate from a sample population whose phase distribution is uniformly random. With only 448 realizations, the sample population of the estimated DOF was too small to confidently determine the mean of the parent population (i.e., the true DOF) as well. By expanding the variance window, the sample size will increase, resulting in a sample population whose statistical distributions will be based on a uniform phase random distribution and whose number of temporally disjoint arrivals will approach a constant ensemble mean while the variance of the estimated number of arrivals approaches zero.

One last examination of the Fig. 41 reveals a series of roughly four "variance bands" when the variance window was expanded to 1440 minutes (i.e., 24-hours). This banding can be observed in the scatter plot of all four bandwidths. These bands resulted from the technique used to calculate the standard deviation of the measured SIL. Because all eight hydrophones were used when calculating the variance, the sample population

from a hydrophone that experience intermittent failure (i.e., hydrophones 1 and 3) had slightly different statistics than a hydrophone that did not experience hardware failure (i.e. the bottom three hydrophones).

THIS PAGE INTENTIONALLY LEFT BLANK

V. CONCLUSIONS

The sound-speed field found along the shelf region in the northeast portion of the South China Sea is extremely dynamic where varying temporal and spatial scale processes dominate the observed fluctuation in the sound-speed field. Significant variability in the sound-speed field was observed to be induced by the broad expansion/compression of sound-channel associated with the nonlinear internal tides as well as the narrow, high-frequency, nonlinear internal depression and elevation waves superimposed on this long-wave pattern.

Analysis of the measured acoustic transmissions revealed that the mean vertical distribution of the sound intensity time-series followed the compression/expansion of the sound-channel associated with the internal tides. Additionally, the strong horizontal sound-speed gradient found along the leading (trailing) edge of elevation (depression) waves effectively scattered sound energy into higher (higher and lower) acoustic modes.

Two different vertical distributions of the sound intensity fluctuations were observed depending on the type of episode. Standard deviation maxima of the measured SIL were confined to the lower half of the water column when elevation wave packets were observed in the vicinity of the hydrophone array. With a compacted sound-channel, the scattering of acoustic energy was limited to very low acoustic modes. Additionally, energy that was scattered into higher modes was stripped off after several interactions with the bottom, thus making it an extremely localized event. Additionally, when depression waves were transiting over the sound source, the variability in the SIL was confined to the lower half of the water column due to the suppression of higher acoustic modes near the sound source. With most of the sound energy initially limited to the lowest acoustic modes, acoustic energy could only be scattered out of the lowest acoustic modes. However, when depression waves transited across the hydrophone array, the standard deviation maxima of the observed SIL was much more vertically diffuse. During these events, the expanded sound-channel driven by the internal tides allowed for the excitation and propagation of additional acoustic modes. With a larger number of

acoustic modes available to scatter energy, the strong horizontal sound-speed gradient found along the trailing edge of these narrow, depression waves effectively scattered acoustic energy throughout the water column.

EOF decomposition of the temperature time-series collected from the five environmental moorings allowed for the generation of an empirical, two-dimensional sound-speed field that was continuous in both space and time for use within an acoustic model. Comparisons between the modeling results from the coupled, normal-mode acoustic model and the analyzed data from the hydrophone array revealed that the empirical sound-speed model was able to reasonably reproduce the vertical distribution of the sound intensity time-series resulting from the long-wave pattern, as well as the vertical distribution of the sound intensity fluctuations resulting from pulse propagation through an acoustic path occupied by nonlinear depression waves. The empirical sound-speed model, however, was not able to replicate the transformation of a depression wave into a series of elevation waves. Consequently, because the empirical sound-speed model could not model the transforming nonlinear internal waves observed in the mooring data, no explanations toward the phenomenology of the observed sound intensity fluctuations resulting from elevation waves near the receiver can be made. However, the confinement of the vertical distribution of acoustic energy fluctuations to the lower portion of the water column may have been due to the compressed sound-channel associated with an elevation wave event. With a compressed sound-channel, only the lowest acoustic modes would be able to propagate along the acoustic path, resulting in most of the acoustic energy focused toward the bottom. The strong horizontal sound-speed gradient associated with the edge of the nonlinear elevation waves may have allowed weak scattering of the bottom-focused, acoustic energy into higher neighboring acoustic modes; however, because of the compressed sound-channel, the weak acoustic energy scattered into these higher acoustic modes may have been quickly been stripped away by the bottom.

The acoustic modeling results during which time a depression wave was observed along the acoustic path helped to explain some of the measurements noted from the hydrophone data. First, the compression/expansion of the sound-channel along the acoustic path (i.e., the long-wave pattern) controlled both the vertical distribution of the

acoustic intensity and which acoustic modes were initially excited. Although acoustic modes from three acoustic mode groups were initially excited when in close proximity to the sound source, only the lowest members (1-3) of the low acoustic mode group were able to reach the hydrophone array when the sound-channel was compressed, as higher acoustic modes were either suppressed or quickly stripped away by the bottom. As the sound-channel expanded over either the partial or the full length of the acoustic path, additional members (1-6) of the low acoustic mode group were initially excited and acoustic energy spread into the mid- and lower portions of the water column. Second, severe fluctuations in the vertical distribution of the sound intensity appear to result from the strong horizontal sound-speed gradient found along the leading (trailing) edge of elevation (depression) waves. The vertical scattering of sound energy was linked to strong acoustic mode-coupling along the nonlinear internal wave-front. The acoustic modeling results suggest that the nonlinear internal wave-front interface allows for the effective scattering of acoustic energy from low acoustic modes into higher acoustic modes. However, if the scattering of energy into higher acoustic modes due to acoustic mode-coupling occurs too far from the hydrophone array, the acoustic energy scattered into the higher acoustic modes may be stripped out by the bottom. Finally, although three acoustic mode groups are initially excited near the acoustic source, the intermediate and high acoustic mode groups appear to contribute little (if any) energy to the sound intensity level. Acoustic energy from the highest acoustic mode group (18-25) is quickly stripped by the bottom prior to reaching the hydrophone array, while the intermediate acoustic mode group (8-16) appears to contribute minimally to the observed sound intensity.

The results from the second objective indicate that is possible to predict the variance of the transmission loss based on the mean number of arrivals if the temporal separation between adjacent arrivals is properly defined and the phase distribution of the sample population is uniformly random. As indicated in the hypothesis, the number of resolvable arrivals was found to depend on the received signal bandwidth and the criteria of "well-separateness." Once a technique was established to properly identify significant arrival against processor noise, four different methods of calculating the number of

arrivals were examined to assess the significance of early versus late arrivals (i.e., full vs. abridged signal length), as well as two different temporal separation requirements between adjacent arrival groups based on two definitions of pulse-width. The estimated number of arrivals was observed to fluctuate wildly in all four methods, thus indicating an unstable arrival structure. A strong correlation was observed between the standard deviation maxima of the estimated number of arrivals and the standard deviation maxima of the measured sound intensity suggesting that the high frequency nonlinear internal wave field, not the background noise, is driving the variability observed in the short-term statistics. Attempts at relating the estimated number of arrivals to the short-term fluctuations in the sound intensities were unsuccessful for several reasons. First, the proposed hypothesis requires that the standard deviation of the estimated number of arrivals be small. When using a short variance window, the standard deviation of the estimated number of arrivals will be large, especially when highly energetic, nonlinear internal waves are found along the acoustic path. If the variance window is expanded, the sample size will increase, thus reducing the variance of the estimated number of arrivals. Additionally, as the sample population is increased, the confidence in the mean of estimated number of arrivals will increase as the sample mean approaches the parent mean. Second, the proposed hypothesis requires a sample population whose statistical distributions are based on a uniform phase random distribution. Short-term statistics provide a limited sample size, thus the sample population will not contain enough samples from the various nonlinear wave events to ensure that the calculated statistics originate from a sample population whose phase distribution is uniformly random. If the variance window is expanded, the sample population increases and this discrepancy can be overcome. Lastly, the short-term standard deviation of the measured sound intensity is time-variant due to the presence/absence of highly energetic, nonlinear internal waves along the acoustic path. These temporally variant internal wave activities resulted in a significant increase in the volatility of short-term statistics of the acoustic intensity measurements. Again, by expanding the variance window, the temporal variability in the standard deviation of the observed sound intensity was minimized.

100

Once the variance window was allowed to expand to a necessary temporal width (i.e., approximately 12- to 24-hours) and the temporal separation requirement between adjacent arrival groups was properly defined, the alignment between the theoretical curve of the proposed hypothesis and the scatter plots which related the estimated number of arrivals to the standard deviation of the sound intensity was excellent.

THIS PAGE INTENTIONALLY LEFT BLANK

LIST OF REFERENCES

Chiu, C. –S., and Y. Desaubies, 1987: A planetary wave analysis using the acoustic and conventional arrays in the 1981 Ocean Tomography Experiment. *J. Phys. Oceanogr.*, **17**, 1270-1287.

Chiu, C. –S., A. J. Semtner, C. M. Ort, and J. H. Miller, 1994: A ray variability analysis of sound transmission from Heard Island to California. *J. Acoust. Soc. Amer.*, **96**, 2380-2388.

Chiu, C. –S., J. H. Miller, W. W. Denner, and J. F. Lynch, 1995: A three-dimensional, broadband, coupled normal-mode sound propagation modeling approach. *Full Field Inversion Methods in Ocean and Seismic Acoustics*, O. Diachok, A. Caiti, P. Gerstoft, and H. Schmidt, Editors, Kluwer Academic Publishers, Boston, MA, 57-62.

Chiu, C. –S., J. H. Miller, and J. F. Lynch, 1996: Forward coupled-mode propagation modeling for coastal acoustic tomography. *J. Acoust. Soc. Amer.*, **99**, 793-802.

Chiu, C. –S., S. R. Ramp, C. W. Miller, J. F. Lynch, T. F. Duda, and T. Y. Tang, 2004: Acoustic intensity fluctuations induced by South China Sea internal tides and solitons. *IEEE J. Oceanic Eng.*, **29**, 1249-1263.

Clark, V., 2002: Sea Power 21 Series – Part 1: Projecting Decisive Joint Capabilities. *Proceedings- United States Naval Institute*, **128**, 32-41.

Duda, T. F., J. F. Lynch, J. D. Irish, R. C. Beardsley, S. R. Ramp, C. -S. Chiu, T. Y. Tang, and Y. –J. Yang, 2004a: Internal tide and nonlinear internal wave behavior at the continental slope in the Northern South China Sea. *IEEE J. Oceanic Eng.*, **29**, 1105-1130.

Duda, T. F., J. F. Lynch, A. E. Newhall, L. Wu, and C. –S. Chiu, 2004b: Fluctuation of 400-Hz sound intensity in the 2001 ASIAEX South China Sea experiment. *IEEE J. Oceanic Eng.*, **29**, 1264-1279.

Dyer, I., 1970: Statistics of sound propagation in the ocean. *J. Acoust. Soc. Amer.*, **48**, 337-345.

Harrison, C. H., and J. A. Harrison, 1995: A simple relationship between frequency and range averages for broadband sonar. *J. Acoust. Soc. Amer.*, **97**, 1314-1317.

Hsu, M. -K., and A. K. Liu, 2000: Nonlinear internal waves in the South China Sea. *Canadian J. Remote Sensing*, **26**, 72-81.

Hull, R. E., 1996: The South China Sea: Future source of prosperity or conflict in South East Asia? *Strategic Forum Number 60*, Institute for National Strategic Studies, National Defense University, Washington, D.C.

Liu, A. K., Y. S. Chang, M. –K. Hsu, and N. K. Liang, 1998: Evolution of nonlinear internal waves in the East and South China Seas. *J. Geophys. Res.*, **103**, 7955-8008.

Makris, N. C., 1996: The effect of saturated transmission scintillation on ocean acoustic intensity measurements. *J. Acoust. Soc. Amer.*, **100**, 769-783.

Marburger, J. M., 2004: Estimation of geoacoustic properties in the South China Sea shelf using a towed source and vertical line hydrophone array. M. S. Thesis, Dept. of Oceanography, Naval Postgraduate School, Monterey, CA.

Medwin, H., 1975: Speed of sound in water: A simple equation for realistic parameters. *J. Acoust. Soc. Amer.*, **58**, 1318-1319.

Orr, M. H., B. H. Pasewark, S. N. Wolf, J. F. Lynch, T. Schroeder, and C. -S. Chiu, 2004: South China Sea internal tide/internal waves – Impact on the temporal variability of horizontal array gain at 276 Hz. *IEEE J. Oceanic Eng.*, **29**, 1292-1308.

Ramp, S. R., T. Y. Tang, T. F. Duda, J. F. Lynch, A. K. Liu, C. -S. Chiu, F. L. Bahr, H. R. Kim, and Y. –J. Yang, 2004: Internal solitons in the northeastern South China Sea. Part I: Sources and deep water propagation. *IEEE J. Oceanic Eng.*, **29**, 1157-1181.

Schneck-Scott, A. R., 2004: Detection and resolvability of pulsed acoustic signals through the South China Sea basin: A modeling analysis. M. S. Thesis, Dept. of Oceanography, Naval Postgraduate School, Monterey, CA.

Schock, S. G., 2004: A method for estimating the physical and acoustic properties of the sea bed using chirp sonar data. *IEEE J. Oceanic Eng.*, **29**, 1200-1217.

INITIAL DISTRIBUTION LIST

1.   Defense Technical Information Center
       Ft. Belvoir, Virginia

2.   Dudley Knox Library
       Naval Postgraduate School
       Monterey, California

3.   Professor Mary Batteen, Chairman, Code OC
       Department of Oceanography
       Naval Postgraduate School
       Monterey, California

4.   Professor Ching-Sang Chiu
       Department of Oceanography
       Naval Postgraduate School
       Monterey, California

5.   Professor Patrick Harr
       Department of Meteorology
       Naval Postgraduate School
       Monterey, California

6.   Associate Professor John Colosi
       Department of Oceanography
       Naval Postgraduate School
       Monterey, California

7.   Visiting Professor Steven Ramp
       Department of Oceanography
       Naval Postgraduate School
       Monterey, California

8.   Visiting Assistant Professor D. Benjamin Reeder
       Department of Oceanography
       Naval Postgraduate School
       Monterey, California

9.   Research Associate Chris Miller
       Department of Oceanography
       Naval Postgraduate School
       Monterey, California

10.   LCDR Justin M. Reeves
        Department of Oceanography
        Naval Postgraduate School
        Monterey, California